A Correlated Study of $FeNiCoMn_xAl_x$

Magnetic, structural, and compositional properties of additive manufactured high-entropy alloy

Aleksander Amble Larsen

Thesis submitted for the degree of
Master in Materials Science for Energy and Nanotechnology
60 credits

Department of Physics
Faculty of Mathematics and Natural Sciences

UNIVERSITY OF OSLO

August 2021

A Correlated Study of $FeNiCoMn_xAl_x$

Magnetic, structural, and compositional properties of additive manufactured high-entropy alloy

Aleksander Amble Larsen

A Correlated Study of $FeNiCoMn_xAl_x$

http://www.duo.uio.no

Printed: Reprosentralen, University of Oslo

Acknowledgement

This master thesis is written as a part of the Magnificent Project.

First and foremost, I would like to thank each of my supervisors Anette E. Gunnæs, Pavlo Mikheenko, Spyros Diplas and Patricia Carvalho. Thanks to Anette for introducing me to the Magnificent project, and for the guidance along the way, and to the manager of the project, Spyros Diplas, for welcoming me to the Magnificent team. A big thanks to Pavlo Mikheenko for the help with the MFM experiments and for facilitation and assistance with the NAP paper. Also, a thank to Patricia Carvalho for the support with the FIB sample creation and Lorentz microscopy**.** A special thanks to Anthoula Poulia for the support in writing the NAP paper. Gratitude is shown to the whole Magnificent team - your willingness to share your knowledge has been highly valuable. Being part of such a competent and solution-oriented team has been crucial, especially under the pandemic which brought with it challenges that at times were demanding to overcome.

Furthermore, a thank is attributed to Ole Bjørn Karlsen for all advice, late night discussions and for showing interest in my thesis. Also, to Phoung D. Nguyen, for the TEM operation support.

I will also take this opportunity to thank my family for always having my back and supporting me along the way. Last but not least, to my girlfriend Karoline, for her positive mindset and motivation on an everyday basis.

Aleksander Amble Larsen

August 2021

Abstract

This study investigates magnetic, structural, and compositional properties of $FeNiCoMn_xAl_x$ High-Entropy Alloys (HEAs) processed by laser metal deposition. This alloy system has already been shown to possess promising soft magnetic properties and has been suggested for further in-depth study[1-3].

Two alloys of the $FeNiCoMn_xAl_x$ system with x = 0.29 and x= 0.9 have been studied. Both compositions have shown soft magnetic properties with intrinsic coercivity below 600 A/m. The $FeNiCoMn_{0.9}Al_{0.9}$ alloy was found to have the lowest coercivity and highest magnetization saturation of 280 A/m and 112 Am^2/kg, respectively.

The $FeNiCoMn_{0.29}Al_{0.29}$ alloy was found to consist of two phases, identified by Transmission Electron Microscopy (TEM) as a B2 and FCC phase. The B2 phase was found to be rich in Al and the FCC to be rich in Fe. The composition of these two phases were related to the magnetic domains by correlating results from Magnetic Force Microscope (MFM) with elemental analysis in Scanning Electron Microscope (SEM). The results uncovered better magnetic properties for the Al-rich B2 phase compared to the Fe-rich FCC phase, and this method is proposed as a possible technique for identifying magnetic phases in multiple-phase alloys.

The study further investigated the $FeNiCoMn_{0.9}Al_{0.9}$ alloy. This alloy was found to consist of a B2 phase having a similar composition as the Al-rich phase of the $FeNiCoMn_{0.29}Al_{0.29}$ alloy. Microstructural analysis in SEM revealed a dendritic structure with the dendrites showing a compositional variation from core to outer regions. This observation indicates a coring effect in the alloy due to solidification under non-equilibrium conditions. Energy Dispersive X-ray Spectroscopy (EDS) analysis showed a trend of correlation between the Al and Ni content, which both anti-correlated to Mn and Fe within the dendrite. A minor phase, rich in Mn and Fe, was observed systematically at grain boundaries and shown to be weakly magnetic.

The magnetic domain pattern acquired by MFM, was correlated to crystallographic orientations obtained by Electron Backscatter Diffraction (EBSD), for the same region. An easy axis along the [111] direction of the B2 phase was indicated by the presence of bubble-domains for this grain orientation. This provides an alternative technique to study magnetocrystalline anisotropy of a material.

Focussed Ion Beam (FIB) was utilised to extract a sample within a dendrite and study both structural and magnetic domains by Scanning TEM (STEM). Structural analysis showed no sign of an ordered $L2_1$ phase, which has been reported in a previous study for alloys of the same system with higher concentrations in Mn and Al[4].

Magnetic domains were studied by Lorenz Microscopy. In the demagnetized state, closure domain arrangement was observed. Domain wall motion was observed as a function of increased applied field from the main objective lens of the STEM. The result reveals pinning of the domain wall motion by the minor phase, rich in Mn and Fe, which is a possible source for increasing coercivity. Suggested future work to improve magnetic properties is adjusting the nominal composition combined with a post heat treatment to approach a single-phase and a more defect-free alloy.

Contents

Chapter 1

Introduction

Advanced soft magnetic materials are crucial for renewable electric energy generation towards reducing CO2 emissions, which topic has never been more relevant. Soft magnetic materials are key components in devices for electric power generation and conversion. Improving soft magnetic materials can thus give higher performance and increased energy efficiency, which in turn will contribute to a more sustainable energy use. Current soft magnetic materials are approaching the performance limit and the field requires new materials and novel methodologies. The current master project is connected to the “Magnificent” project funded by the Research Council of Norway, where the aim is to develop soft magnets based on high entropy alloys, using a digitalised approach with additive manufacturing and subsequent post treatment.

1.1 High entropy alloys

High Entropy Alloys (HEAs) have been of increasing interest among material scientists since the discovery of five principal elements was observed in a single-phase solid solution in 2004[5]. In conventional metallurgy, alloys are mixtures consisting of mainly one dominant element in addition to small quantities of others. Therefore, the idea of mixing high concentrations of many principal elements is quite radical. Owing to the high configurational entropy, these alloys can stabilise as single crystal structures rather than intermetallic phases. The concept of HEAs promotes the establishment of promising materials in the field, with possibilities of an optimised mixture of properties not found in conventional alloys. This can lead to discovery of new materials of superior functionality in technological applications[6]. One of these applications concerns development of materials with better soft magnetic properties that can increase energy efficiency in electricity generation by e.g., reduction of hysteresis loss.

1.2 Soft magnetism and energy loss

A good soft magnetic material exhibits the property of easily being magnetized and demagnetized by an external field. Soft magnets are often utilized to channel or enhance a magnetic flux produced by an electric current. If the applied field is alternating, the magnetic material will continuously swich directions of magnetisation. However, there is a hysteresis associated to the magnetisation of the material and the applied field. That is, the magnetisation in the material lags behind changes in the external field. This hysteresis is not desired, as there is an energy loss associated to it. By developing softer magnetic materials, hysteresis loss in electrical devices can be reduced.

An important magnetic property for a soft magnetic material is the magnetic permeability, which is desired to be as high as possible. The magnetic permeability is the degree of magnetization in a material in response to an applied field. A brief introduction to the relationship between the applied magnetic field and the magnetisation of the material will be described next with a hysteresis loop.

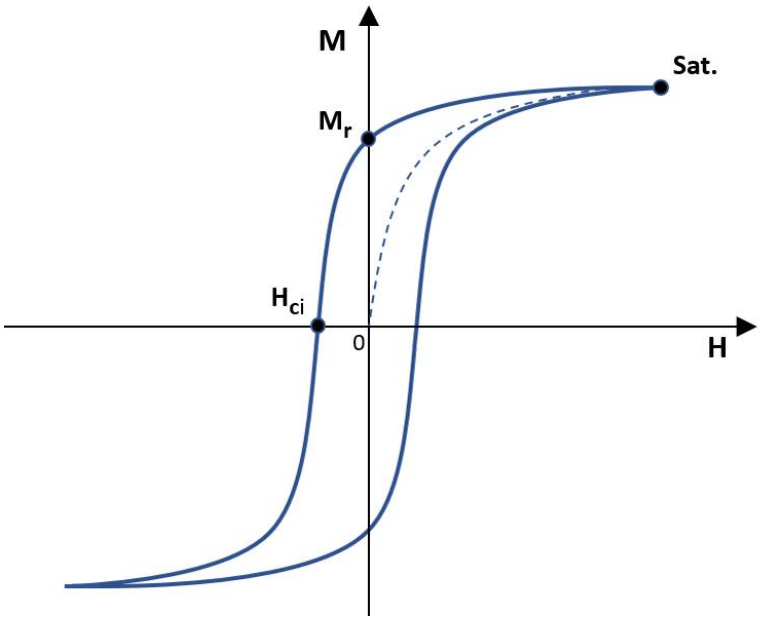

Fig. 1.1: Hysteresis loop of a ferromagnetic material. Magnetization, M, is plotted as a function of applied magnetic field, H. The saturation magnetization (Sat.), remnant magnetization (M_r) and the intrinsic negative coercivity point (H_{ci}) are shown.

When applying a magnetic field H, to an initially unmagnetized ferromagnetic sample (M=0), it becomes magnetized. Increasing the external field will cause domains to grow and align, resulting in an increasing magnetization, M, of the material. Saturation magnetization (Sat.) is achieved when no more domains align with the increasing field. This step is illustrated by the dotted line from 0 to Sat. in Fig 1.1. If now reducing the external field from the level which reached Sat., the domains in the material will not immediately return

to their initial direction of magnetization. This is due to resistance of domain movement in the material. Thus, magnetization will not follow the same path in reverse when plotting the magnetization versus the applied field.

When considering a hysteresis loop, there are mainly three factors of interest. These factors are saturation magnetization, remanent magnetization, M_r, and the intrinsic coercivity, H_{ci}. For e.g., core magnets in industrial applications, the saturation is a limitation for the maximum achievable magnetization. To increase it, the mass of the material must be increased, or new materials with higher saturation magnetization must be developed. The remanent magnetization, M_r, is the magnetization value for the material, in absence of an external field and high values are associated to permanent magnets. The intrinsic coercivity, H_{ci}, equals the external field required to de-magnetize the material which is desired to be as low as possible for soft magnetic materials.

The energy required to complete a full cycle of magnetization and demagnetize of a material is represented by the area of the hysteresis loop. By reducing the intrinsic coercivity for a magnet, the area of the hysteresis loop decreases as Fig 1.1 demonstrates. Thus, less energy is required to complete a full cycle of magnetization for a given saturation value. This energy difference is referred to as hysteresis loss. Minimizing hysteresis loss is the main motivation for producing softer magnetic materials.

1.3 Master thesis' aim and objectives

The overarching goal for this research is to contribute to developing a soft magnetic material of the $FeNiCoMn_xAl_x$ high-entropy alloy system. The more specific aim for this thesis is to study the magnetic, structural, and compositional properties and investigate the relationship between these variables. The study will focus on a selected set of samples for different concentrations of Mn and Al and proceed with in-dept analysation of the phases with the most desirable properties for applications as a soft magnetic material. The study aims to point out trends related to the magnetic, structural, and compositional variables and potential improvements for future development.

The samples will be prepared by laser metal deposition by the Magnificent project group. Structural characterization will be studied by utilizing X-Ray Diffraction (XRD) and Transmission Electron Microscope (TEM). Magnetic characterization will be performed through Vibrating-Sample Magnetometry (VSM), Magnetic Force Microscope (MFM) and Lorentz Microscopy in TEM. Energy Dispersive x-rays Spectroscopy (EDS) in Scanning Electron Microscope (SEM) will be used for elemental analysis. The methodology that will be used to achieve the objectives, is to conduct correlated studies by combining some of the mentioned techniques.

Due to the covid-19 situation which lead to periods with restricted access to the University of Oslo and laboratories, the author was not able to complete the started TEM training. At the time of the opening,

decisions were made by the supervisors not to restart this training to become an independent TEM operator. To attain the goals of the thesis, TEM operation was thus assisted. The author was present at all TEM experiments, guiding the operator towards the objective of the individual experiments.

Chapter 2

Theory

This chapter is dedicated to establishing a theoretical background for the results presented in this thesis. A brief description of key concepts for instruments and theory are given.

2.1 Structural and compositional characterization

2.1.1 Energy dispersive x-ray spectroscopy

Energy Dispersive X-ray Spectroscopy (EDS) is a method for analysing the chemical composition of a material. The method is usually integrated in both SEM and TEM. An electron beam in the instrument is projected on to a specimen and the emitted X-rays are detected. The incident beam kicks out electrons from inner atomic shells, increasing their energy and allowing them to drop to the available lower levels. Photons of characteristic energy are emitted, which are identified by the detector. The number of counts for each energy is plotted, and the intensity in the spectrum determines the elemental composition.

The interaction volume in a bulk sample in SEM is a drop-shaped volume, typically 1-5 micrometre below the surface. Therefore, the results should be considered relative to the surface area measured with a correction, knowing that the data may come from a larger volume under the surface. In TEM EDS, the beam is transmitted through the sample and a higher accuracy can be achieved locally.

2.1.2 Braggs' law

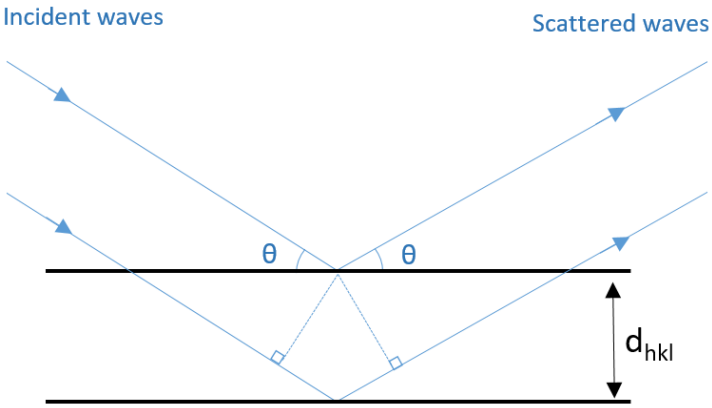

Fig. 2.2 is a schematic illustration of Bragg's law.

Consider a beam of monochromatic X-rays that are in phase, scattered from crystal planes with an angle equal to the incident angle. Waves that interact with distinct *hkl* planes, will travel a different distance before and after they are scattered. This will cause a relative phase shift and produce constrictive and destructive interference. This occurs when the path of the waves differs by a whole and a half wavelength, respectively. The relationship is given by Bragg's law in Eq. 2.1 and a schematic illustration is shown in Fig 2.2.

$$n\lambda = 2d_{hkl}sin\theta \qquad (2.1)$$

n is an integer, λ is the wavelength, d_{hkl} is the distance between *hkl* planes, θ is the angle between the incident wave and the *hkl* plane.

2.1.3 Electron backscatter diffraction

Electron backscatter diffraction (EBSD) is a technique to analyse microstructure, crystallographic orientations, and grain boundaries in a material with an SEM. The experimental set up is arranged with a high angle tilt between the electron beam and sample, as more electrons are diffracted at a height angle, typically around 70 degrees. This is done to attain a good contrast of the inelastically scattered electrons, which form a Kikuchi pattern on a phosphor plate. The incident beam and crystal interaction result in cones of diffracted electrons, which when overlapped form a Kikuchi pattern. Two intersecting Kikuchi lines represent a zone axis. A Hough transformation is acquired by the instrument software, which matches the Kikuchi pattern of the sample to a list of crystal structures appended by the user. Finally, an image of grain orientations and phases can be obtained.

2.1.4 Electron channelling in SEM

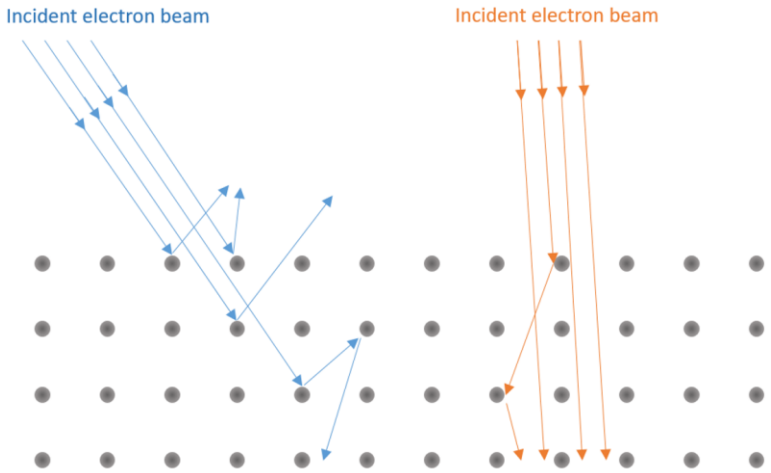

Fig. 2.1: A schematic illustration of two incident electron beams with a different orientation, relative to a crystal lattice

Electron channelling is the result of the interaction of electron beam with the material, which is dependent upon its crystallographic orientation. If the incident electron beam projection is closely aligned to a zone axis, the proportion of backscattered electrons (BSEs) may be less compared to a low-symmetry crystal orientation, and this gives rise to a contrast in e.g. the BSE image in SEM which is illustrated in Fig 2.1.

2.1.5 Structure factor

The structure factor represents the amplitude and phase shift of a diffracted beam from a crystal and is a summation of all scattered wave contributions for the atoms in the unit cell. The observed intensity in a diffraction experiment is proportional to $|F_{hkl}|^2$. Thus, if the structure factor is zero, the intensity will be zero. The expression for the structure factor is given by Eq. 2.2

$$F_{hkl} = \sum_{j=1}^{N} f_j \cdot e^{-2\pi i(hx_j + ky_j + lz_j)} \qquad (2.2)$$

Here, x, y and z are the coordinates for the atom j. The *h*,*k*, and *l* are the Miller indices and f is the scattering factor for atom j, N is a positive integer, e is Euler's number, and i is the imaginary unit.

2.1.6 Transmission electron microscope and selected area diffraction

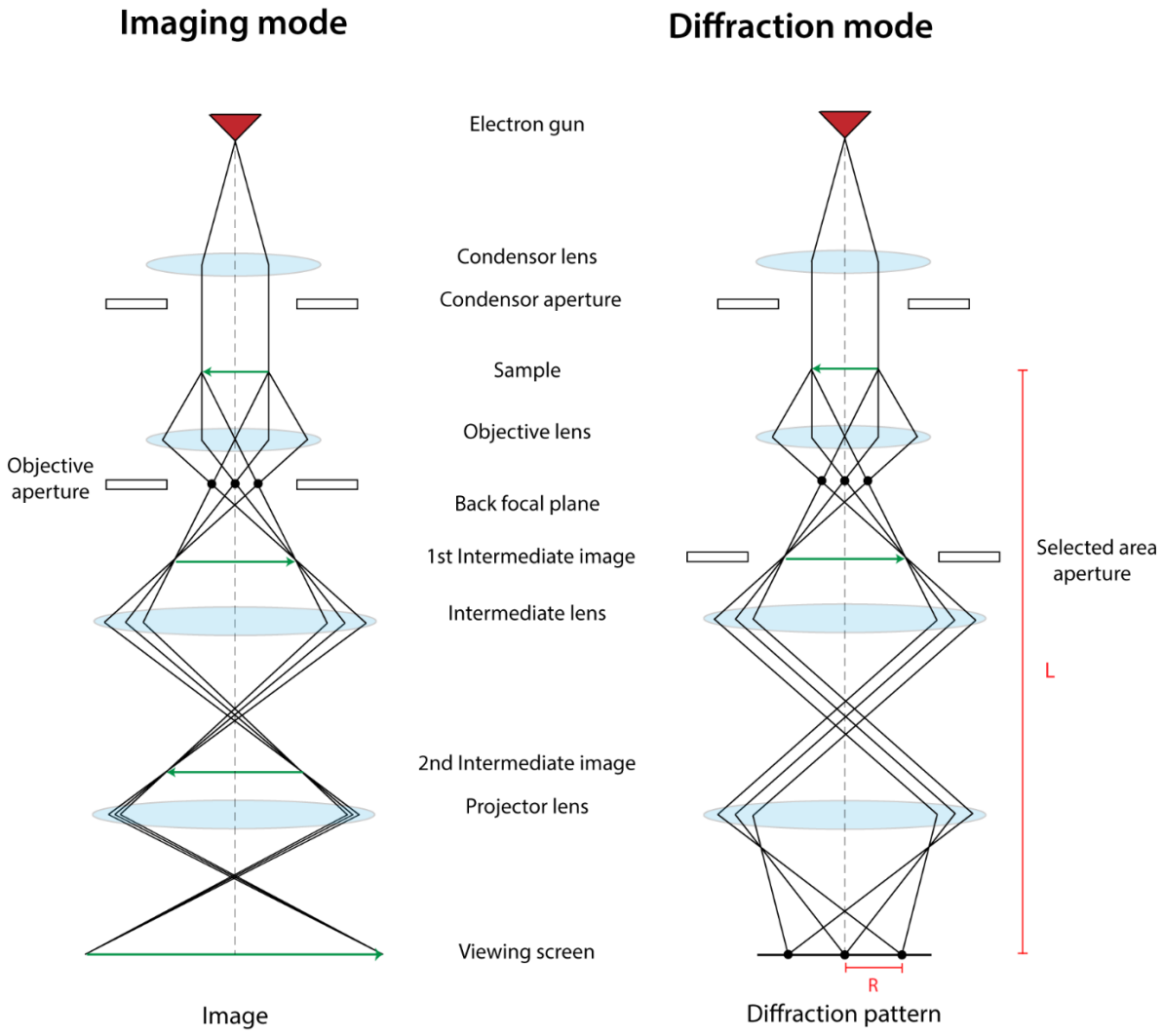

Fig. 2.3: A ray diagram for imaging and diffraction modes in a TEM. The two modes differ by the strength of the intermediate lens.

A TEM utilizes an electron beam to illuminate a sample. The electron beam is accelerated by a potential of typically 60-300 kV. The incident beam is guided by magnetic lenses and aperture to interact and transmit through a thin specimen. The TEM can be operated to study both real and reciprocal space. A ray diagram of a TEM is schematically represented in Fig 2.3 and shows the two modes of imaging and diffraction. The two modes differ by the strength of the intermediate lens.

Selected area electron diffraction (SAD) is a common method to study the diffraction pattern from a specific region. An aperture is inserted in the first image plane to confine the area of interest and the intermediate

lens is focused to project the diffraction pattern, as shown in the diffraction mode in Fig 2.3. Diffracted waves that are parallel to each other will intersect in the back focal plane and form a diffraction pattern. Each diffraction spot, or reflex, represents a set of planes in the crystal structure. To index these spots, the reciprocal distance can be evaluated by Eq. 2.3 and the fact that reflexes occurring on the same line are dependent and related to each other through parameter n·[h+k+l], where n is an integer.

$$Rd = \lambda L \tag{2.3}$$

The equation shows the relationship between the interplanar spacing, d, in the crystal, and the distance between the central- and the diffracted beam, R, in the diffraction pattern. λ is the wavelength of the electron beam and L is the camera length, which is the distance from the sample to diffraction pattern in the viewing screen. λ·L is usually referred to as the camera constant. The pattern indexing must satisfy vector addition condition, and it is therefore sufficient to determine only two reflexes.

A zone axis is a major direction in a crystal, at which the diffraction pattern is symmetric. The zone axis is antiparallel to the incident beam and normal to the diffraction spots. Thus, the zone axis can be obtained by the cross product of two indexed spots.

For a cubic crystal lattice:

$$d = \frac{a}{\sqrt{h^2 + k^2 + l^2}}. \tag{2.4}$$

Here, d is the interplanar distance, a is the lattice constant, and h, k, l are the Miller indices.

Considering two independent reflexes, R_1 and R_2, the ratio can be determined from Eq. 2.5, which is a combination of Eq. 2.3 and Eq. 2.4 above.

$$\frac{R_2}{R_1} = \frac{d_1}{d_2} = \frac{\sqrt{{h_1}^2 + {k_1}^2 + {l_1}^2}}{\sqrt{{h_2}^2 + {k_2}^2 + {l_2}^2}} \tag{2.5}$$

Eq. 2.5 reflects the d ratios and the geometry of the unit cell

2.1.7 Scanning transmission electron microscope

Scanning Transmission Electron Microscope (STEM) is a technique where a converged beam focused to a spot size of typically 1-2 Å, is used to scan across a sample. The STEM mode is set up with annular detectors, collecting scattered electrons from the sample interaction. The image for each detector will have a different contrast depending on the collection angles of electrons. All images can be acquired simultaneously from the same region due to the annular geometry.

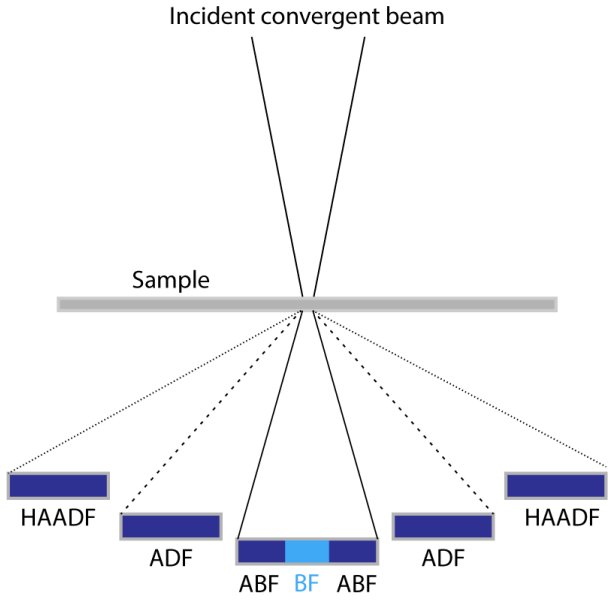

Fig. 2.4: A cross section illustration of the annular detectors in STEM mode.

Bright Field (BF), Annular Bright Field (ABF), Annular Dark Field (ADF) and High Angle Annular Dark Field (HAADF) are the available detectors from low to high angles, respectively. The detectors are illustrated in Fig 2.4. The BF detector measures the intensity of the direct transmitted beam and small scattering angles, 0 to 10 milliradians (mrads) and detects mainly Bragg diffracted electrons. For these images, it can be difficult to separate whether atomic columns are dark or bright since it depends strongly on the defocus and additional simulations may be required to associate the contrast to the atomic columns. In contrast, the ABF measures electrons scattered typically from 10 to 20 mrads and both light and relatively heavy elements, like transition metals. The images will appear with high contrast and can be interpreted more intuitively[7]. The ADF detector gathers all scattered electrons from 20 to 40 mrads. The HAADF image shows mainly Z-contrast and is obtained registering electrons scattered above 70 mrads, which are mostly Rutherford scattered electrons. The mrads range for the annular detectors depends on the camera length.

2.2 Magnetic characterization

2.2.1 Vibrating Sample Magnetometer

A vibrating sample magnetometer (VSM) is an instrument measuring the hysteresis loop for a magnetic material. The instrument applies a constant magnetic field in one direction, on to a sample. The sample is mounted to a vibrating tip. There are coils around the tip, to detect changes in the magnetic field lines. When the tip is oscillated up and down, normal to the applied field, this will cause changes in the magnetic field and a current is induced in the coils, according to Faraday's law. The instrument will measure the magnetization in the material by the induced current. A hysteresis curve can be recorded when the applied field is increased until the material is saturated and equally for the opposite direction.

2.2.2 Magnetic force microscopy

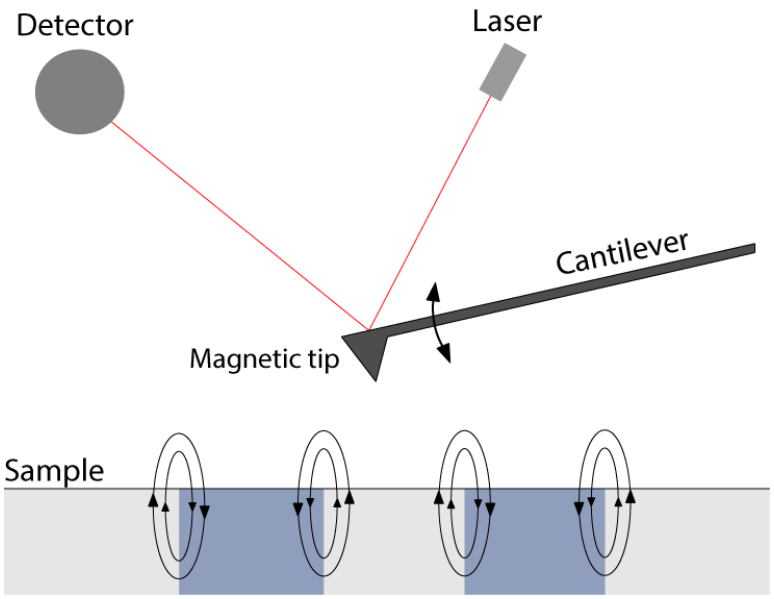

Fig. 2.5: A schematic illustration of an MFM. The magnetic domains are illustrated by different colours and magnetic field lines.

Magnetic force microscopy (MFM) is a method for studying magnetic properties above the surface of a flat specimen. A cantilever is oscillating with a resonance frequency above the surface of a material, with a magnetic tip attached. The deflection of the tip is measured by a laser, reflected from the cantilever to a photodiode detector. When the tip interacts with a magnetic specimen, the phase of the oscillation is shifted. The phase shift is proportional to the gradient of force, with which aligned magnetic domains of the sample

act on the magnetic tip[8, 9]. The magnetic force in z-direction, i.e. perpendicular to the surface, can be obtained by knowing the magnetization/dipole moment of the tip[10].

The technique is surface sensitive, and the topography of the sample will affect the phase shift, if the tip is scanned across the flat sample at a constant height. However, there is a dual scan mode, which can compensate for this effect. First, the topography of the sample is scanned at a constant high above the surface and, subsequently, a scan following the path of the topography is performed, and the magnetic force is measured. This mode produces a force map without topographic effects.

2.2.3 Magnetocrystalline anisotropy

Magnetocrystalline anisotropy is the property of a crystal having a preferred direction of the magnetic moment with respect to the lattice. This originates from spin-orbit coupling and the confined positions of the atoms in the lattice[11, 12]. This leads to that some directions in a crystal requires more energy to be magnetized than others. If a weak field is applied to a demagnetized crystal, the direction in which spontaneous magnetization of domains will occur is called the easy axis. However, if the applied field is sufficiently strong, the domains will align parallel to the field and not to the easy axis[12]. The coercive field in a material is strongly connected to the magnetic anisotropy and more isotropic magnetic properties are desired for soft magnets[13].

2.2.4 Lorentz microscopy – Fresnel mode

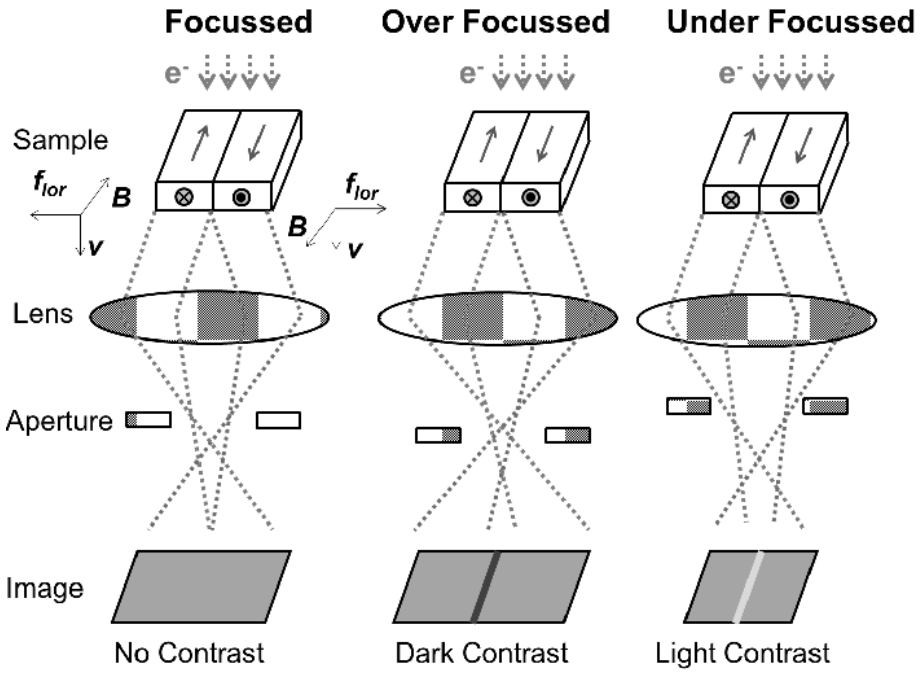

Fig. 2.6: The ray diagram in Fresnel mode for different defocus[14].

Lorentz Microscopy (LM) is a method to study magnetic domains using a TEM. In the so-called Fresnel mode, the TEM is set up with the objective lens turned off to not apply an external field and interact with the magnetic specimen. When a parallel electron beam passes through a ferromagnetic material in the TEM, it can be deflected due to the Lorenz force interaction between the beam and the magnetic domains. The beam deflection will depend on the direction of the magnetic moment for the domain, relative to the electron beam direction. For two adjacent domains with reverse magnetization direction, the electron beam is deflected in opposite ways according to the right-hand rule. As illustrated in Fig. 2.6, the domain walls will appear with bright and dark colour, depending on the defocus. To distinguish the domain walls, contrast from to other features, one can compare the over- and under-focus images, as domain walls are expected to appear with opposite contrast. If the beam is in focus with respect to the image plane, no contrasts contributed by domain walls are present in the image.

Chapter 3

Literature

3.1 HEAs and the $FeNiCoMn_xAl_x$ system

3.1.1 Definition of HEAs and the concept of phase stabilization

There are some varieties in the literature on how to define an HEA. The initial definition is an alloy with minimum five principal elements, each with a concentration between 5-35 at. %[15]. Another definition of HEA is an alloy mixing enthalpy above 1.5 R in solid solution, where R is the universal gas constant [16, 17].

The principle of phase stabilization driven by mixing enthalpy (or entropy), can be understood from Gibbs free energy in Eq (3.1).

$$\Delta G_{mix} = \Delta H - T\Delta S_{mix} \qquad (3.1)$$

G_{mix} is the Gibbs free energy, H is enthalpy, T is absolute temperature and S_{mix} is the mixing entropy.

A very negative value for ΔH would promote ordered intermetallic phase formation. According to the empirical Hume-Rothery rules for substitutional solid solution formation, elements with similar atomic radii and electronegativity can easily substitute atomic positions in a solid solution. Thus, having a similar probability of occupying a given position in the crystal lattice[18]. Mixing elements that satisfy the Hume-Rothery criteria in adequately high amounts to achieve a sufficiently high entropy, can allow formation of a chemically disordered crystal structure, preferred to e.g., forming intermetallic phases. Entropy can in this case dominate the enthalpy and be the main contribution to stabilising solid solution phase formation.

3.1.2 The A2, B2, and $L2_1$ structures

Since some crystal structures are thoroughly discussed in this thesis and in the literature of HEAs, a short introduction of these is given below.

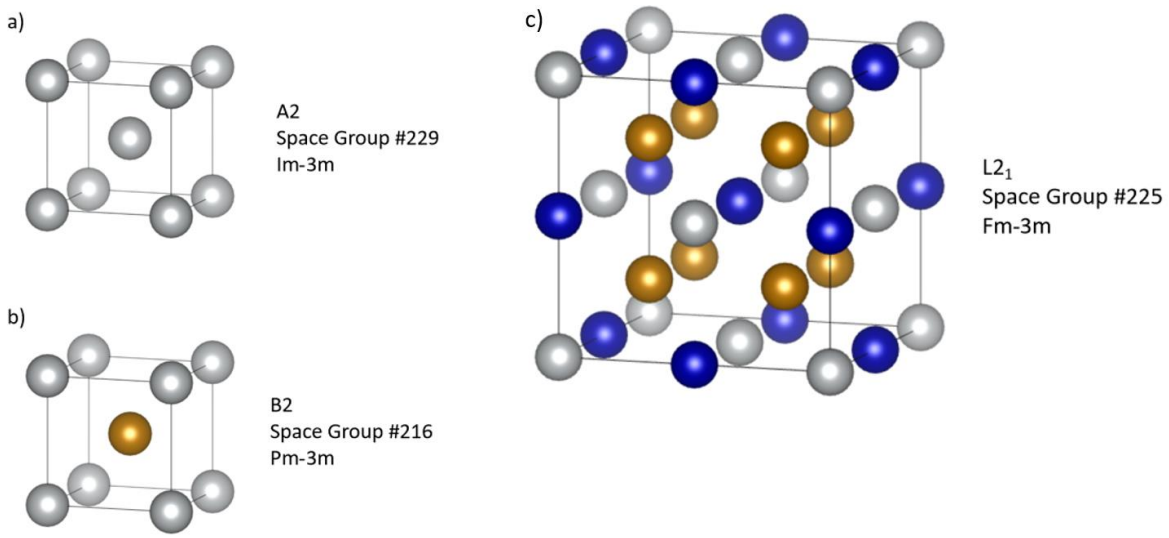

Fig. 3.1: Models of **a)** A2 structure, **b)** B2 structure, and **c)** $L2_1$ structure.

The first structure to be mentioned is the A2 structure, which is well known and commonly referred to as a simple BCC, illustrated in Fig 3.1 a. Second is the B2 structure that has two atomic sites as shown in Fig 3.1 b. The B2 is commonly referred to as an "ordered BCC" in the literature. However, strictly speaking, this structure is primitive as the space group symbol indicates, not body-centred. The largest structure is the $L2_1$ and is also known as a full-Heusler. The structure is a face-centred one, as illustrated by the silver spheres' position in the unit cell in Fig 3.1 c. The $L2_1$ can be described as a simple FCC with fully occupied tetrahedral and octahedral holes. The structures are related to each other by degrees of ordering. Starting from the $L2_1$, the symmetry reduces to that of a B2 type upon disordering the atomic sites for the blue and silver sphere. Further, by disordering all atoms in the B2 unit cell, one arrives at the symmetry of the A2. Hence, the configurational entropy is greatest for the A2 and lowest for the $L2_1$.

3.1.3 Predictions of phase stabilities in HEAs

A simplified estimate to predict the phase stability of a BCC, FCC, or mixture of phases, can be achieved by calculating the average Valence Electron Concentration (VEC) for the composition. The method is commonly used in the literature and is based on empirical results[17, 19]. An example is given in Fig 3.2 below. The figure is illustrating the effect of VEC to phase stability and is found in the paper by Guo et

al.[19]. Half-filled symbols in this figure are representing a mixture of FCC and BCC phases, whereas non-filled and fully filled symbols represent sole BCC and FCC phases, respectively. According to Guo et al, the dotted line shows the intervals for VEC where HEAs are expected to be pure BCC, FCC+BCC or pure FCC. It is important to notice that the term BCC is in their paper used to include the *primitive* B2 phase[17]. Hence, this could be a possible source for misconceptions in the field.

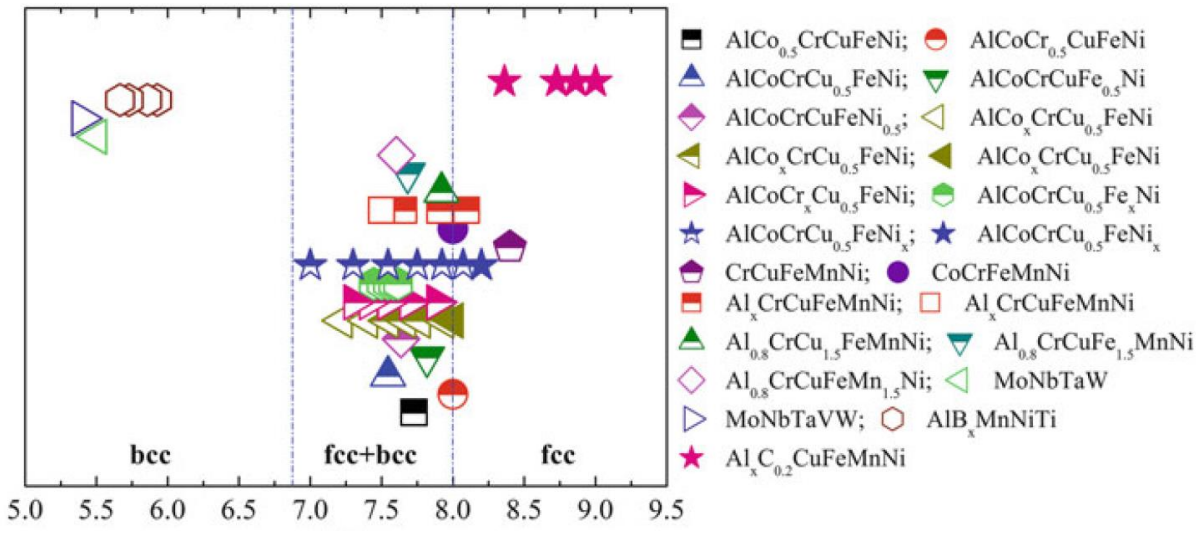

Fig. 3.2: A relationship between the VEC and phase stabilisation of BCC, FCC + BCC and BCC published by Guo et al. [19]

With regards to VEC and phase stability, Yang et Al[20] points out that the method has limitations. For example, the method is not accounting for temperature and gives inconsistent threshold values for some alloy systems. However, this method could be useful in early stages to predict alloys with desired structures, by e.g., using the knowledge that FCC tends to be more ductile and BCC tends to be stronger[21] for composition design.

For prediction of possible phase stabilities on a more fundamental basis, ab initio calculations are commonly used in the field. For the given system of $FeNiCoMn_xAl_x$ that is presented in this thesis, such calculations have been performed within the framework of the Magnificent project. The calculations were performed with regards to a variation of x, i.e., the concentration of Mn and Al. They predicted that an FCC phase was energetically favoured at low concentrations of x = 0.2 and an ordered $L2_1$ as the most stable phase at x = 1.5[4]. The phase that was second lowest in energy was a B2 phase for x = 1.5. A sample with the highest concentration of Mn and Al was experimentally observed to have a nanoscale structure with both B2 and $L2_1$ in an interplay mixture. The study utilized TEM investigations. However, in this thesis it is not clear whether alloy B, with a lower Mn and Al concentration, possesses the same nanostructure.

3.1.4 Mixing aluminium in HEAs

Oqura et al. [22] reports that the phase stability of FCC and BCC for an $FeNiCoAl_xCr$ alloy, presumably depends on the aluminium content. Further, they found that for some values of x, more ordered structures, such as B2 and $L2_1$, are energetically favoured over simple BCC (A2). This is in accordance with the ab initio calculations done by the Magnificent group. Stepanov et al. report the same observation for different HEA systems, when increasing Al content in combination with transition metals[23]. Wang et al. [24] suggest that the effect of aluminium's large atomic size, as compared to that of the transition metals, could have an impact on the phase transition from FCC to BCC due to lower atomic packing-efficiency. Contrary to aluminium, Lee et al. [25] proposes that iron is a stabiliser for the FCC phase in a HEA with both elements. A general trend in the literature is that an increased Al content seems to stabilise more ordered structures, i.e. structures of a lower configurational entropy.

In relation to magnetic properties, Huang et al. [26] indicate that addition of Al, which in its pure form is non-magnetic, can cause a transition from a paramagnetic state to a ferromagnetic state for a material in room temperature. This sets Al as an interesting candidate for future development in magnetic compounds.

3.1.5 Magnetic properties of the $FeNiCoMn_xAl_x$ system and characterization techniques

The magnetic properties of the $FeNiCoMn_xAl_x$ system have been studied by Panpan Li et al[1, 3]. Multiple papers that have been published are advocating this alloy to be a potential soft magnet for future use, and they expect further in-depth-studies for this composition. They found that x = 0.25 is the composition with the best soft magnetic properties after annealing. The composition was reported to be an FCC phase with a minor fraction of B2 phase. Zhong Li et al. [2] have studied the same system and are suggesting a transition from FCC to a BCC depending upon low and high concentration of Mn and Al, and also promoting the $FeNiCoMn_{0.25}Al_{0.25}$ alloy. However, in contradiction to Panpan Li et al, Zhong Li et al. are not mentioning any presence of B2 phase or of an ordered BCC phase. Both of the above papers utilized XRD and VSM for structural and magnetic characterization.

VSM is a common method in the field to obtain the magnetic saturation and coercivity values of a material. The method gives the average values of all crystal grains along the measured direction. As magnetic properties, especially coercivity, depend on the magnetocrystalline anisotropy[13], relating the crystal structure to the magnetic properties is critical to further develop and improve soft magnetic materials. However, the VSM technique has limitations in determining anisotropy for single crystals. The same applies for torque magnetometry, which is dedicated to analysing magnetic anisotropy for bulk materials. The author has not found any published work related to the magneto crystalline anisotropy of the $FeNiCoMn_xAl_x$ system, neither any comparison of magnetic properties of the distinct phases in the mixed alloys. These two aspects are targets for further investigation in this thesis.

An important characteristic related to anisotropy is the easy axis of the material. The easy axis of a magnetic material is utilized in power transformers to reduce energy loss and increase permeability[27]. This can be achieved by aligning the core magnet with its easy axis parallel to the direction of magnetization. Such core magnets are known as grain-oriented in the industry. BCC Fe has its easy axis along the [100] direction, while FCC Ni has its easy axis along the [111] direction [28, 29]. To investigate magnetic properties more locally, Lorenz Microscopy and MFM are examples of commonly used techniques for a material scientist. These methods allow for studying domain patterns in local regions.

In relation to improving magnetic properties, annealing the material is a frequently used method. Zhang et Al [30] points out that this heat treatment is key to obtain superior soft magnetic alloys in their study of $FeNiCoCu_xAl_x$. Mishra et al [31] found that annealing also is beneficial in terms of increased magnetic saturation.

To summarise, the $FeNiCoMn_xAl_x$ system is promising with regards to soft magnetic properties, and the result from the Magnificent project reveals complex nanostructure for the high content of Mn and Al. What is not clear is what the magnetocrystalline anisotropy and domain structure of this alloys are like. In addition, it is not clear whether the composition presented in this thesis, with slightly lower concentration of Mn and Al, obtains the same nanostructure with an interplay mixture of the $L2_1$ and B2 phase.

Chapter 4

Methods

In this section, the sample preparation, experimental, and post data-processing methods are presented. First follows an overview of the compositions and a short summary of the correlating techniques, which were performed for the two alloys.

4.1 Samples

The high-entropy alloys were processed by laser metal deposition at SINTEF by the Magnificent group, with the nominal compositions given in Table 4.1. The alloys will be referred to as Alloy A and Alloy B.

Table 4.1: Nominal compositions

Alloy	**Chemical formula**
A	$FeNiCoMn_{0.29}\ Al_{0.29}$
B	$FeNiCoMn_{0.9}Al_{0.9}$

4.1.1 Correlated studies of Alloy A

The objective of the experiments conducted on this alloy, was to investigate the correlation between the magnetic, structural, and compositional properties of this dual-phase alloy. Further, to determine the phase with the best magnetic properties of the two. The sample was marked with an indentation tool to observe the same area in both MFM and SEM. A FIB sample was extracted from the region studied, but unfortunately lost in the process of mounting it for TEM investigation. Therefore, the structures of the two

phases were analysed by making a TEM sample from the bulk material by polishing. The structures were related with EDS to the corresponding chemical phases observed in SEM.

4.1.2 Correlated studies of Alloy B

This alloy is similar to the phase with the best magnetic properties observed in the dual-phase alloy, in a purer state. Thus, this alloy was more thoroughly investigated. Powder XRD and modelling of the structure were carried out in the beginning, validated by Rietveld refinement. MFM, EDS and EBSD were cross correlated with measurements acquired for the same region to correlate magnetic properties to crystal orientation and composition. Subsequently, an FIB sample was extracted from the same region of interest to further study the crystal structure and composition in the STEM. The magnetic properties of the domain walls were investigated by Lorentz microscopy conducted on this FIB sample.

4.2 Sample preparation methods

4.2.1 Sample preparation for hysteresis loop measurement

The samples were cut with a diamond metal blade from the middle of the bulk material. Further, the slices were cut to a 3x3x3 mm cube and subsequently grinded with a 400 grit size silicon carbide paper, down to an approximately one-millimetre edged cube. The samples were weighted with a high precision electronic scale and embedded in epoxy. Furthermore, the epoxy was cut manually with a hacksaw to a 3x3x3 mm epoxy cube with the sample in centre. The reason for the epoxy was not to damage, contaminate or oxidize the sample. Additionally, it could more easily be found if it fell off the vibrating tip.

4.2.2 Sample preparation for MFM and SEM with characteristic indentation marking

The material was cut from the inner region of the bulk sample, grinded and polished to a 1x3x3 mm slice. The grinding and polishing were done with Allied MultiPrep, and angular calibration was performed in order to attain a flat sample with parallel surfaces for the MFM measurements. Grinding was done with accordingly 800, 1200, 2000, and 4000 grit size silicon carbide paper, followed by polishing with cloths. The clothes were sprayed with diamond powder of 6, 3 and 1 micrometres, respectively.

The sample was marked with a Vickers hardness tool, Zwick 3212, in an asymmetric pattern. The intention of this was to localize a specific position and orientation during measurements on the MFM and later study the same region with the SEM and correlate the results. Low magnification overview images of the sample, captured with light microscope, were printed out and brought to the instruments to identify and track the measured areas as is shown in Fig. 4.2 a.

4.2.3 Etching

Etching of the samples was done with a solution of nitric acid and ethanol, with parts of 1:9 respectively, more commonly known as Nital. The acidic solution was applied to the material with a cotton swab for 15 seconds and subsequently the sample was washed with water and isopropanol. The goal was to study microstructure of the sample in optical microscope, but then EBSD was also carried out on an etched sample to compare it with an un-etched sample. The reason for this was some inconsistent results with regards to the microstructure observed for the etched sample in light microscope and the un-etched sample in EBSD.

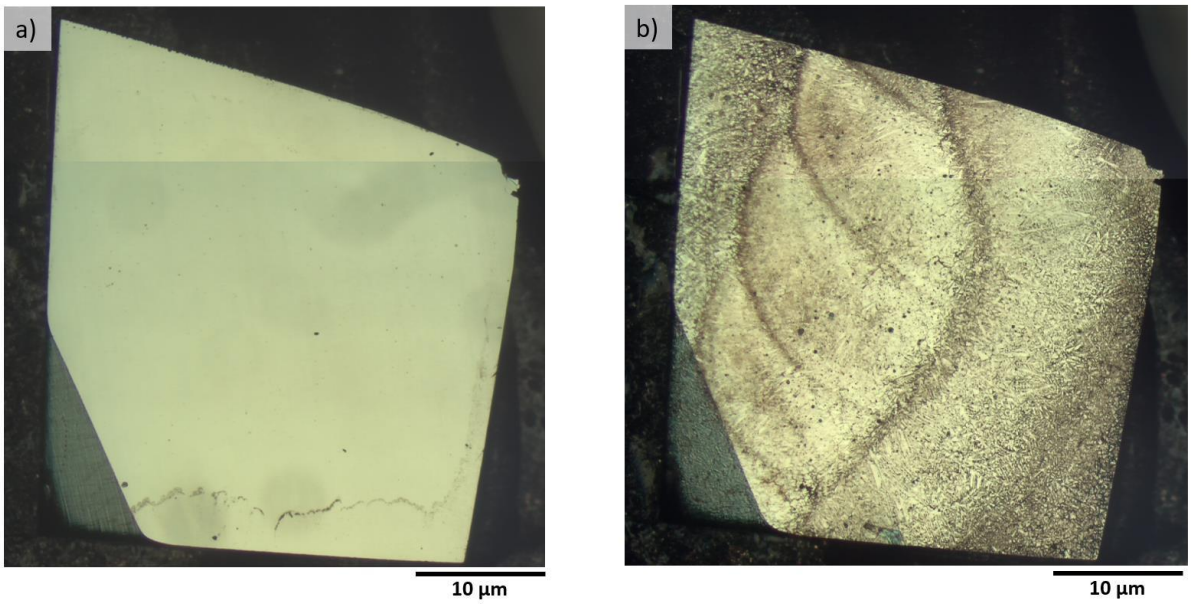

Fig. 4.1: Images of a sample **a)** before etching and **b)** after etching the surface with Nital. The images are captured with light microscope on low magnification.

4.2.4 TEM wedge sample preparation made from bulk

The objective for this preparation was to make a wedge specimen and glue it to a copper ring holder for the TEM. A slice of 2x2x1 mm was cut from bulk sample and glued to a holder for the MultiPrep tool, which first was calibrated for flat polishing. Diamond abrasive films of 30, 15, 6, 3 and 1 micrometre roughness were used to polish the sample down to a thickness of respectively 1000, 700, 650, 600 and 590 micrometres. The thickness was measured with a digital dial indicator from Mitutoyo. The load on the MultiPrep was reduced from full (6) to minimum (1), as finer polishing films were applied. The wedge was made by gluing the material to a new sample holder with a glass underneath, allowing angular polishing, and a tilt of 2 degrees was set. From this point on, the wedge thickness was measured by determining the length of the wedge tip by a Reichert-Jung MeF3 light microscope, mounted to a camera. An image was captured at 120× magnification, and the scale bar was calibrated by observing a grid with known spacing. Papers with

particles of 15, 6, 3, 1 and 0.5 micrometres were used to shape the wedge geometry in steps of 250, 150, 50, 20 and below 20 micrometre thickness of the wedge tip, respectively. Mechanical polishing was stopped at the point when glass was removed from the sample holder. Further, ion milling with a Precision Ion Polishing System (PIPS) was conducted. Accelerating voltage of 5 kV was used for 30 min at an angle of 7 degrees followed by 3 kV in 20 min with an angle of 5 degrees.

4.2.5 TEM sample preparation by FIB

A Focused Ion Beam (FIB) instrument of type FEI Helios NanoLab DualBeam was used to extract a TEM sample from a specific region, after performing experiments in the SEM and MFM. The instrument was operated by Patricia A. Carvalho and done at NTNU NanoLab in Trondheim. She received an instruction from the author of how to locate the region that was already measured. This included an overview image from optical microscope with indentation marks as shown in Fig. 4.2 a, and SEM images of the specific grain and region to extract TEM sample close to the indentation mark, shown in Fig. 4.2 b.

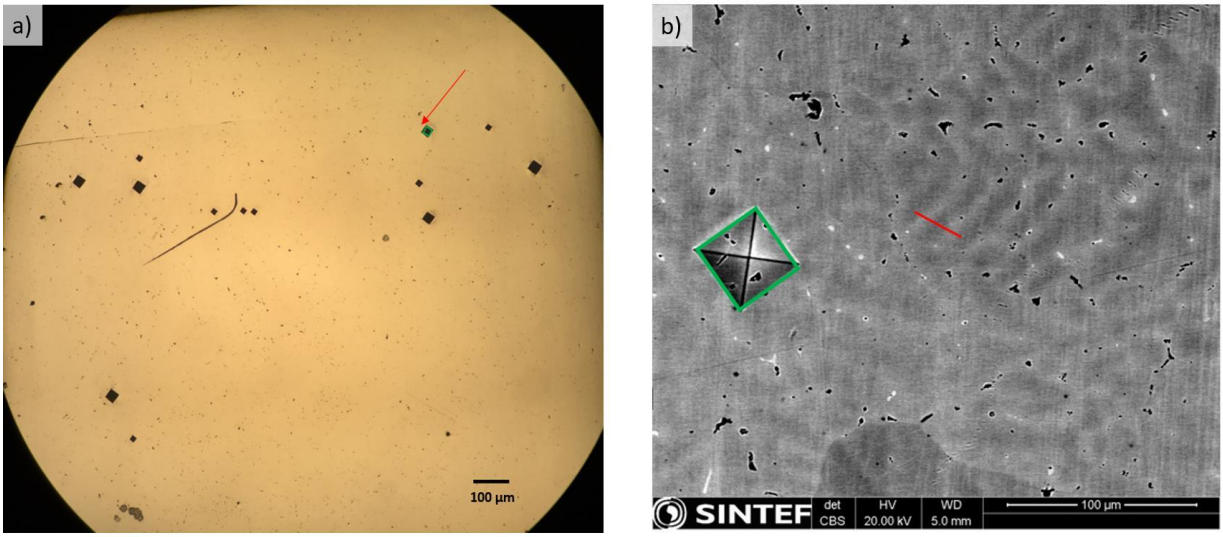

Fig. 4.2: **a)** Overview image from light microscope of Alloy B, showing the asymmetric hardness indention marks, with the region of interest indicated by the red arrow next to the green square. The images are mirrored as an artefact of the optical microscope. **b)** SEM image of the region of interest showing the same green indention mark as in a). The red line in the centre marks the desired area around indentation to extract as an FIB sample.

4.2.6 Removal of surface contamination

The samples were cleaned with acetone and subsequently isopropanol in an ultrasonic bath to remove surface contamination before SEM and MFM experiments were conducted. The FIB samples were plasma cleaned for 5 minutes before investigation.

4.3 Experimental methods

4.3.1 Hysteresis loop measurements

Hysteresis curves were measured by Vibrating Sample Magnetometer (VSM) technique on a PCM MicroMag 3900 instrument. The preparation goal for this experiment is to make an approximately cubic sample to avoid demagnetizing effects and check its isotropic properties. The instrument can only measure one direction of the sample at a time. The maximum weight for each sample was set to 5 mg, due to the saturation level of the instrument and a limitation of the relatively weak field that can be applied to strongly magnetic sample. Mass reduction is required to not saturate instrument by maximum field strength applied to the sample.

The sample was mounted to the vibrating tip with silicon grease and the position of the sample was calibrated for the instrument. The position in x-direction was calibrated by a minimum field for the sensors on each side. The optimal position in y- and z-direction was calibrated when the sensors were measuring a maximum field. When the sample was mounted and the position was calibrated, the magnetic field strength for the measurement was set. The goal was to saturate each sample and it was acquired when no changes in magnetic moment was observed with an increasing applied field. This field strength was set as maximum for the experiment.

The applied field was measured in Oersted [Oe] and the magnetic moment in [emu], as default settings for the magnetometer. These units were converted to SI magnetic field strength [A/m] and mass magnetization [$A \cdot m^2/kg$] respectively. For the latter conversion, each sample was normalized by its mass and the experimental data was plotted with Origin.

4.3.2 MFM measurements and analysis

The MFM maps were recorded on a JPK NanoWizard 4.0 Scanning Probe Microscope with an external field of 0.58 T applied to the sample and a scan height of 200 nm above the surface. A two-scan method was utilized to remove topological contribution to the force map.

Line profiles of the domain patters were created using JPK Data Analysis software, and the plots were exported as image files. The average domains spacing was calculated by dividing the measured distance by the number of magnetization peaks.

4.3.3 SEM and EDS analysis

Two SEM instruments were used to study microstructure and elemental analysis with EDS. A Hitachi TM3000 SEM was used with an acceleration voltage of 15 kV and the EDS mapping and quantification was

conducted with Quantax 70 system from Bruker Ltd. For Alloy A, this was the only instrument used. EDS analysis was performed across the samples for 25 random locations in the bulk material and the average composition was calculated with standard deviation for the two phases present.

The same method and instrument were applied for Alloy B. In addition, an SEM with a Field Emission Gun (FEG) was used to perform measurements at higher energy resolution. The measurements were conducted at SINTEF on a FEI Nova NanoSEM 650 with an acceleration voltage of 20 kV. As compositional gradients were found to be extensively present in the alloy of this composition, line scans were widely used in addition to EDS maps to better visualize and determine trends along a cross section. The EDS line scans were checked in accordance with the EDS maps and data from randomly measured regions, to evaluate how representative the data were for the sample as a whole.

4.3.4 EBSD

The preparation for these experiments started with powder XRD experiments to obtain information about the crystal structure of the sample. The EBSD software, AZtecHKL, requires a list of plausible phases in the specimen in the format of Crystallographic Information Files (CIFs) to match the experimental Kikuchi patterns. Hence, the XRD results were the basis for writing these CIFs, which closely matched the XRD pattern and the composition of material obtained from EDS. The models describing structure of investigated materials should take into account partial occupancy on the atomic sites, but the AZtec software would only accept CIFs with fully occupied sites. Therefore, alternative structures were suggested by the author at SINTEF using VESTA V4.3 software. The structures added to the phase list were a $L2_1$ type, a B2 type and a simple BCC structure with lattice parameters of 5.8 Å, 2.9 Å and 2.9 Å, respectively, although they did not match exactly the EDS data.

EBSD experiments were conducted on a FEI Nova NanoSEM 650 instrument to obtain the crystallographic orientations for grains near the surface of the sample. The sample holder was tilted by 70.5 degrees, which is the optimal angle for diffraction contrast. All raw files were exported from AZtec, line plots as .cvs files and plotted in Origin, and the EDS maps were saved as image files due to lack of access to the analysing software. The crystallographic orientations of grains were found by manually examining the EBSD results in form of Inverse Pole Figure (IPF) maps for x-, y- and z-direction. Combining these three maps for each crystal grain, the relative orientation to the EBSD detector was found. The Vesta software was used to virtually rotate a cube and subsequently make drawings of this cubic orientation on EBSD map. This was done in order to provide an illustration of grain orientation for the reader. It is possible to use a software to find these crystallographic orientations more accurate and faster, but the lack of access to such a software made manual fit a suitable alternative. Examples of such IPF maps can be seen in Fig 4.3a-c. The IPF colour key in Fig 4.3d relates each colour to an orientation and green arrows in Fig 4.3e show the coordinate system relative to the sample.

The IPF map in z-direction has the same relative orientation to the sample as the MFM and SEM images. Hence, this direction was used to correlate the EBSD results with the results from the two other instruments.

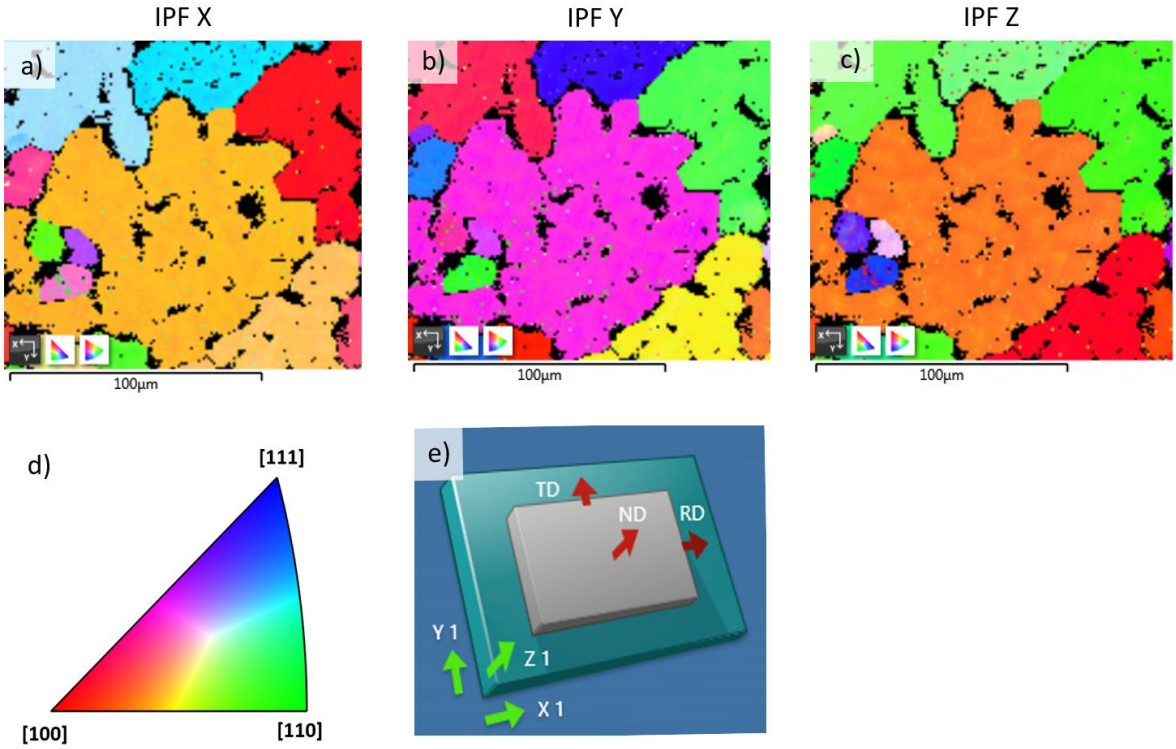

Fig. 4.3: a) IPF map in X direction. **b)** IPF map in Y direction. **c)** IPF map in X direction. **d)** IPF colour key figure copied from[32]. **e)** An illustration of the EBSD sample holder with the respective coordinate system for the IFP maps. The figure is a print screen from the AZtecHKL software.

4.3.5 Correlation of EDS analysis with MFM data

The indentation marks were utilized for area-specific measurements across the instruments. Fig 4.4a is an example, which is showing the MFM cantilever on the left of the indentation mark, captured with the optical microscope set on the instrument. The same indentation mark is shown in an SEM image in Fig 4.4b. To obtain the chemical content from the region measured in MFM, a low magnification EDS map with an acquisition time of 1 hour was performed. However, the resolution was not adequate due to the sample drift over such long acquisition period. Therefore, elemental EDS maps were recorded at fixed magnification of 4000× and acquisition time of 700 seconds. The magnification and acquisition time were optimized for mapping the region of interest, with sufficient contrast to separate two observed phases. An example of the acquisition time calibration is shown in Fig. 4.4d. The elemental maps for aluminium were used as reference, due to its big compositional variation between the two phases. The EDS maps were stitched together from the regions indicated by different coloured squares in Fig. 4.4c and subsequently scaled to match the

magnification of MFM maps. The results from the separate microscopes were correlated by overlapping the measurements from the exact same areas.

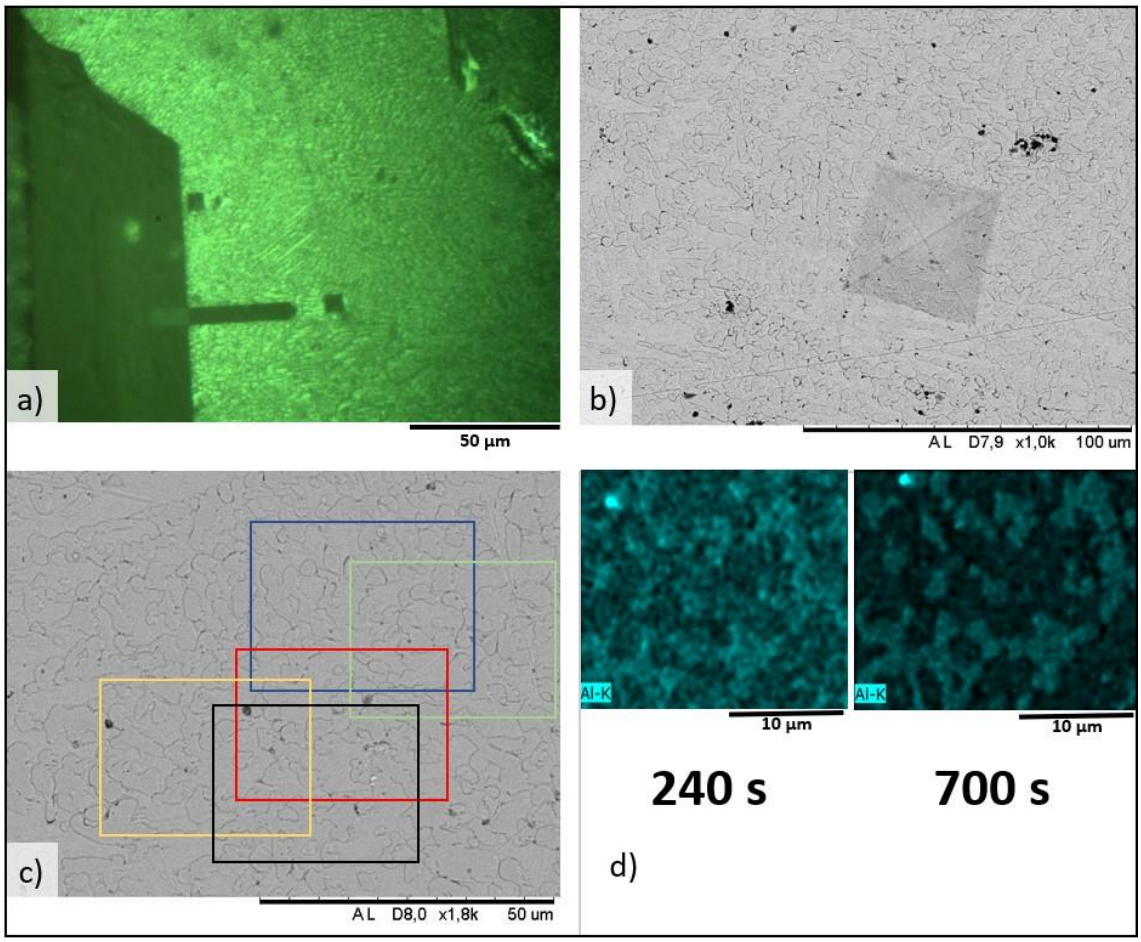

Fig. 4.4: a) Optical image from MFM showing the cantilever next to an indentation mark. **b)** An SEM image of the corresponding indentation mark. **c)** The area of each recorded EDS map surrounded by rectangular frames of different colour. **d)** Two Al EDS maps of the same area, but with different times of acquisition.

The MFM results were analysed by creating a histogram of the measured area in the JPK Data Processing software. The data were extracted and plotted in OriginLab Origin software, and a deconvolution of the histogram into two peaks was done to evaluate the relative difference between the magnetic phases. The procedure in Origin was executed with the following sequence: Peaks and Baseline – Multiple Peak fit - Open dialogue – Gaussian peak – Fit until converged.

4.3.6 TEM operation and SAED indexing

For normal TEM mode, a JEOL JEM-2100F with an acceleration voltage of 200 kV was used. The TEM used was operated by Anette E. Gunnæs and Phuong D. Nguyen in accordance with the author's objective and intention. The author was present and involved in the experiments.

Selected area electron diffraction (SAED) patterns were acquired for each phase to determine the crystal structure. The diffraction patterns (DPs) were captured along zone axes and at different tilt angles by following the Kikuchi lines from one major orientation to another, while keeping track of the tilting sequence and angles between each DP. Great care was taken to make sure the SAED was obtained from the same region when tilting the sample. The elemental composition was analysed by point EDS for the observed phases at several locations, and the average compositions were calculated.

To index the experimental SAED patterns, their symmetry was evaluated and calculating ratios of the reciprocal distances were calculated. The diffraction patterns were analysed with Digital Micrograph V3.43. Several diffraction spots along the same line were used to reduce the error doing the analysis. In order to maximize the contrast to visualize any low intensity spots, Diffraction Tools – Reveal weak reflections option was selected in the software. The ratios of the d-values were calculated as described in the theory section 2.1.6 and checked accordingly with a table of ratios for some common structures[33, 34]. The angle of tilting was used to achieve a complete match of all diffraction patterns to the proposed structure.

Simulation of SAED pattern for different structures was obtained with the Jems V4.8 software by importing the particular structure as a CIF file and orienting the structure with operations: right click the visualized model – show SAED pattern.

4.3.7 STEM and HR imaging and data processing in Digital Micrograph

For High Resolution (HR) imaging, a FEI Titan G2 60-300 operated at 300 kV in STEM mode was used and operated by Patricia A. Carvalho. The HR-images captured were drift corrected by the Velox software on the instrument.

To study local trends in the intensities in the HR High Angle Annular Dark Field (HAADF) image, line profiles were drawn along the atomic columns in the Digital Micrograph software. The process was acquired by right clicking on the image and using command “draw line profile”.

Fast Fourier Transform (FFT) was performed on the HR HAADF images to obtain DP and evaluate the crystal structure of the specimen with the same software. Further, inverse FFT was performed on selected diffraction spots. The procedure was done on a HR HAADF image by operations: Process – FFT – right click on DP – apply masks – select the diffraction spots of interest – inverse FFT. The method provides information of what areas in the HAADF image are contributing to the selected diffraction spots.

4.3.8 Lorentz Microscopy

4.3.8.1 Fresnel mode and domain wall identification

A FEI Titan G2 60-300 operated at 300 kV was used for Lorentz Microscopy (LM). The microscope was set up in Fresnel mode with the objective lens at zero applied field. To identify the domain walls in the specimen, images were captured for over- to under-focus of the sample on the lowest magnification possible. When the beam is defocused, domain walls will appear as dark and white lines and with opposite contrast at the focus shift. Any lines not obeying this inverse contrast change are not domain walls. Additional validation of the domain walls was obtained by not observing the lines when the electron beam was in focus.

4.3.8.2 Observation of domain wall motion

To observe the movement of the domain walls as a function of applied magnetic field, the defocus was kept constant making the domain walls visible. The objective lens then was turned on and the field was increased from 0 to 5% of its maximum applied field over a period of 105 seconds with a linear rate of increase. The increasing magnetic field caused the domains to align, and the movement in the domain walls could be observed. One image was captured every 1.5 seconds, to acquire a total of 70 images of the domain wall movement. When the Titan microscope runs in normal STEM mode, the objective lens is at 88 % of its maximum applied field strength, which is approximately 2 T. Thus, in an assumption of linear dependency, maximum field corresponds to about 2.3 T.

4.3.9 Powder XRD, modelling of possible structures and simulations

Powder XRD was conducted on alloy B using a Rigaku MiniFlex Benchtop XRD with Cu K-alpha and beta radiations. Fragmentation of the metal was achieved by milling it with pestle and mortar.

The XRD measurements were carried out with and without X-Ray Fluorescence (XRF) mode on the instrument. The XRF mode was found to give the best signal to noise ratio and was thus used for obtaining optimal results. Heat treatment of the fragmented material was carried out in a sealed, low vacuum quartz ampule for 30 min at 300 °C. This was an attempt to reduce any deformations caused by the mechanical processing of the sample. However, this heat treatment was only conducted once since there was no observable effect with respect to the broadening of peaks in the diffractogram. The Cu K-alpha radiation was filtered in the diffractogram by DIFFRAC.EVA software from Bruker.

The experimental XRD results of alloy B indicated a B2 phase. However, a similar alloy from the Magnificent project was found to have a mixture of B2 and more ordered $L2_1$ phase. Thus, the possibility of this $L2_1$ phase being present in the alloy B was taken into consideration. In order to investigate whether the experimental XRD results could fit an $L2_1$ phase, the structure factor for this phase was calculated and evaluated.

The VESTA software was used to model the $L2_1$ and B2 structures and additionally to simulate XRD patterns for the given models in order to compare them to the experimental results. These models aimed to match both the experimentally obtained XRD and the average composition obtained from the EDS analysis. At this point, it was not possible for the author to examine the samples in the TEM and thus this method was applied. The results are presented in Appendix A.

Chapter 5

Results and discussion

This chapter is divided into three sections. First, the average magnetic results for Alloy A and B are presented, followed by separate sections for the results of Alloy A and Alloy B. The findings are discussed throughout the chapter.

5.1 Hysteresis measurements

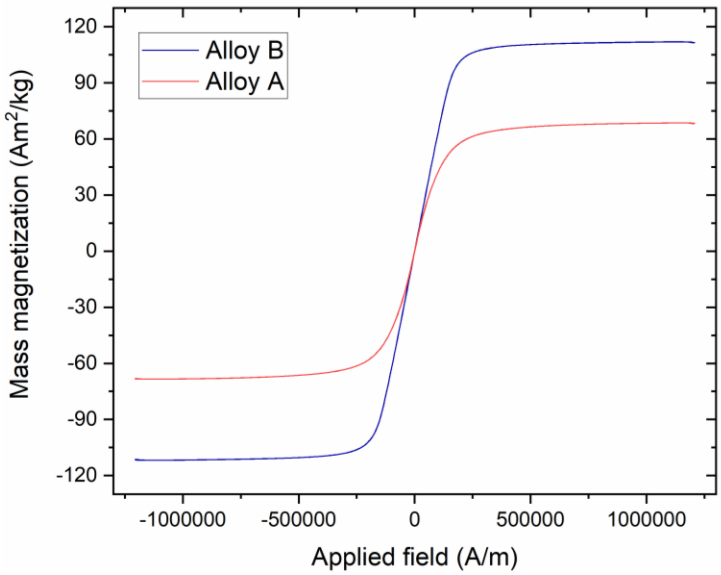

Fig. 5.1: Hysteresis curves for three measured samples, plotted with the same axis scale.

According to Fig. 5.1, Alloy B has the highest saturation magnetization of the two samples with a value of 112 A·m^2/kg. Alloy A has the lowest mass magnetization saturation of 68 A·m^2/kg.

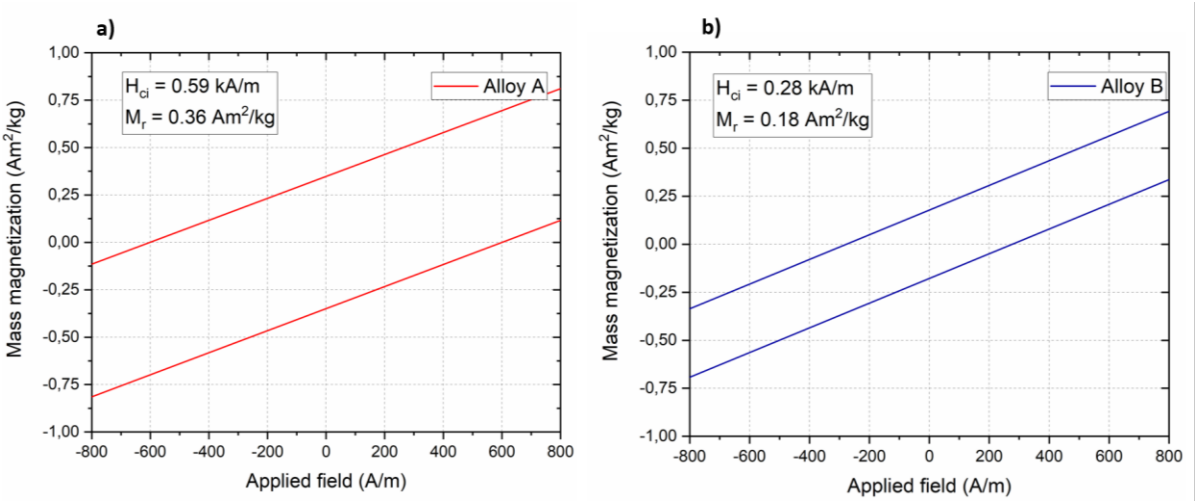

Fig. 5.2: a) Hysteresis curves for Alloy A. b) Hysteresis curves for Alloy B. The axes are scaled to observe the region of interest for the intrinsic coercivity and the remanent magnetization, which values are shown in the upper left corner of each plot.

With the ambition of developing a magnet as soft as possible, Alloy B seems to be the best candidate with the lowest intrinsic coercivity of 0.28 kA/m. This is the alloy with the highest composition of Al and Mn. Both alloys are magnetically soft, in terms of the general characterization, with an intrinsic coercivity below 1000 A/m.

The VSM results represent the average magnetic properties for the alloys, measured for one direction. Other experimental data reveal that there is more than one phase present in each of the alloys. This fact must be taken into consideration when evaluating the hysteresis loop results. There may exist a desired magnetic phase that is only a minor fraction of the multiphase alloy and is dominated by the other phases in the VSM result. More detailed investigation with other techniques is needed to separate distinct magnetic phases that are chemically or structurally related.

In this experiment, only one direction was recorded for each of the alloys. As magnetic properties can vary for different crystallographic orientations, this may have an impact on the result. Repeating the experiment with one measurement along all directions of the cubic sample is preferred but was not possible to carry out at the time. With regards to the relatively small sample dimension, there may not be enough randomly oriented crystal grains along the measured direction, to give a good representation of the average magnetic properties, compared to a bulk size measurement. Yet, there is a limitation in the maximum magnetization measured by the instrument.

VSM is the only method in this thesis that reports the important quantities, coercivity and saturation, related to characterizing magnetic softness and some types of energy loss in use for industrial application. It gives

the average information about all existing phases in the material. To distinguish between different magnetic phases in the material, more detailed methods are needed.

5.2 Alloy A

The results presented in this section is for Alloy A, with a nominal composition of $FeNiCoMn_{0.29}Al_{0.29}$. Mainly two phases were observed in this alloy, in addition to small particles of aluminium oxide (alumina). An SEM backscattered electron (BSE) image of the alloy is presented in Fig 5.3a. The figure reveals the microstructure of this sample. The dark square in Fig 5.3a represents the area of an acquired EDS map analysis. This elemental analysis is given in Fig 5.3b-f with an EDS map for the individual elements in this region.

The elemental map for Al in Fig b shows an uneven distribution in the measured area. Such distribution of Al is representative for the whole bulk sample and was associated with a chemical phase, higher in Aluminium content. The bright spot in the Al map illustrates an alumina particle that can be related to the dark spots in BSE image. By studying the separate EDS maps, such as in Fig 5.3 b-f, one trend was pointed out. A systematic distribution of higher Al content opposite to areas of higher Fe content. This is illustrated in Fig 5.3g by the elemental map of Fe and Al overlaid with 50 % transparency, to visualise the anti-correlation. Elemental analyses conducted over larger regions and for multiple samples substantiate the trend in the presented results. Hence, these two phases are referred to as the Al-rich and Fe-rich phase.

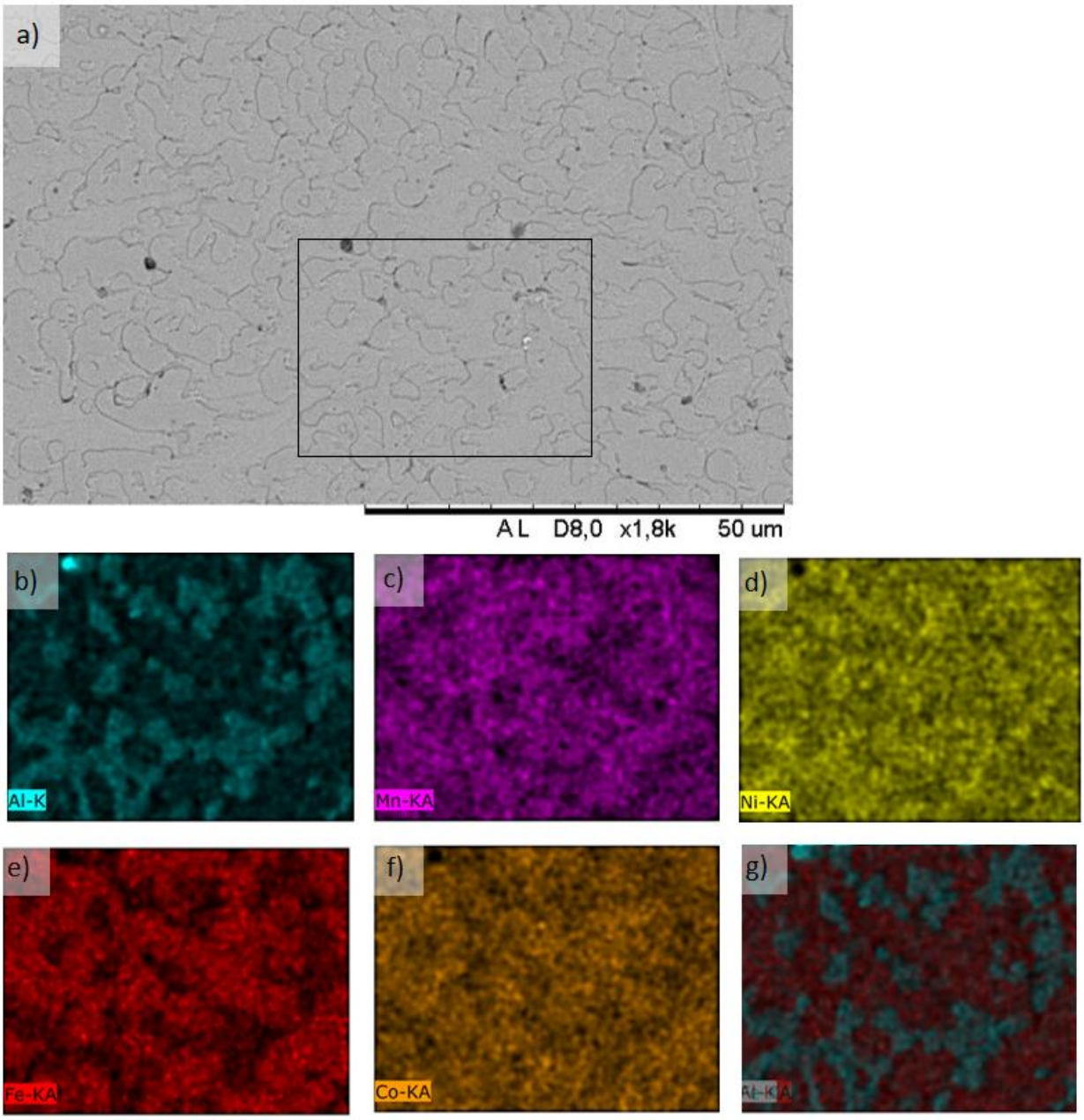

Fig. 5.3: a) SEM BSE image with the EDS map for each constituent element. **b)** Al, **c)** Mn, **d)** Ni, **e)** Fe, **f)** Co and **g)** Fe and Al overlaid with 50% transparency, to visualize the anti-correlation.

Table 5.1: Average compositions for the two phases observed in Alloy A

at. %	Fe	Ni	Co	Mn	Al	Formula
Al-Rich phase	22.2 (±1.4)	24.4 (±1.0)	23.1 (±0.7)	12.0 (±0.6)	18.4 (±0.9)	$FeNi_{1.1}CoMn_{0.5}Al_{0.8}$
Fe-Rich phase	28.5 (±1.0)	22.7 (±0.5)	26.2 (± 1.0)	12.1 (±0.9)	10.5 (±1.0)	$FeNi_{0.8}Co_{0.9}Mn_{0.4}Al_{0}$ .4

Table 5.1 shows the average EDS data for two phases obtained from SEM measurements. The measurements were performed at 25 random positions for each phase. The composition is given in atomic percent with standard deviation next to the respective chemical formula. The chemical formulas were normalized with respect to Fe content and rounded to one decimal point. It should be noted that both the Fe-rich and Al-rich phase are in accordance with the definition of a HEA, as all five elements are within the interval of 5-35 at. %. The results show a minor variation of Ni and Mn for the distinct phases, while the Fe and Al concentration differs the most. Co differs by 3 % for the two phases with a tendency to follow the Fe content, as can be observed by comparing Fig 5.3e-f.

The EDS and microstructure analyses raised questions about the distinct magnetic properties of the Fe-rich and Al-rich phases in relation to each other, as the VSM result represents the average of these chemical phases. The same region was located in the MFM measurement, by using characteristic indention marks to navigate. The MFM map has no contribution from topological features that could be used as reference points in the SEM. Therefore, the EDS map of Al was utilized to match the precise area for the two results, as the map showed a high contrast with sharp boundaries to the Fe rich phase.

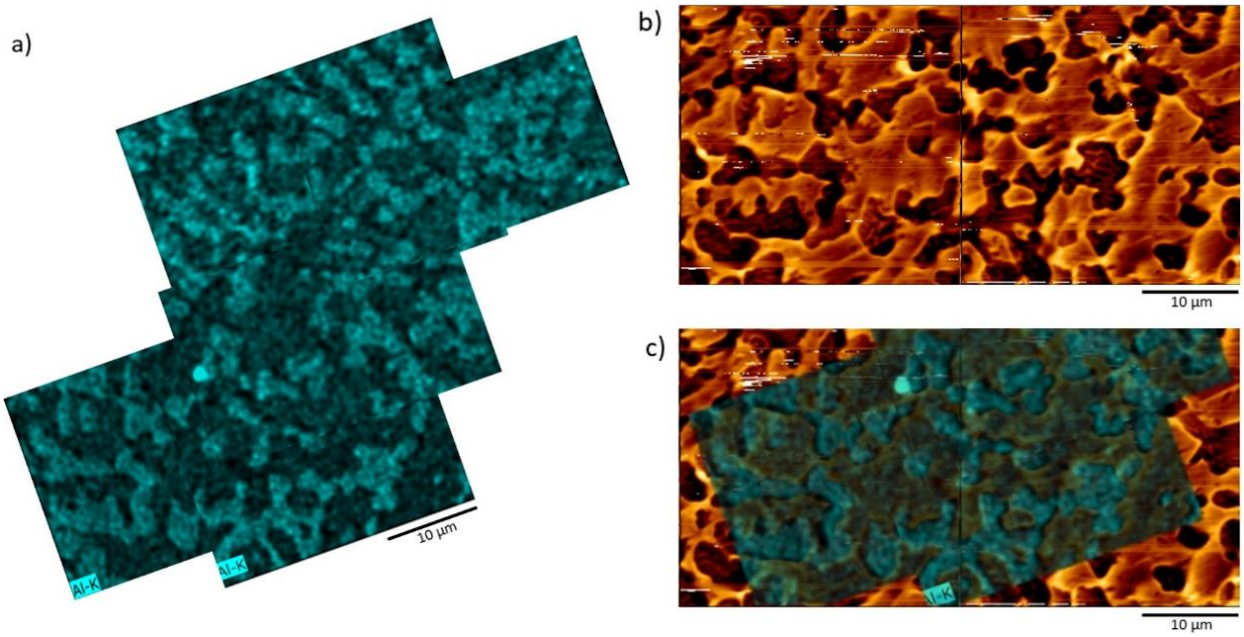

Fig. 5.4: a) Al elemental map from EDS, **b)** MFM map from the same region as the Al elemental map and **c)** MFM map overlaid with the elemental map, having 30 % transparency.

Figure 5.4a shows the EDS map of Al content, for the same region as the MFM result in Fig 5.4b. The Al map is rotated due to a slight variation in orientation, resulting from the mounting of the sample in two instruments. Fig 5.4c shows the MFM measurement overlaid with the elemental analysis from SEM. The result reveals a significant correlation between the compositional and magnetic phases in Alloy A, with

close to perfect overlapping of the EDS and MFM maps. The Al-rich phase is corresponding to the darker domain areas in the magnetic map of Fig. 5.4b. A darker region in the magnetic image means a stronger magnetic field. Hence, the Al-rich composition is magnetically stronger in comparison with the Fe-rich phase. Al is non-magnetic in its pure metallic form, nevertheless; the phase with enhanced content of Al has the stronger magnetic field. The dark areas in the MFM result show a stronger tendency to split into domain structure, best illustrated by the stripy pattern in Fig. 5.6a.

To quantitatively analyse the magnetic measurements, the difference in phase area was determined by deconvolution of the MFM histogram into two peaks.

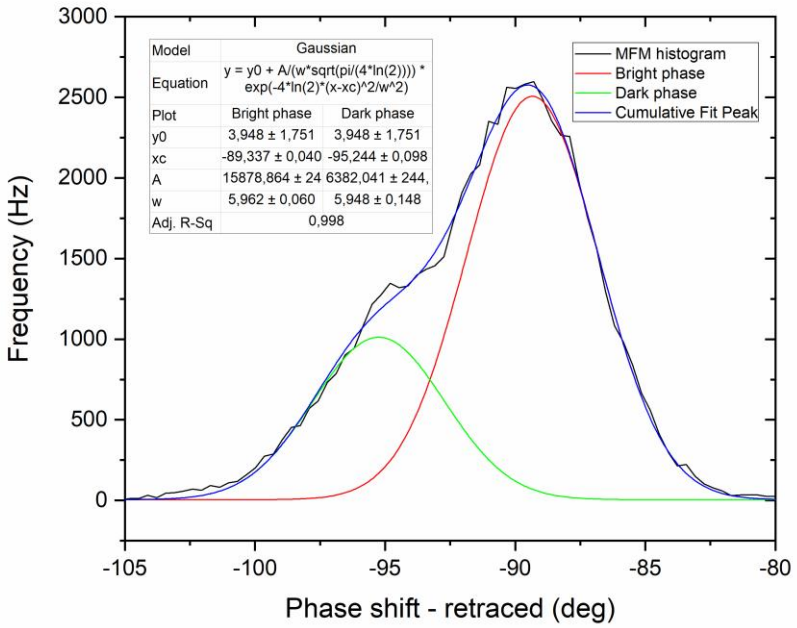

Fig. 5.5: MFM histogram and the deconvoluted peaks with the data set for the Gaussian curves in the upper left corner.

The deconvolution reveals two peaks with mean phase shifts of -89.3 and -95.5 degrees, which are related to the two chemical phases. The phase shift is proportional to the gradient of the magnetic force between the tip and the sample. A more negative phase shift, meaning stronger attraction of the magnetic tip[35], is associated with the dark areas in the MFM map, hence the Al-rich composition. This implies that the Fe-rich phase is magnetically weaker than the Al-rich phase.

The areas below the Gaussian curves (intensities) are 15878 and 6382 for the bright and dark areas in the MFM map, respectively. This is indicating a dominant mass fraction of the Fe-rich phase in the measured area. If this result is representative for the whole sample, this alloy is dominated by the magnetically weaker phase. This method can be applied as an estimate for obtaining the phase fraction for this alloy, if done extensively or for lower magnification to cover larger areas. However, this was not attempted in this thesis.

The experimental method's success was highly dependent on the hardness indentation marking, suggesting that this procedure should be applied in further work with a similar objective as in this study. The achievement of this experiment supports the idea of using only the constituent with the largest difference in atomic percent, to clearly visualize the correlation between the chemical and magnetic phases.

To extend the correlated study, a FIB sample was extracted from the same area in which the MFM measurements had been conducted, crossing a grain of Al-rich phase with Fe-rich phase on both sides. This is depicted in Fig 5.6, showing the corresponding area from the MFM result in a) localized in the FIB instrument in b). Fig. 5.6c shows deposition of carbon before sample extraction. Fig. 5.6d shows the area after ion milling with the hardness indentation mark above, and e) captures the lamella from a side view. Unfortunately, the FIB sample was lost when mounting it to the TEM sample holder. However, it demonstrates the technique of how to correlate an MFM measurement of a bulk sample to a TEM study.

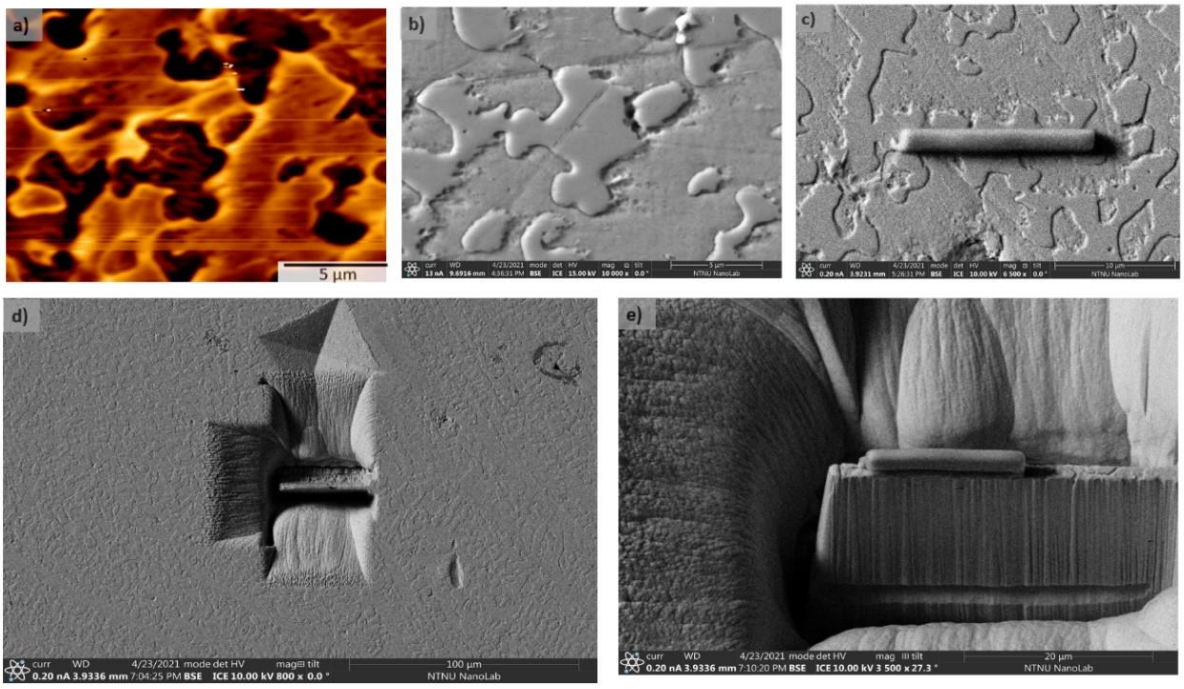

Fig. 5.6: a) The MFM map. **b)** The corresponding region from the FIB, BSE image. **c)** Carbon is deposited on the grain before ion beaming. **d)** An overview picture of the beamed area with the hardness indentation mark above. **e)** A view of the lamella before the extraction.

To obtain the crystal structure of the Al-rich and Fe-rich phases, a wedge sample from bulk material was prepared and the respective structures was determined by SAED in TEM. The two phases were recognised by DF and BF contrast and corresponding EDS analyses to that obtain from SEM.

5.2.1 SAD of the Fe-rich phase

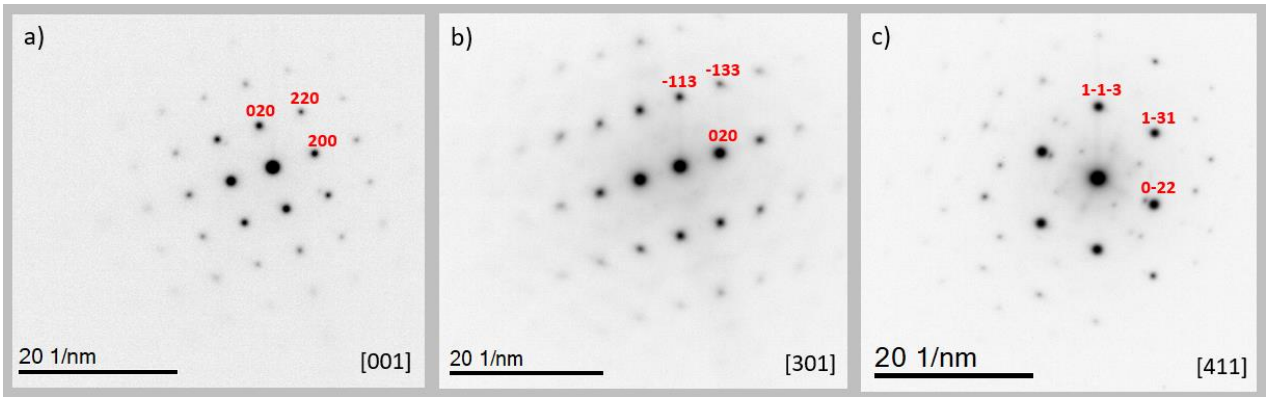

Fig. 5.7: Fe-rich diffraction patterns for different crystallographic orientations, indexed as a simple FCC structure. **a)** [001] direction, **b)** [301] direction, **c)** [411] direction.

The SAED patterns in Fig. 5.7 were identified as a simple FCC structure with a lattice constant of 3.6 Å. The diffraction patterns were obtained by tilting series within one crystal grain. The [411] direction in Fig. 5.7c reveals additional reflexes beyond the simple FCC matrix. This result indicates the presence of precipitates in the matrix of the Fe-rich phase and were observed in different grains of this phase. However, these were not identified and further TEM investigation is required.

5.2.2 SAD of the Al-rich phase

The crystal structure of the Al-rich phase was identified to match a B2 phase with a lattice constant of 2.9 Å. Published work for the $FeNiCoMn_{0.25}Al_{0.25}$ system has been reported as both a mixture of FCC + B2 and FCC + BCC. Yang et al.[36] observed a single phase B2 for the as-cast alloy, transitioning into a mixture of FCC + BCC phases after heat treatment and concluded that the B2 phase is a metastable phase. However, Li et al.[1] reports presence of FCC + B2 phases after annealing. The findings of Li et al. are similar to the result for the as-cast Alloy A presented in this thesis. The published articles differ in the annealing temperature and time, which could explain their different observations. Additionally, the reported alloys of Yang et al. and Li et al. have been synthesised by different methods, and neither of them are processed by laser metal deposition.

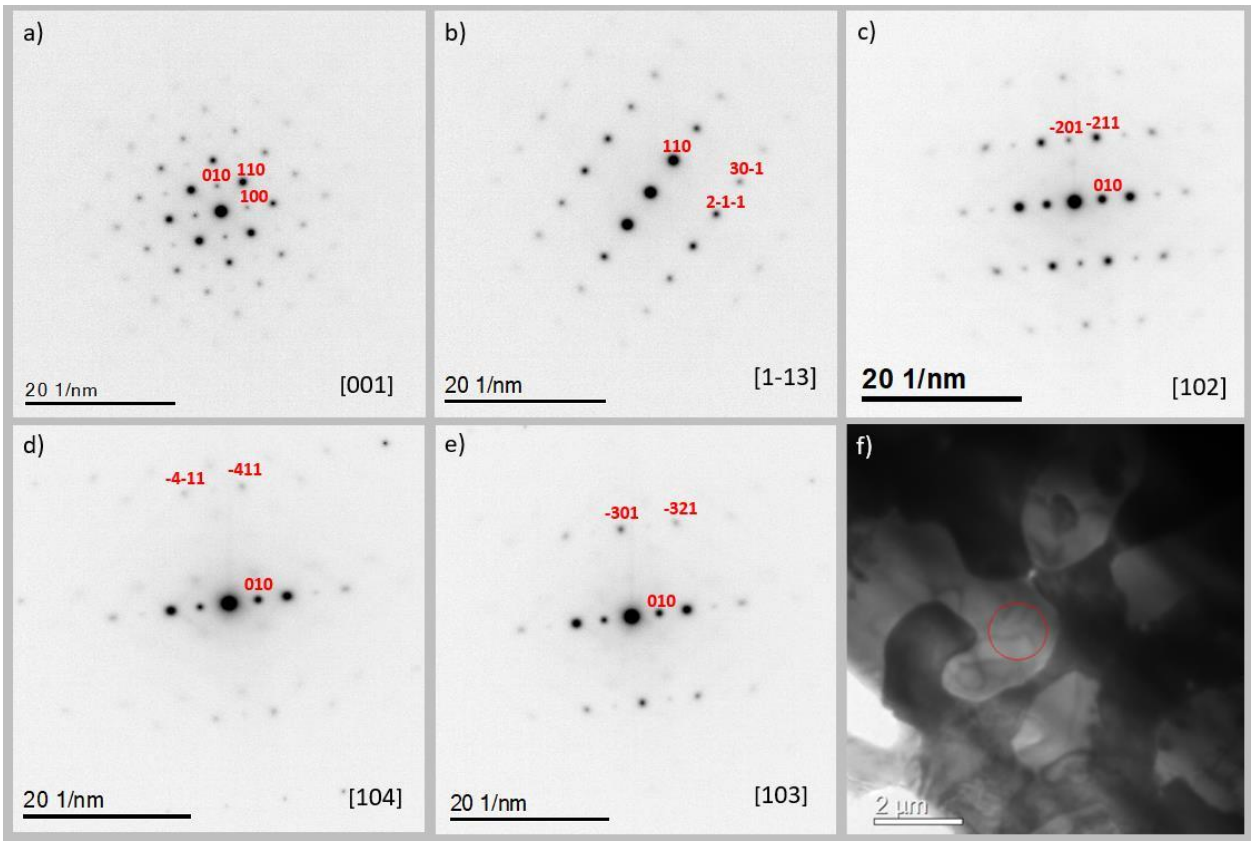

Fig. 5.8: SAED patterns for different orientations of the Al-rich phase, indexed as a B2 phase. **a)** [001] direction, **b)** [1-13] direction, **c)** [102] direction, **d)** [104] direction, **e)** [103] direction. **f)** A BF image of the sample with a red circle indicating the region of the selected-area aperture used for the diffraction series.

A study of the transition between the Al-rich and the Fe-rich phases and the grain boundaries was performed. A series of diffraction patterns were obtained along the red arrow illustrated in Fig. 5.9a. The sample tilt was kept constant and aligned to the [001] direction for the Al-rich phase, as shown in Fig. 5.9b. Fig 5.9c-f shows observed changes on the grain boundary, moving into the Fe-rich phase. In the middle of the Fe-rich phase, the [411] zone axis of a simple FCC was identified, as Fig. 5.9g shows. Fig 5.9h-k displays the observed changes from the middle of Fe-rich phase transition into the Al-rich phase, ending with the diffraction pattern in Fig 5.9l. A trend was noticed when studying this phase transition. The reflexes belong to h + k + l = odd for the B2 diffraction pattern was weaker towards the grain boundary to the Fe-rich phase. If these reflexes were of zero intensity, the diffraction pattern would be associated to a simple BCC structure (A2).

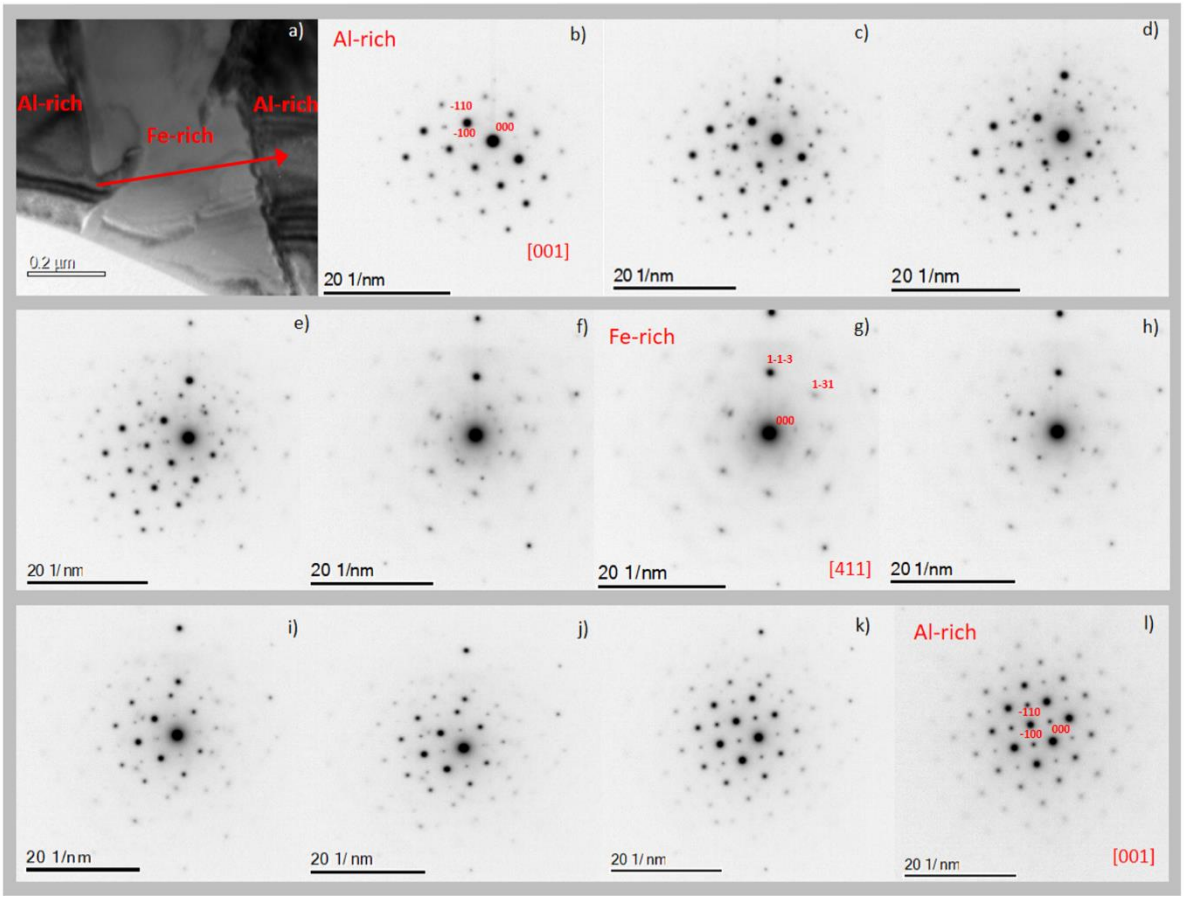

Fig. 5.9: a) Shows the region where the diffraction series are captured, and the path is indicated by the red arrow. **b)** is diffraction pattern from the starting point of the arrow. **c) – k)** are diffraction patterns along the arrow in chronological order, ending with the DP in figure **l**) at the tip of the arrow in a). Al-rich are indexed as a B2 type and the Fe-rich as a simple FCC.

This observation may indicate two things: One indication could be a reduced content of Al towards the Fe-rich phase. The elements except Al are transitions metals and close in atomic numbers. Hence, this could result in the two atomic positions in the B2 unit cell approaching the same number of electrons. Another possibility is that the Al content is evenly distributed in the phase, but more disordered in the crystal lattice towards the grain boundary. Both should lead to the observation of weaker intensities for these reflexes, as the structure approaches a simple BCC (A2 type). This can be observed by comparing the -100 reflex in Fig 5.9b, which is close to the grain boundary, with the same reflex in Fig 5.9l. This may suggest that phase stability of the B2 and BCC phase are close in energies. In relation to configurational entropy, the degree of ordering is higher for the B2 phase, which seem to be more favourable for increased Al content in this alloy.

5.3 Alloy B

The results presented in this section are obtained for Alloy B, which has a nominal composition of FeNiCoMn0.9Al0.9. This alloy is similar in composition and structure to the Al-rich phase in the Alloy A.

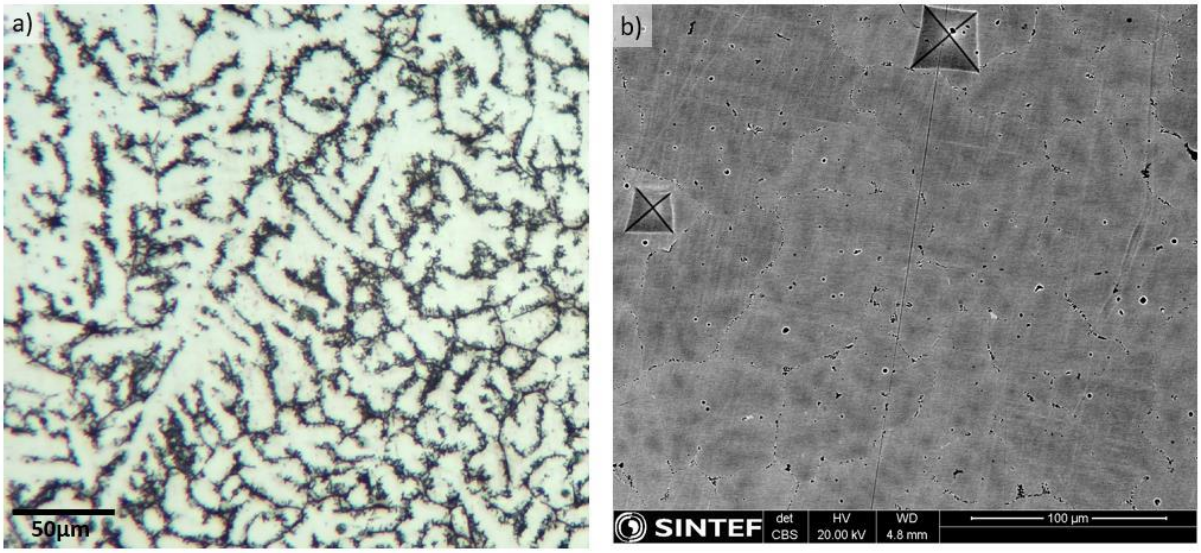

Fig. 5.10 a) An etched sample of Alloy B in light microscope. **b)** A non-etched sample of Alloy B in SEM.

Fig 5.10a reveals the dendritic microstructure of Alloy B, visible in the light microscope as a result of etching. The BSE image from Fig 5.10b shows a non-etched sample in SEM and two indentation marks. The contrast in this BSE image arises from a compositional gradient observed across the dendrites, from the core to the outer region. The dark spots which can be observed in Fig.10b is a Mn and Fe rich phase, that was systematically observed along the grain boundaries and between the dendrite arms. This phase is referred to as the Mn-Fe phase. Table 5.2 show the results of the EDS analysis obtained from the SEM of this alloy. A distinction is done between the core dendrite regions and the edges. The core regions were found to be rich in Al, where the Fe content was observed to be at the minimum. This is similar to Fe-rich and Al-rich phase in Alloy B, but in the case of Alloy A, this variation is observed within the crystal lattice. This is demonstrated by EBSD and STEM results presented later in this section.

Table 5.2: The average chemical formulas for phases in Alloy B normalized by Fe content

at. %	Fe	Ni	Co	Mn	Al	Formula
Dendrite core	16.0(±0.5)	20.9(±1.4)	19.0(±1.4)	18.1(±1.4)	26.0(±1.4)	$FeNi_{1.31}Co_{1.19}Mn_{1.13}Al_{1.63}$
Dendrite edge	20.5(±1.2)	17.5(±0.8)	19.1(±1.8)	20.9(±1.7)	22.0(±1.5)	$FeNi_{0.85}Co_{0.93}Mn_{1.02}Al_{1.07}$
Mn-Fe phase	37.9(±2.1)	5.7(±0.7)	15.5(±1.3)	37.1(±1.9)	3.8(±0.6)	$FeNi_{0.15}Co_{0.41}Mn_{0.98}Al_{0.10}$
Nominal	20.8	20.8	20.8	18.8	18.8	$FeNiCoMn_{0.9}Al_{0.9}$

Multiple powder XRD measurements was conducted for this alloy, in order to identify the structural phases in combination with the EDS analysis. The powder diffractogram was found to fit a B2 phase. No extra intensities beyond the B2 peaks were observed, despite the observed presence of the Mn-Fe phase in the SEM. A possible explanation for the absence of the Mn-Fe phase in the XRD results, could be the small phase fraction in addition to this phase being ductile. Hence, the mechanical pulverization for the power XRD may have introduced deformation in the lattice, leading to broader peaks. Combining such effect with the minor phase fraction of the Mn-Fe phase would make it difficult to distinguish from the background in the diffractogram. The XRD results of Alloy B is available in Appendix A.

The compositional variation observed in Alloy B is exemplified in Fig. 5.11. The Fig 5.11a shows a BSE with an arrow that indicates an EDS line scan, crossing two dendrite arms, which is plotted in Fig 5.11b. The line scan plot reveals the trend which was observed across the bulk samples of Alloy B, that Al and Ni correlate with each other and anti-correlate with Fe and Mn, whereas Co is homogenously distributed. The observation explains the contrast in the BSE image, by the lower average atomic number, mainly contributed by Al. In other words, the bright contrast in Fig. 5.11a corresponds to the areas with enhanced content of Fe and Mn, while the darker areas in the BSE image are associated with the increased content of Al and Ni. The red dotted line in Fig 5.11a illustrates a grain boundary, which was obtained by EBSD. The EDS line scan is according to the EBSD data measured within one grain.

The chemical variation in the EDS map is indicating a dendritic structure with a coring effect. As one can see in the grain of where the EDS line scan is taken in Fig. 5.11a, the dark colours resemble that of a tree, which the word dendrite originates from. The inner core is dark and is branching out with white bright contrast in between. This observation could be explained in the following way: The Al-enhanced phase is the first to solidify with the rest of the composition remaining in melt. When the crystal continues to grow from the core towards the liquid, which is cooled down, the crystallization at the solid-liquid interface happens without diffusion. Diffusion through the solidified crystal core to the liquid interface requires considerable time. Thus, the crystallization at the interface occurs under non-equilibrium conditions, and the alloy develops enhanced content of the phase with the highest melting point at the core, and vice versa closer to grain boundaries. A dendrite grows until it meets another arm, grain or stops when another phase starts solidifying. For Alloy B, the content of Mn and Fe is increasing in the liquid, as more Al and Ni has solidified in the core dendrite. Therefore, the Mn-Fe phase is found in-between dendrite arms or at grain boundaries.

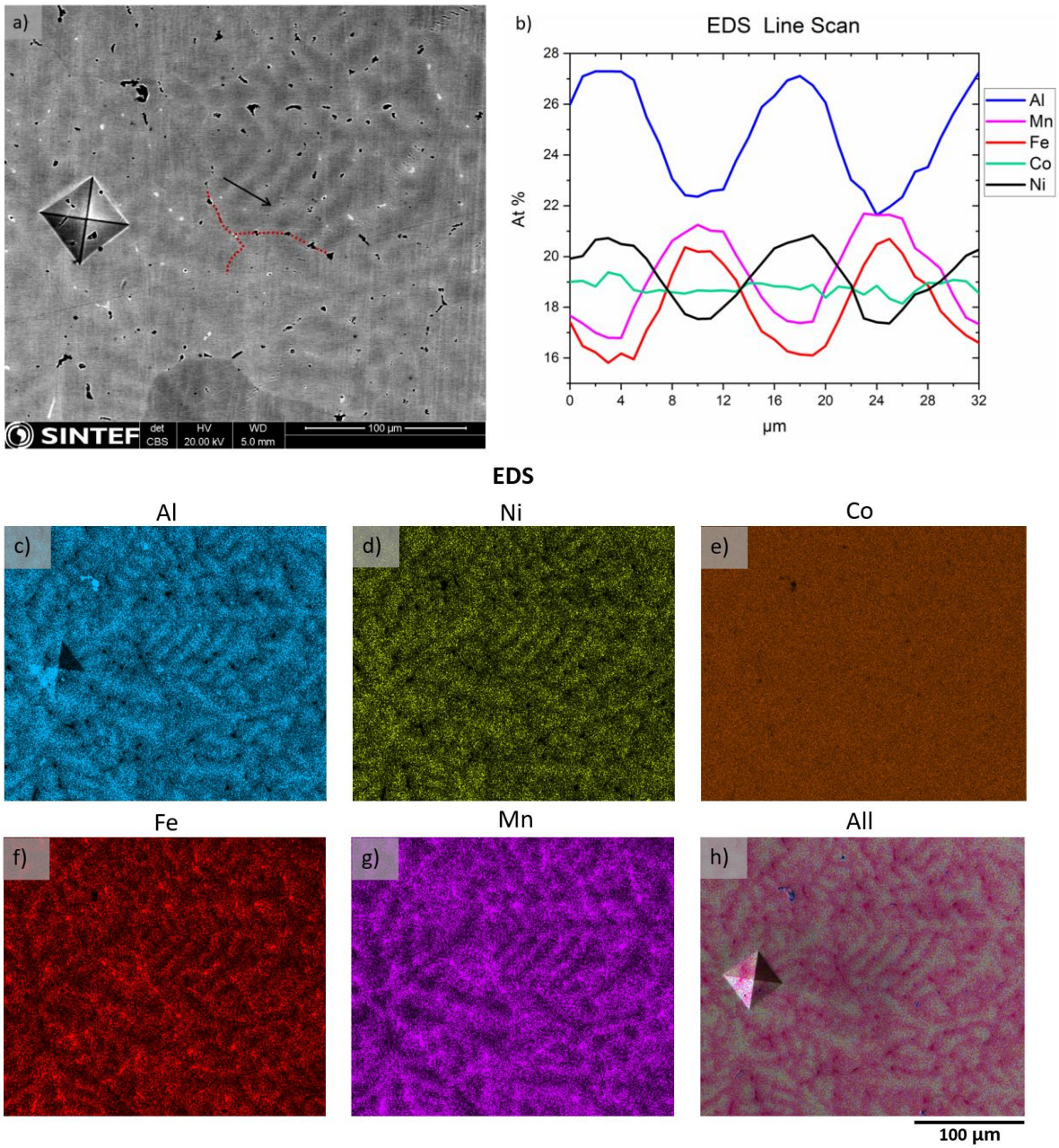

Fig. 5.11: a) SEM BSE image with an arrow showing the position of the elemental line scan. **b)** Element contents along the line scan. **c)-g)** Elemental maps of Al, Ni, Co, Fe and Mn, respectively. **h)** A combinational SEM BSE image.

The composition in the dendrite core is $FeNi_{1.31}Co_{1.19}Mn_{1.13}Al_{1.63}$ compared to a content of $FeNi_{0.85}Co_{0.93}Mn_{1.02}Al_{1.07}$ at the dendrite edge, when normalized by the Fe content (see Table 5.2). The coring effect should be possible to remove by heat treatment with a temperature below the melting point. This would allow diffusion in solid state to take place, which did not have time to happen in the solidifying process. Annealing is suggested for further work to obtain a more homogenous phase composition, which is desired for the end product in applications.

5.3.1 Microstructure analysis of an etched sample of Alloy B

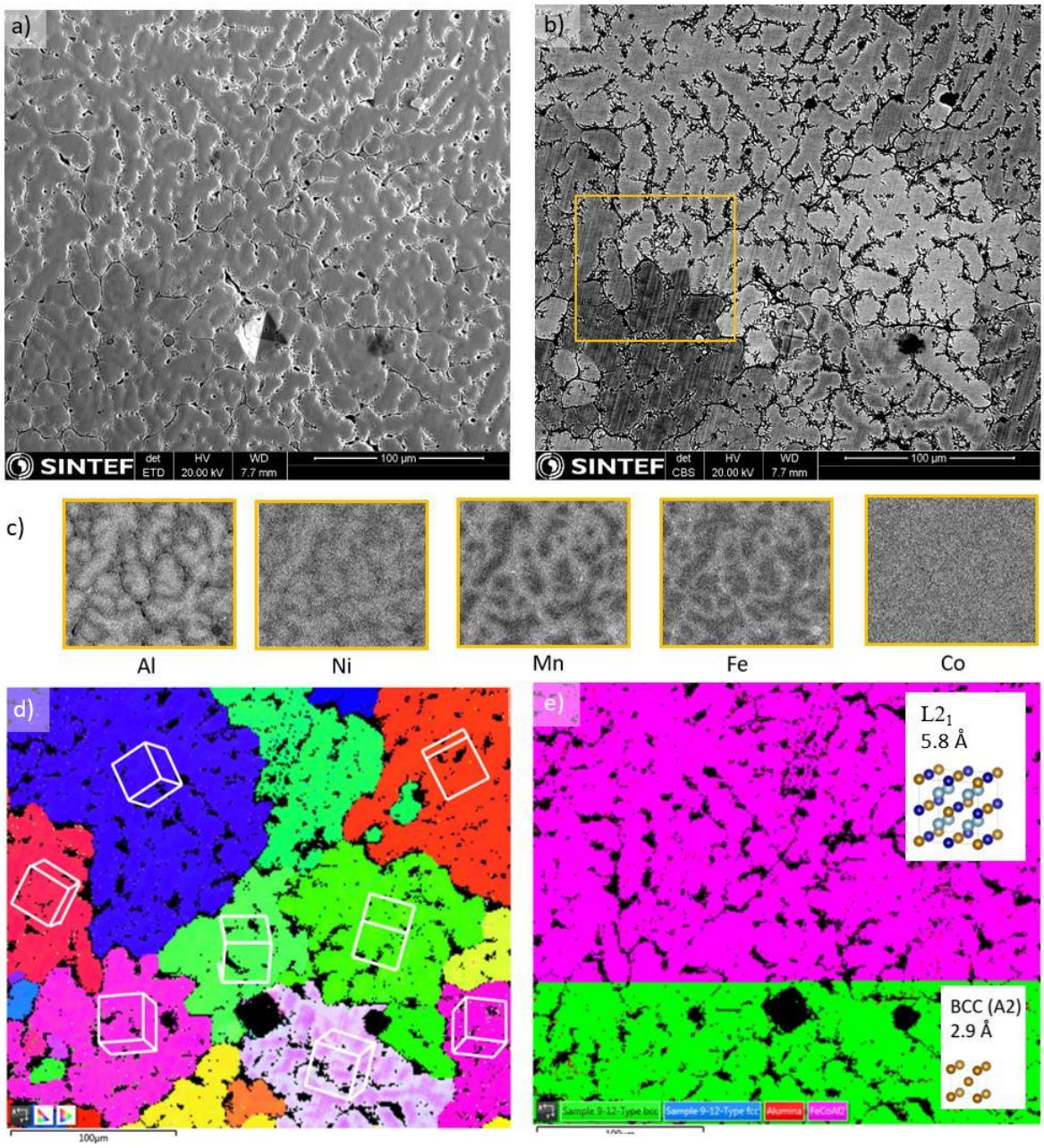

Fig. 5.12: a) Secondary Electron image from SEM. **b)** BSE image for same region as in a). **c)** EDS maps from the orange square region in b). **d)** EBSD map from same region as a). **e)** The phase map for EBSD data in d).

The SEM image in Fig. 5.12 a) shows the microstructure of an etched sample of Alloy B taken with the secondary electrons (SE) detector, while b) is the same area observed with the BSE detector. The EDS map is obtained from the orange square in Fig 5.12b and the individual EDS maps are given in Fig 5.12c. By correlating the EDS maps to the same area in the EBSD, it is clear that the contrast in the BSE image is related to the different crystallographic orientations, and not chemical content. This may indicate and

electron channelling effect, allowing the electron beam to travel deeper into the crystal for some orientations, which results in lower number of backscattered electrons. Such orientations are usually closer to major zone axis with low density of atoms. In this case, the darkest grain is along the [113] direction, whereas the brightest contrast is for a grain oriented close to the [120] direction offering most reflecting area. The majority of the grains have slightly darker contrast in the core area compared to the edge. This feature correlates well with the EDS maps of the un-etched sample showing locally enhanced Al and Ni content anti-correlating with Mn and Fe content. However, there was not observed any obvious electron channelling contrast in the BSE image for the un-etched sample in the same instrument. Etching this material thus helps revealing grains and orientations by the contrast.

Fig 5.12e is the phase map for the EBSD result, illustrating the identified phases by the software and their distribution in relation to the EBSD map. The colour in the phase map was suddenly switched from pink to green and is not in accordance with the grain boundaries obtained from EBSD. There is no reason to believe that this phase map is correct, however, it is an evidence that the software was not able to clearly distinguish the two phases, namely the simple BCC and full-Heusler structure with lattice constants of 2.9 Å and 5.8 Å, respectively. An explanation of why the software is not able to separate these structures, is their close relation by higher degree of ordering. If one fully disorders all atoms in the $L2_1$ structure, the symmetry will be reduced to that of the simple BCC structure with half of the lattice constant. Hence, it is shown that this method is not sensitive to the chemical ordering. Both phases had the same 87 % match with the corresponding models in the phase map.

There are some colour variations within the grains, which suggest a local alteration in the crystal lattice orientation. As the colours in the EBSD map illustrate crystallographic orientation, the results suggest that the crystal lattice is bent in the core region, relative to the edges. The phase map, however, shows no variation. This colour difference is more evident in the light-coloured grains and is not, or just barely visible in the grains with more intense colour. This was found to be due to the colour saturation, which is difficult to correct without access the EBSD software. By comparing the IPF maps of the same grains, this variation was found to be in the core of all dendrites. This local orientation difference is associated with the chemical variation from the core to the outer dendrite area discussed earlier, where the Al content was sufficiently higher in the core region. Al is the element with largest metallic radius of 143 pm, compared to Mn as the second largest with 127 pm and Ni with the smallest radius of 124 pm. According to Vegard's law, the lattice parameter should increase with enhanced content of Al in the solid solution. This could lead to a bent crystal lattice and thus a small shift in the orientation.

An alternative explanation could be that there is no variation in orientation from core to outer dendrite, but the that the software misinterprets a variation in the lattice parameter as a small angle tilt. If so, this may be explained by the software's ability to recognise the Kikuchi bands, which determines the resolved orientations. A larger crystal lattice will result in a narrower Kikuchi band, which could affect the matching simulated Kikuchi patterns to the experimental ones. The software uses a band width that is based on the given model from the structures in the phase list. If the experimental band width is increasing or decreasing,

while the software utilizes a constant band width, the angle determination could be offset, and thus result in a misinterpreted orientation. To verify this, a new run with additional structures, e.g., with lattice parameters of 2.91 Å and 2.89 Å for simple BCC phase could be done after adding them to the phase list. In any case, the observed dendrite feature in the EBSD map is linked to the chemical variation of Al and its large radius.

5.3.2 Correlation of MFM and EBSD results

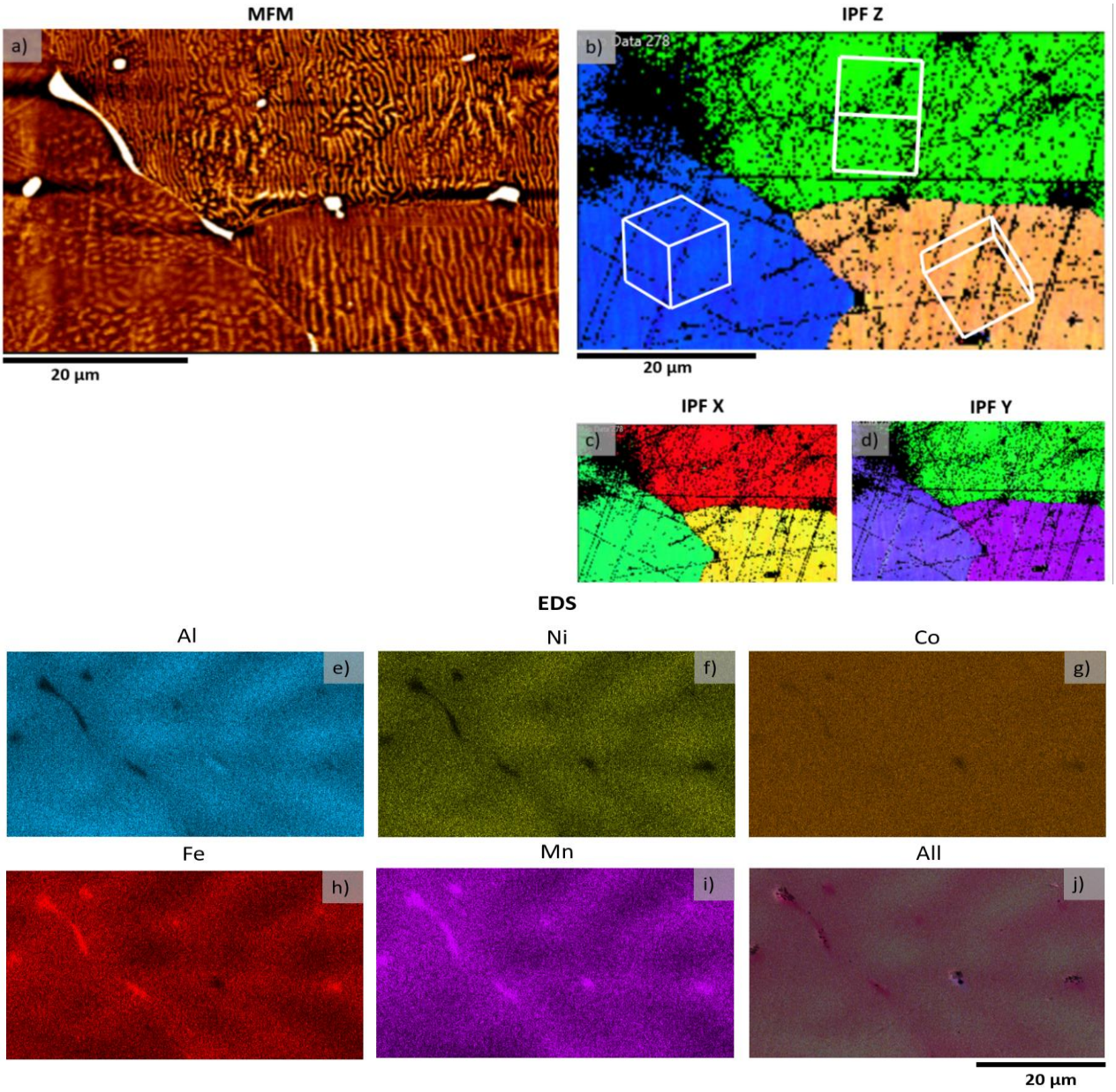

Fig. 5.13: a) MFM map **b)** IPF in z-direction from EBSD for same region as the MFM map, with illustrations of the crystal orientations **c)** IPF x-direction **d)** IPF y-direction. **e)-i)** are the elemental EDS maps for Al, Ni, Co, Fe and Mn, respectively, for the same region as MFM and EBSD above. **j)** is the combined EDS map with all colours together and SEM image in the background.

An experiment was performed in order to examine the magnetic domain pattern in MFM with respect to the crystallographic orientations of Alloy B. The same region was localized by use of the characteristic indention marks on the sample. The white spots in the MFM map are particles of the Mn-Fe phase, which was found to be weakly magnetic according to the contrast in the MFM result.

The EBSD map shows no match for the structure of the Mn-Fe particles, and they are visualized by the black areas in the IPFs, Fig. 5.13b-d. The EBSD map confirms that there are three grains with different orientations revealed by the MFM map. This explains the observed difference in the magnetic domain pattern (MDP) specific to each grain. With the IPF Z map in Fig. 5.13b as a basis, the grains will be referred to as green, blue and orange. The magnetic domain pattern in the green grain is oriented in the [110] direction. Here, the MDP is stripy, with some variation in the density of the stripes. Thus, there is a variation in the stripes period across the surface with splitting into more domains in some regions for this orientation.

The orange grain is not oriented along a major axis but does have a stripy MDP, just as the grain oriented in the [110] direction. The orange grain shows a more regular MDP but there is a tendency of having denser stripes closer to the grain boundaries. By investigating the EDS maps in Fig. 5.13e-j for the same region, a chemical trend is found. There is enhanced content of Fe and Mn and reduced content of Al and Mn at the grain boundaries. The blue grain in IPF Z shows a bubble-pattern. This type of MDP is evidence of the grain orientation being closely aligned to the easy magnetic axis in the crystal structure[37-39]. As the blue grain illustrated in Fig. 5.13b shows, the orientation is close to the body diagonal of the cube, the [111] direction. The easy axis is an important property of a magnetic material, as it defines the preferred magnetization direction of spontaneous magnetization, with respect to the crystal lattice[11]. By obtaining both the crystal structure and the easy axis of a material, one can evaluate the magnetocrystalline anisotropy. As high magnetic anisotropy generally means higher coercivity[40], it is important to obtain this knowledge in development of a soft magnetic material. This result should be verified by reproducibility and other methods.

For determining the easy axis, other methods, such as torque magnetometry and vector-VSM[41] could be used. However, the two methods also need material in a form of a single crystal, which is the main challenge to overcome for these techniques. If the grains are very small, it is difficult to make single-crystal samples. Therefore, the combination of MFM and EBSD is a good technique to identify an easy axis. An alternative is Lorentz microscopy, where both crystal orientation and the MPD of specific regions could be measured simultaneously. In any case, different MPDs in grains of different orientations provide evidence of magnetic anisotropy and existence of a preferred magnetization direction in the crystal.

5.3.3 Variation of domain patterns within the grains

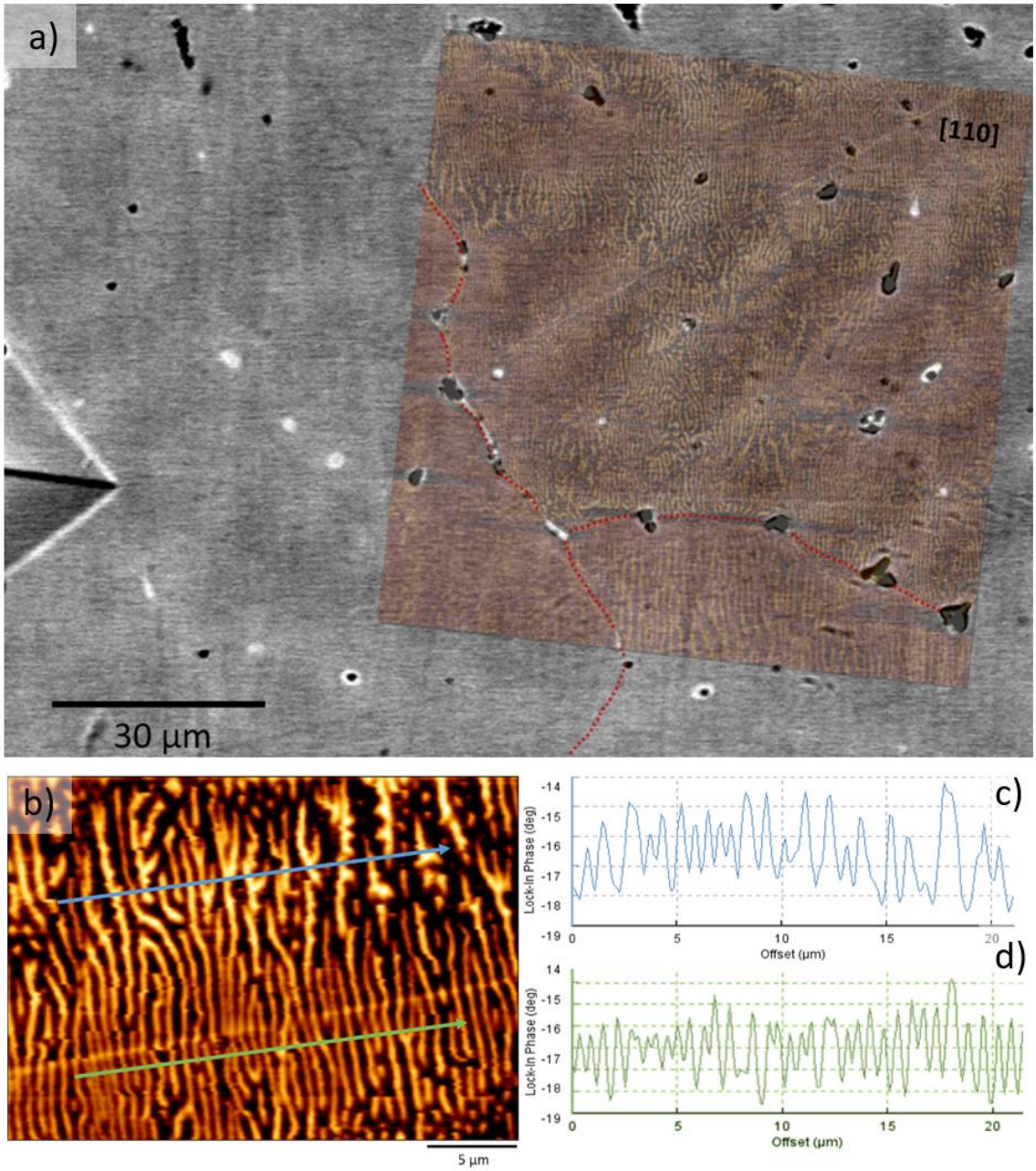

Fig. 5.14: a) BSE image from SEM overlaid with MFM map from the same region. The red line shows the grain boundary obtained from EBSD. **b)** Domain pattern within the [110] grain in a). **c)** Line profile of the domain pattern along the blue line in b). **d)** Line profile of the domain pattern along the green line in b).

As previously mentioned, there is a variation in the MDP within the grains. An attempt to correlate this variation in the domain pattern to the observed chemical variation was executed and presented in Fig a). If carefully comparing the MFM result with chemical content and the contrast from the SEM BSE image, there

is a tendency of denser stripes in the Fe-enhanced area (bright colour in SEM) and less dense stripes in the Al-enhanced area (dark colour). As there is a significant variation in elemental composition in these regions, it is not unexpected that the magnetic properties are different. However, the correlation is not perfect, and further investigation is needed to clarify the relationship between the MPD and the crystal coring.

The MFM map in Fig 5.14b shows the variation in domain stripes within the [110] oriented grain. The two cross section plots in Fig. 5.14c and d illustrate that there is an average domain wall distance of 0.58 μm and 0.91 μm for the blue and green line, respectively. The observation of domains splitting into denser stripes can be observed for high magnetic anisotropy[28], which raises the question of why there would be a difference in the magnetic anisotropy within the crystal. An answer to that can be strain, which is known to induce magnetocrystalline anisotropy[42]. It is reasonable to believe that there is strain in the crystal lattice due to the chemical variation of Al, and the variation seen in the EBSD results related to the core and outer regions of the dendrite. Strain in the crystal could be a possible explanation for the discussed variation in the domain patterns, however, more research is required to conclude.

To further investigate the crystal structure, a FIB sample was extracted along the EDS line scan shown in Fig 5.11a-b, crossing two arms of the dendrite. The lamella is normal to the [110] direction, confirmed by the EBSD map in Fig. 13a. The Fig. 5.15a-b below shows the region of interest before and after extraction of the sample. The TEM results for this FIB sample are presented in the next section.

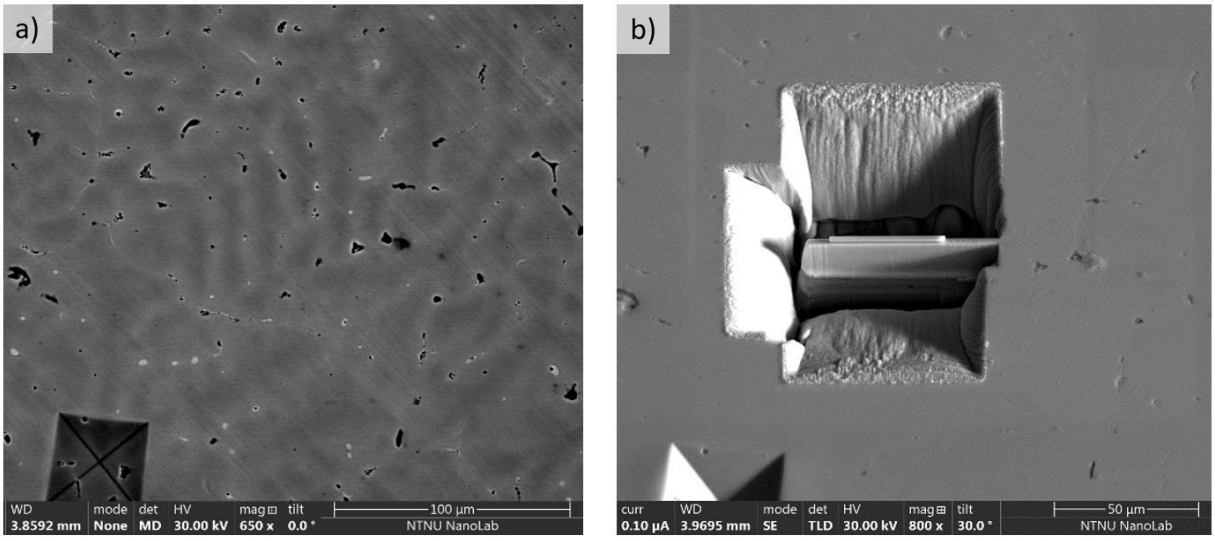

Fig 5.15: a) The area where the FIB was extracted shown in b) **b)** SEM image of the FIB lamella prepared for extraction.

5.3.4 The FIB sample on micrometre scale

In this section, the STEM results of the FIB sample on micrometre scale are presented.

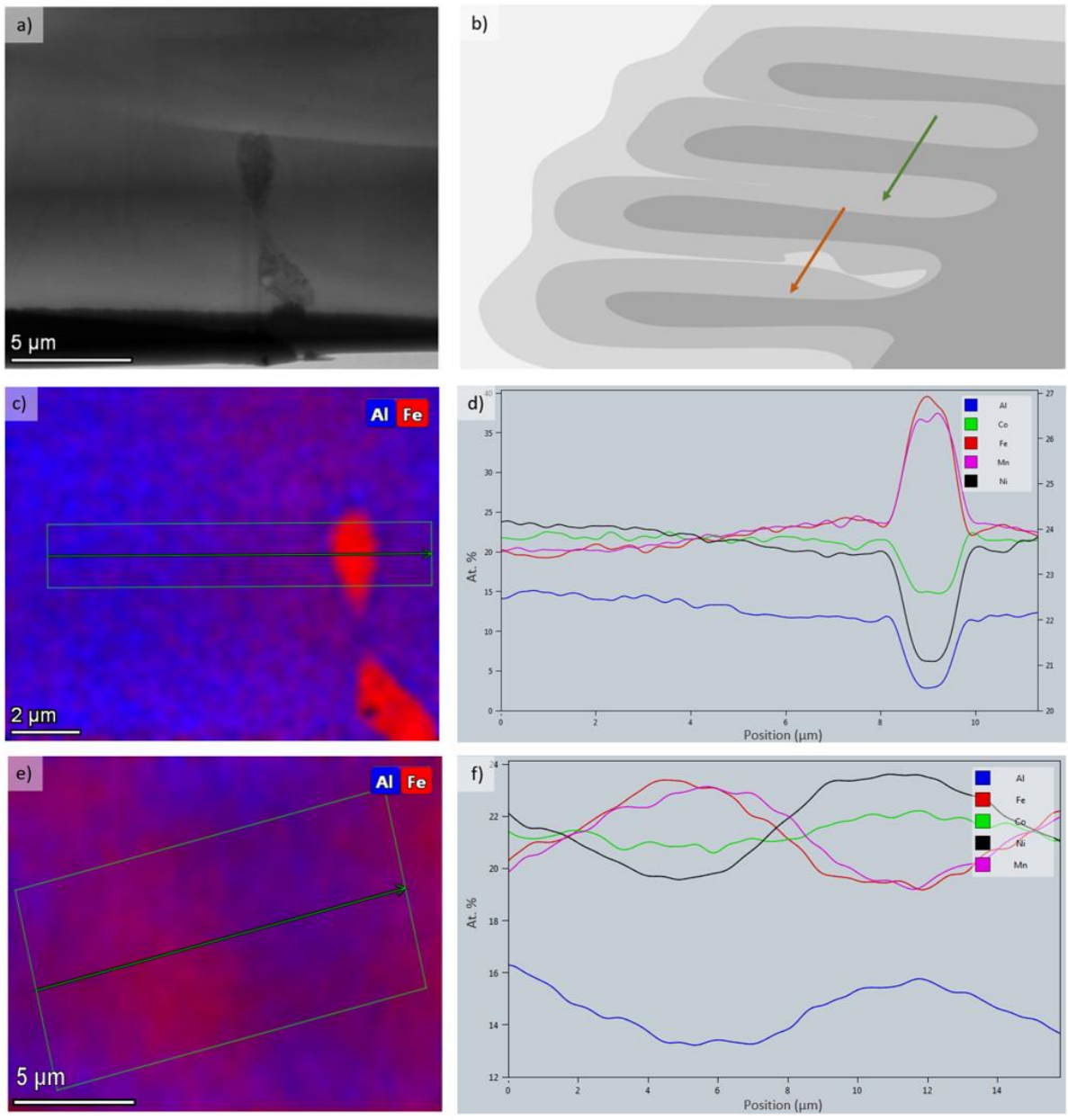

Fig. 5.16: a) A low-magnification ADF image of the FIB sample. **b)** A schematic illustration of the dendrite, with an orange arrow indicating the line scan in **c)**, which is crossing one dendrite arm and the profile of MnFe-phase along this line plotted in **d**. The green arrow in b) is the line of scan in **e)**, which is crossing one dendrite arm with its element profile plotted in **f)**. The STEM EDS maps in c) and e) are only mapped for the Al and Fe content.

The solidification process of the dendrite is illustrated in Fig. 5.16b. The darkest and the lightest grey tones represent the solidification at higher and lower temperature, respectively. The trapped MnFe-phase is

illustrated as the brighter region below the orange arrow in Fig. 5.16b. The illustration is a simplification and is provided to give an overview and understanding of the measured areas in terms of chemical analyses.

The EDS map in Fig 5.16c shows the compositional gradient of Al and Fe when moving from one dendrite arm to another and crossing the MnFe-phase. The plot in Fig. 5.16d reveals an increase in Mn and Fe concentration towards the MnFe-phase as the other constituents decrease. The MnFe-phase can be observed as the strongly red coloured dumbbell shape in Fig. 5.16c and is recognized by the same shape as in the ADF image in Fig. 5.16a. The MnFe-dumbbell is of importance for the Lorentz microscopy results discussed further down. The obtained content of this MnFe-phase from the TEM EDS is in accordance with the SEM EDS analysis.

The EDS map and line scan plot in Fig. 5.16e-f show the coring effect, as observed in the SEM, and the scan is crossing two dendrite arms that has grown together, without pure MnFe-phase in-between. This line measurement is illustrated by the green arrow in Fig. 5.16b. The map is shown for Fe and Al to amplify the compositional gradient by utilizing the two most anti-correlating constituents. Here, the same trend as in the SEM is observed for the elements. However, the aluminium content has dropped significantly in comparison to the SEM measurement, despite that the SEM line scan was obtained on the specific region where the FIB sample was extracted.

5.3.4.1 Diversity in the SEM and TEM elemental analyses

The chemical analyses in SEM and TEM is conducted perpendicular to each other, due to the FIB sample geometry, which is illustrated in Fig 5.17. When comparing the results for the core regions of the dendrite, the Al content drops from roughly 28 at. %, down to 16 at. %, from the SEM to the TEM measurement. When normalizing the two results on Fe content, the chemical composition is $FeNi_{1.31}Co_{1.19}Mn_{1.13}\mathbf{Al_{1.63}}$ for the SEM and $FeNi_{1.25}Co_{1.16}Mn_{1.01}\mathbf{Al_{0.85}}$ for the TEM measurement. In other words, Al content drops significantly more than content of other elements.

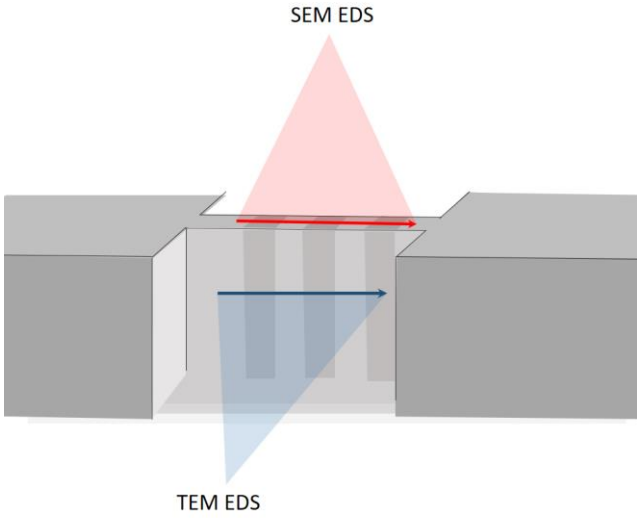

Fig. 5.17: An illustration of the FIB sample and the direction of the acquired compositional quantifications. The stripes illustrate the observed coring.

There are some possible ways to interpret the diversity in these results in order to evaluate whether this variation is real or an artefact. A possible explanation for the results, is that the EDS line scan was not performed on the exact same area where the FIB sample was extracted, or that the chemical composition is dependent on the direction of measurement. However, the measured region is within the same dendrite and not close to a grain boundary and both line scans are crossing dendrite arms. For this variation to be real, that means that the dendrite has solidified with a great variation in the core region. In addition, if the chemical variation is real, the FIB sample is deviating from the extensive EDS analysis acquired by two separate SEMs. The maximum content of Al in the FIB sample is then lower than the observed global minimum content for Al in the bulk sample. Given these considerations, it might seem unlikely that the observed results are due to a real variation in the chemical composition. This leads to a discussion of possible sources of error and differences between the SEM and TEM analysis.

Absorption of aluminium's characteristic x-rays in the sample is one possible explanation for the inconsistent results, and the closely related possibility of error in the EDS software's absorption-corrections. In an SEM, the EDS data are corrected for absorption of lighter elements, which in this composition is Al, if compared to the 3d transition metals. In TEM, the EDS analysis is to a very small degree corrected for absorption, or not corrected at all, due to small thickness of the sample. To test the differences in absorption correction for the software, the same raw data file was opened in the AZtec EDS-SEM and the AZtec EDS-TEM software. The test showed that the TEM software returned a lower value for Al with the SEM raw data as input, which substantiate the absorption-correction differences by the software. This test gave similar chemical values as observed experimentally and are available in Appendix A.

Additionally, absorption of aluminium's characteristic x-rays was observed through systematic measurements with point EDS on the mechanically prepared wedge sample in the TEM. The Al content dropped when moving into thicker regions away from the wedge edge, while maintaining the same phase, verified by the diffraction pattern. The explanation of this observation for the mechanically prepared samples was concluded to be absorption of Al characteristic x-rays due to increased sample thickness. Given these considerations, the experimental difference across the instruments may be related to absorption or absorption-correction procedure.

From the discussion above follows the question of which EDS could be considered correct. The FIB sample could be too thick to get correct estimates, or the absorption correction in the SEM could be too high. Alternatively, it could be a mixture of these effects, so that the true chemical composition is somewhere in-between. Regardless, the correlating and anti-correlating trend on micrometre-scale is the same in both instruments.

5.3.5 The FIB sample on nanometre-scale

In this section, the FIB sample is studied with higher magnification in the STEM. On the scale of micrometres, the sample appears as a dendrite that has crystallized in non-equilibrium, with larger compositional changes from core to outer regions of the crystal. On nanometre-scale, the STEM investigation reveals another level of uneven chemical distribution.

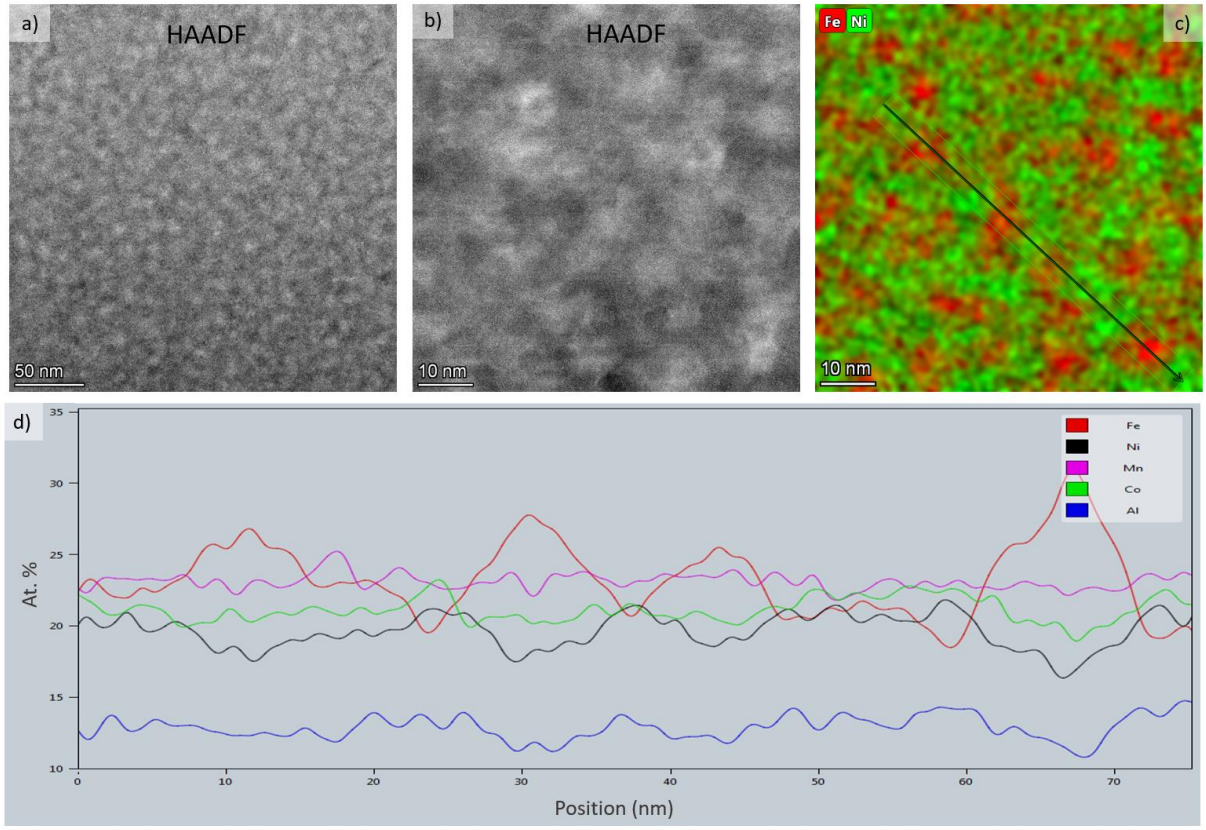

Fig. 5.18: a) HAADF image of the FIB sample. **b)** HAADF image of a smaller area corresponding to the EDS map in **c). d)** The EDS line scan plot indicated by the arrow in c).

The HAADF image in Fig 5.18a reveals a pattern of dark and bright spots with an approximate size of 5-15 nm. The contrast in the HAADF image could be a result of variation in the average atomic number or a thickness variation in the sample. The EDS analysis in Fig. 5.18c combined with the correlated HAADF image in Fig 5.18b substantiates the contrast as being related to the average atomic number. As Al has approximately half of the atomic number of other elements in the compound, its uneven distribution in the sample would mostly form the regions of lower average atomic number. Hence, leading to darker areas in the HAADF image. The general trend on nanoscale would be that Al is correlating with Ni and both anti-correlate with Fe. Hence, the bright regions in the HAADF image in Fig 5.18b are associated with the Fe-enhanced areas.

The chemical variation on nanoscale is observed in intervals of 5-15 nm and the FIB sample thickness is roughly 50-100 nm. This variation is assumed to be present through the sample. Thus, diffraction and EDS results are products of the composition along the transmitted electron beam. The results must be considered in this manner. HR-EDS was preformed along [110] as an attempt to identify chemical ordering in the unit cell, but due to both sample drift and this chemical variation, this method was not successful.

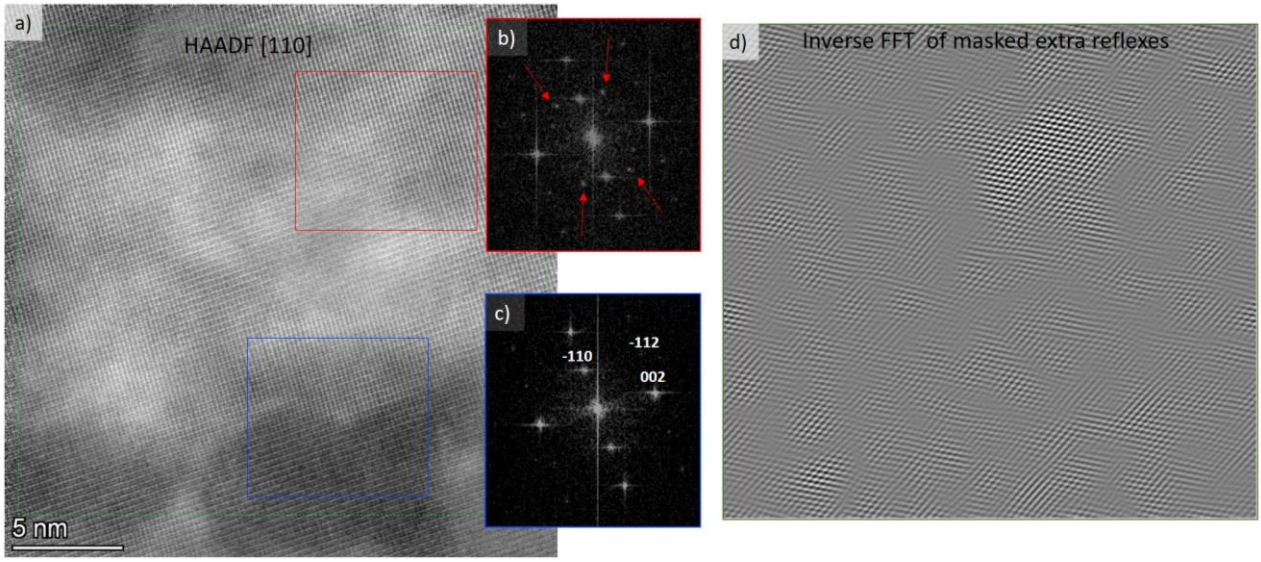

Fig. 5.19: a) HAADF image for [110] direction, with a selection of two regions where FFT is acquired, indicated by red and blue squares. **b)** FFT DP from the red square region and **c)** FFT DP from the blue square region, indexed as a B2 structure. **d)** An inverse FFT from the green square region in a), consisting of only the four masked reflections, indicated by the red arrows in b).

To investigate the observed contrast variation in the HAADF images in relation to the crystal structure, HR-STEM and FFT were performed for larger and smaller regions. The structure of the matrix was identified to fit the DP as a B2 phase. However, in some regions of the sample, additional reflexes to the B2 matrix were observed for the [110] direction. The HAADF image in Fig 5.19a is a region, where these local variations in the DP were present. The preformed FFTs in the red and blue square are shown in Fig. 5.19b and c), respectively. Some of the extra reflexes beyond the B2 phase, are indicated by the red arrows in the DP in Fig 5.19b. These additional reflexes are aligned to the B2 matrix and could be related to a superlattice with a higher degree of ordering in local regions. To study this possibility, the ratios between the reciprocal distances of the extra reflexes and the B2 matrix were calculated. The distance from the -110 to the -112 divided by the distance from -110 to the extra reflex in the direction of -112 equals to 0.42. The ratio of 0.42 is not an immediate indication of a superlattice reflex, and further work with DP from other projections would be required to clarify these local observations. The extra diffraction spots could also be related to another phase e.g., with preferred orientation to the matrix explaining the alignment to the matrix DP.

To systematically study the regions in the sample, in which the four extra reflexes were present, inverse FFT with applied masks on the given diffraction spots was performed. The result is presented in Fig. 5.19d, which reveals the regions in the sample, where the extra reflexes occur, shown as a "chess board pattern". The inverse FFT is acquired from the green square region in the HAADF image in Fig. 5.19a. The study did not identify a correlation between the brighter and darker regions in the HAADF image and the extra diffraction spots seen in the FFTs.

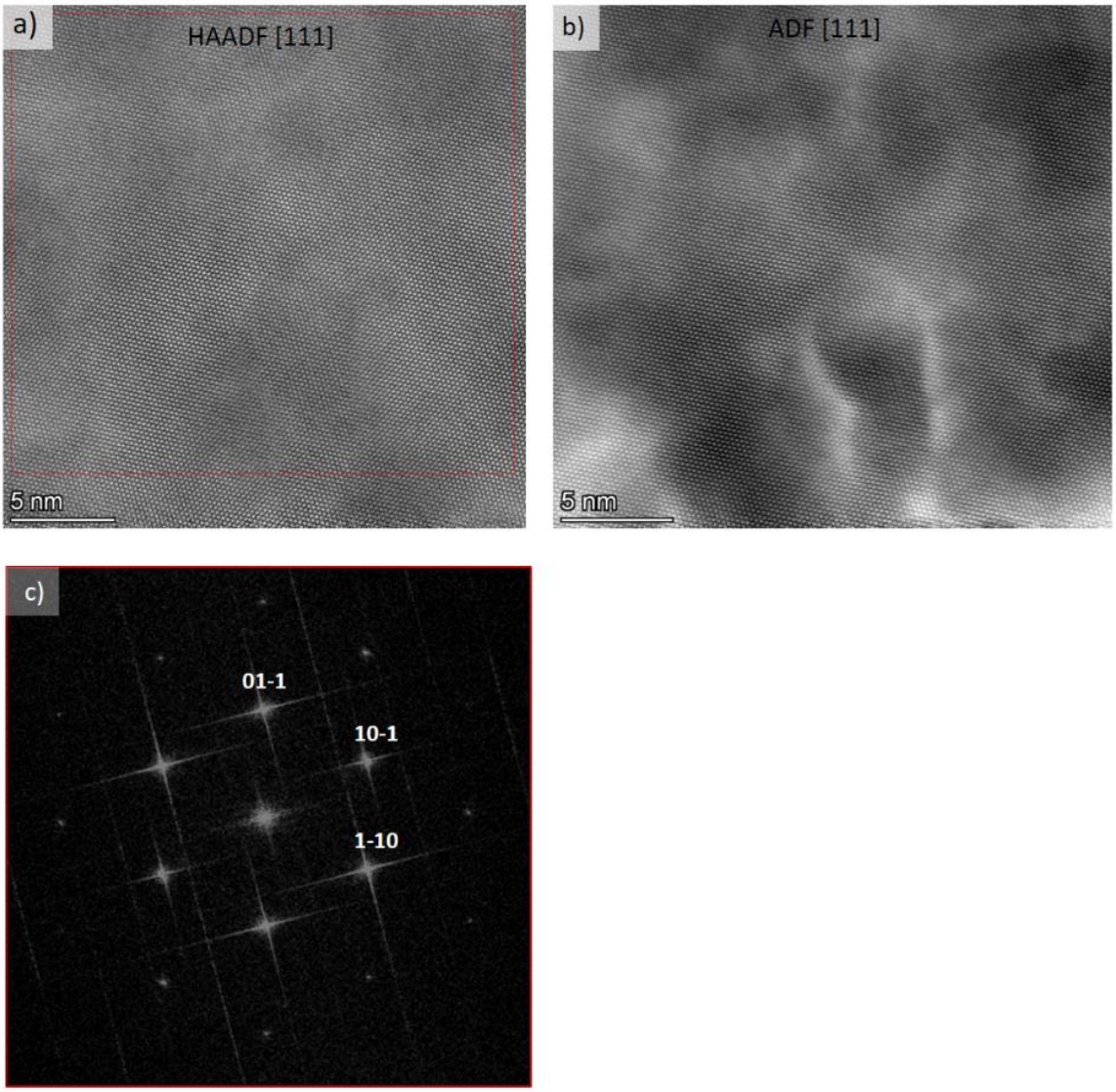

Fig. 5.20: a) HAADF image for [111] direction. **b)** ADF image for [111] direction. **c)** The DP obtained by FFT from the red square region in a).

The DP in Fig. 5.20c is obtained from FFT in the red square region in the HAADF image shown in Fig. 5.20a. It is indexed as a B2 structure for the [111] direction. No extra reflexes were observed with respect to the indexed phase. However, this is not the exact same area as the [110] direction shown above with extra

reflexes beyond the matrix. The reason was strong sample drift making it difficult to obtain the position under tilting.

Part of the initial objective was to search for evidence of a superlattice and local regions with higher degree of ordering. The reason of this was that it was observed by Bazioti et al.[4] in the Magnificent project for a similar alloy having increased content of Mn and Al. In relation to possible $L2_1$ structure type, the DP from the [111] orientation would look identical to a B2 type with half the lattice constant of the $L2_1$ structure. Given the above, limited amount of time was spent investigating this orientation in the sample.

The HAADF and ADF images in Fig. 5.20a and b) above are acquired from the same region of the sample. When comparing the contrast for specific regions, the brighter areas in ADF contrast may indicate strain in the lattice. This can be seen around the darker areas in the HAADF image, which are Al-enhanced regions. As mentioned in the EBSD part for this sample, Al has a larger metallic radius than the other constituents. This could result in strain in the crystal lattice if the distribution of this element is uneven. In relation to magnetism, strain in a material can change the magnetic properties and contribute to higher magnetocrystalline anisotropy[43, 44]. This effect is called magnetoelasticity, and e.g. for iron, the magnetocrystalline anisotropy becomes uniaxial under the strain[45]. This effect is not desired for a soft magnetic material and is an argument for annealing the material in order to remove strain. Further investigation of strain could be done by performing e.g., geometric phase analysis (GPA). Measuring the coercivity with VSM before and after annealing could give further insight.

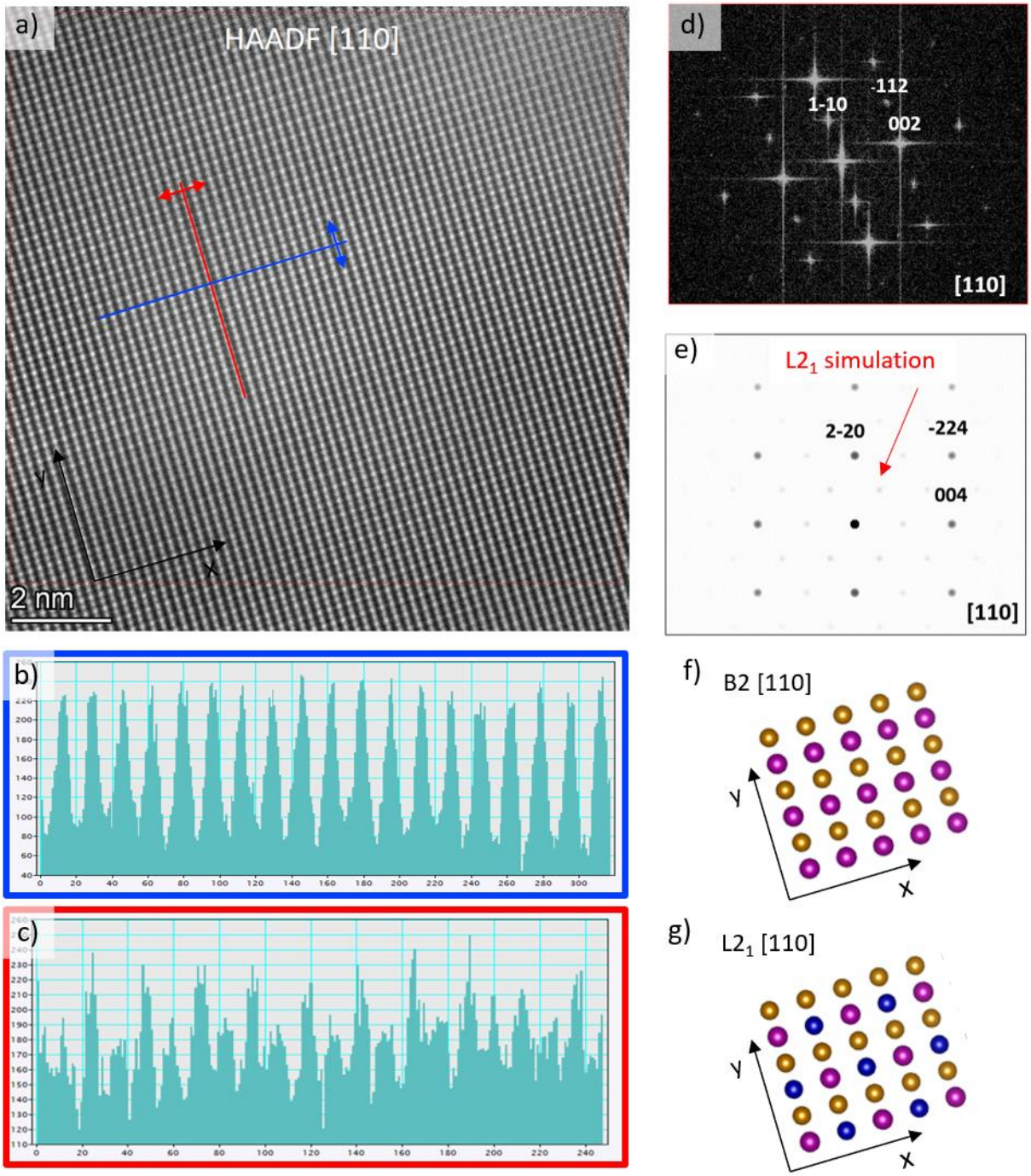

Fig. 5.21: a) HAADF HR-image for the [110] direction. **b)** A line profile of the intensities along the blue line in a). **c)** The line profile of the intensities along the red line in a). **d)** The DP obtain from FFT of a). **e)** A simulation of the DP for an $L2_1$ model for the [110] direction. **f-g)** Models of a B2 and $L2_1$ crystal lattice, respectively, in real space for the [110] direction.

FFT was performed on the HAADF image in Fig. 5.21a and is presented in Fig. 5.21d. The DP is indexed as a B2 phase, and no additional reflexes are visible. In comparison, the simulated DP in Fig. 5.21e shows how an $L2_1$ phase for the same orientation would look under ideal conditions, with the extra superlattice reflections occurring. The red arrow in the figure illustrates one of these reflexes. However, very weak reflections could be invisible in an FFT, which will be further elaborated below.

Local investigation of the intensities in real space was also performed for HAADF images in [110] direction. The aim was to identify the periodic trends in the intensities with a line profile, along certain directions. This method should be able to distinguish the $L2_1$ and B2 phases for the given orientation without having to perform FFT. This is beneficial because FFT can give low quality for smaller areas which, in turn, could make it hard to distinguish noise from weak reflexes. In addition, the magnitude of the intensities is easier to evaluate in a line profile than the spots in a DP. The [110] direction is preferred to separate the two symmetries that are related by degrees of ordering in the unit cell. The real space structural models for the two structure types are shown in Fig. 5.21f and g for the same orientation as the HAADF image in Fig 5.21a. The intensities obtained from the line profile are shown in Fig 5.21b and c) and are acquired along the atomic columns marked by the blue and red lines, respectively. When moving the blue line to the next atomic column along the positive and negative y-axis, the periodic trend in the intensities of the line profile was observed to stay constant.

The same was true for the red line when moving to the adjacent column in positive and negative x-direction. The intensity profile for the red line in Fig. 5.21c shows a trend of every other peak shifting up and down. The trend for intensity profile of the blue line is roughly constant in comparison. The line profiles are expected to differ for the B2 and $L2_1$ structure, where the latter type should result in alternation of the two profile types as in Fig.5.21b and c), when moving the blue line along the y axis. Since this trend was not observed, there is no evidence of the $L2_1$ phase being present in the measured area. The overall STEM study indicates that the sample is dominated by the B2 phase.

5.3.6 Lorentz microscopy of the FIB sample

5.3.6.1 Identifying domain walls

Lorentz microscopy was conducted on the FIB sample to study the domain walls. They are characterized by the lines of high contrast in Fig. 5.22b and c), which is not present in Fig. 5.22a, as well as inverse colour from the over-focused to under-focused image. The bright lines are of enhanced intensity due to adjacent domains with opposite, or close to opposite, alignment deflecting more electrons to the domain wall region. The black lines represent the reverse case, causing absence of intensity for the domain wall regions. The domain walls are highlighted in Fig. 5.24a as dotted lines, with the MnFe-phase marked in red. The width of the domains is approximately 2-5 micrometres, and the length is approximately 5-10 micrometres, confined by the edge of the sample. The identification of the domain walls was used to study the motion of the magnetic domains as a function of an increasing applied field from the objective lens, under constant

defocus. The magnetic field from the objective lens is perpendicular to the sample, and out of the plane with respect to Fig. 5.22, Fig. 5.23, and Fig. 5.24

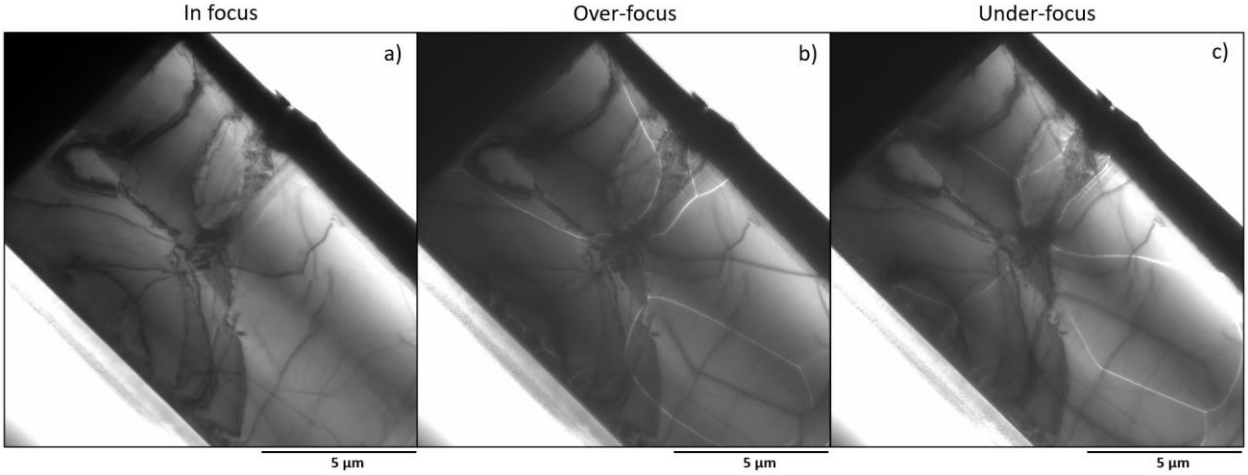

Fig. 5.22: The FIB sample observed in the lowest possible magnification in Fresnel mode: **a)** in focus, **b)** over-focus and **c)** under-focus with respect to the image plane.

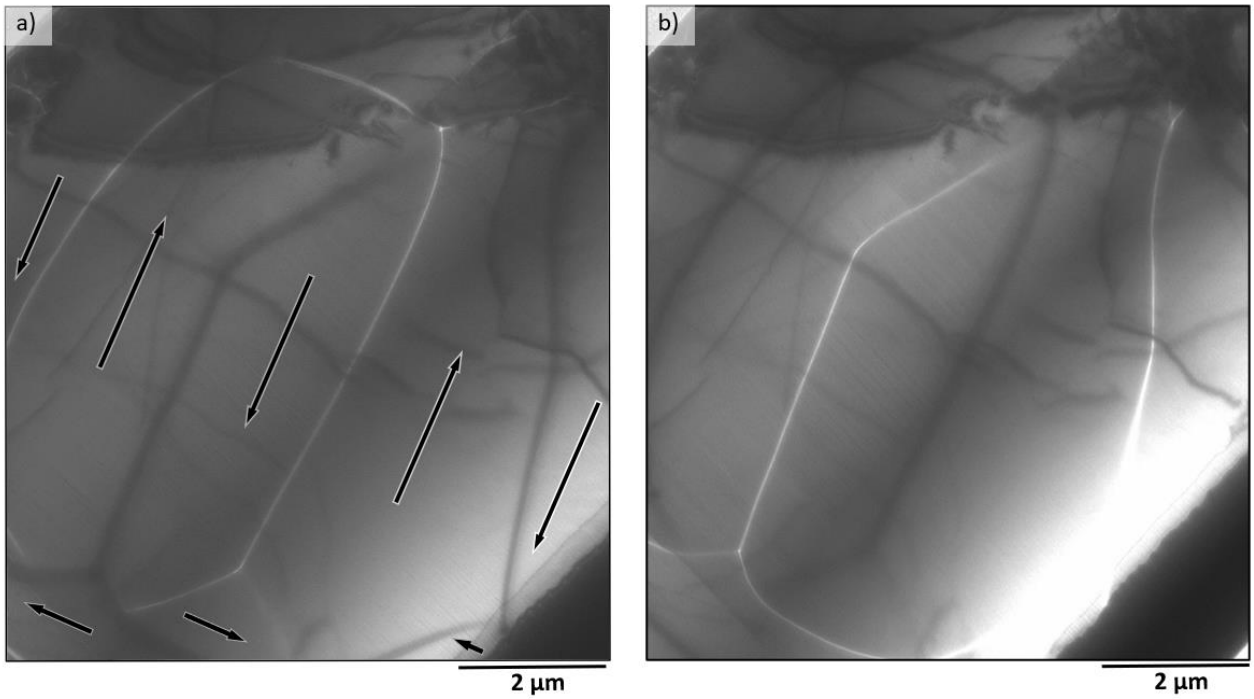

Fig. 5.23: a) Over-focus images with arrows suggesting direction of magnetization in the domains. **b)** Under-focus of same area as in a). Both figures are cropped and rotated being taken from the Fig. () b) and c).

Fig 5.23a presents a suggestion of how the direction of the magnetic moment in the domains is arranged. This arrangement of the domains will produce the same dark and white lines as experimentally observed in

the over-focus image. There is no meaning in the length of the arrows. The arrangement looks like so-called closure domains. A closure domain structure is an arrangement that minimizes the stray field (external field caused by a magnet or magnetostatic energy field). This domains arrangement acts to close a circuit of the magnetic flux lines and hence reduce the stray field. Landau and Lifshitz predicted this type of domain arrangement when minimizing the total energy of a magnet in 1935[46]. The same domain structure was further described and termed “domains of closure” in 1945 by Kittel[47]. The domains in this ordering are more or less parallel to the surface of the material, and observed near surfaces and for thin films, like this lamella sample[48, 49]. The presence of closure domains is an evidence that the specimen is trying to reduce its external field in the demagnetized state (no applied field). The 90-degree magnetization vectors required in a closure domain form at the expense of the magneto crystalline anisotropy, pointing magnetization away from the preferred easy axis in the crystal[50]. Hence, it emphasises the dominant role of reducing the magnetostatic energy for this sample.

5.3.6.2 Observation of domain wall motion in external field

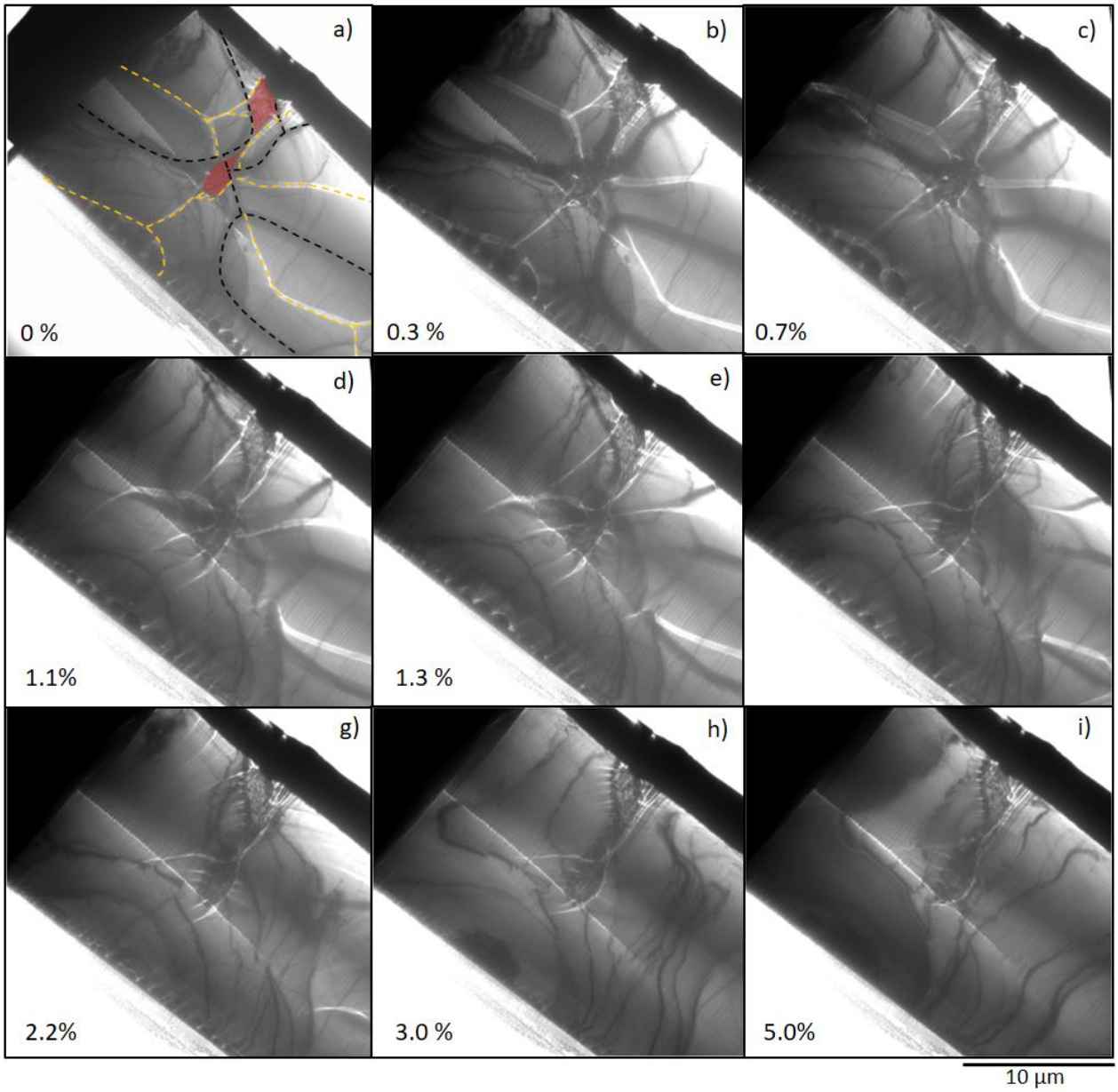

Fig. 5.24: a) The domain walls are identified and highlighted with dotted lines according to their contrast and the region for the MnFe-phase is marked in red. The strength of the objective lens is increased in ascending order for the images **b)-i)** with the percentage of the objective lens maximum noted in the left bottom corner.

In Fig. 5.24b and c), the magnetic field is increased from 0.3 % to 0.7% of maximum strength of the objective lens, and the movement of the walls can be observed. In Fig. 5.24d-g the field is increased from 1.1% to 2.2%. For this interval, some of the domain walls disappear, meaning that adjacent domains became aligned as a result of the stronger field from the lens, and the domain size increases. Minor changes in the domain wall movement are observed in Fig. 5.24h-i, which is the interval of 3.0% to 5.0% strength. This

indicates that the sample is close to saturation at 3% field strength, which corresponds to approximately 70 mT. The straight white line observed in Fig. 5.24i is a crack in the FIB sample. The domain walls move across this crack. However, no domain wall was observed crossing the MnFe phase, which is interpreted as this weak magnetic phase is pinning the domain walls. As a reference, the MnFe-phase is highlighted in Fig. 5.24a with red colour and can be traced to the last Fig. 5.24i.

Since this FIB sample was extracted from a single dendrite with the trapped MnFe phase and the motion of domain walls can be observed within one crystal lattice, MnFe phase can be treated as a large defect in the structure. Defects are known to pin domains and resist domain wall motion, which is important for hard magnetic materials[44, 51]. Hence, a more defect free and single-phase material is ideal to lower the coercivity. An adjustment in the nominal composition to lower values of Mn and Fe in addition to annealing is suggested to improve the desired magnetic properties.

5.4 Further work

A section is dedicated to further work based on the research in this thesis. As Alloy B has shown the best potential for applications as a soft magnetic material, further work is suggested with the focus on this composition. However, there are topics related to Alloy A that is not clear, as the precipitates in the FCC Fe-rich phase, but these are considered as less relevant for the aim of this thesis, due to the better magnetic properties of the Al-rich B2 phase.

5.4.1 Annealing

Annealing the alloys is highly recommended for further work. Systematic testing for different temperatures should be performed, followed by basic characterisation techniques in SEM, VSM and XRD. The observed coring effect should be studied in the SEM as a function of annealing temperature and measuring the average magnetic properties from VSM. Finally, pulverization of these samples can be conducted to study possible phase transitions by XRD. Here, the full width half maximum can be measured for the intensities in the diffractogram, to evaluate changes related to strain in the crystal lattice, presuming no phase transition has occurred.

5.4.2 Adjusting the nominal composition of Alloy B

The nominal composition of Alloy B should be adjusted to minimize the MnFe-phase which was observed at grain boundaries. The mass fraction can be obtained experimentally and removed from the nominal composition. First principal calculations are suggested to be performed to evaluate the most stable

composition for the B2 phase, where the coring was observed. The calculation should be based on the compositions obtain from experimental data from core to outer dendrite.

5.4.3 Validation of the easy axis

The evidence of an easy axis along the [111] direction needs to be verified by reproducibility of experiments. EBSD should be carried out in advance to locate well oriented grains with respect to the [111] direction and the surface of the sample. Further work with regards to this topic should include studying a possible shift in the easy axis for the annealed sample. This could indicate if the possible easy axis is induced by strain, as is known for Iron under strain conditions.

Chapter 6

Conclusion

This thesis is research establishing correlations between magnetic, structural, and compositional properties of a high-entropy alloy FeNiCoMnxAlx. In the research, several cutting-edge scientific instruments have been used. Two additive manufactured alloys with nominal compositions of FeNiCoMn0.29Al0.29 and FeNiCoMn0.9Al0.9 have been studied, named Alloy A and B, respectively. Both alloys had intrinsic coercivity below 600 A/m and were identified as soft magnetic materials. Alloy B was found to have better soft magnetic properties than A, with a saturation magnetization of 112 Am2/kg, and a coercivity of 280 A/m.

Alloy A

The nominal composition of Alloy A showed a mixture of two phases identified as an FCC and a B2 phase by SAED in TEM. The FCC phase was found to have an enhanced amount of Fe, whereas the B2 phase was rich in Al. The result is in agreement with findings in the literature, showing that increased content of Al is associated with more ordered crystal structure for this HEA system. The Al-rich phase in Alloy A was found to have better magnetic properties than the Fe rich phase, which was obtained by correlating MFM and EDS results of a specific region. As demonstrated, combining the two techniques is a good way to assign magnetic phases to chemical phases in a multi-phase alloy.

Alloy B

The study of Alloy B revealed presence of a B2 phase by XRD and STEM investigation, similar to the Al-rich phase in Alloy A. Microstructure analysis of Alloy B revealed a dendritic structure with the dendrites showing a compositional variation from core to outer regions. The chemical variation was explained by a solidification effect, taking place under non-equilibrium conditions. Correlation and anti-correlation elemental trends were observed through EDS analyses in the dendrites. EDS line scans showed that Ni and

Al content correlated with each other and there was anti-correlation between Mn and Fe content. A minor MnFe-phase was observed systematically at grain boundaries and it was found to be weakly magnetic by the MFM.

Magnetocrystalline anisotropy of Alloy B was studied through correlation of MFM and EBSD experiments for the same region. The results give evidence of an easy axis along the [111] direction in the magnet expressed in the presence of bubble domains for this crystallographic orientation. The results also revealed variation of domain pattern within the crystal grains, splitting into more domains in some regions. This was found to be a result of the chemical variation from the coring effect. Possible explanations of such an effect could be strain and induced magnetic anisotropy, or a bent lattice, as indicated by the EBSD result. However, further work is needed to clarify the reason of this variation.

STEM investigation of Alloy B revealed another level of compositional variation at nanometre-scale. The key observation was Ni and Al correlation with each other and anti-correlation with Fe, as was also observed on the micrometre-scale. The Al content obtained from EDS analysis in STEM was inconsistent with that obtained in SEM. This might be related to absorption of aluminium's characteristic x-rays in the sample, due to, e.g., thickness of FIB sample or absorption corrections from the SEM EDS software. Further work is needed to verify these possibilities.

Structural analysis such as FFT and line profiles was utilized to study HR HAADF images in relation to the chemical variation within the crystal grains. The crystal was identified as a B2 structure by XRD, with no signs of the more ordered L21 phase, as reported in an alloy with higher Mn and Al content from the Magnificent project.

Lorenz microscopy was conducted to study the magnetic domains. Observation of closure domains confirms the ferromagnetic nature of Alloy B in the demagnetized state, in which domains order themselves to reduce the stray field. Domain wall motion was observed as a function of increased field from the objective lens, revealing pinning of domain walls by the MnFe-rich phase, acting as large defects in the alloy. The results point out a potential for further development of this soft magnetic material for industrial applications.

Suggested future work to improve magnetic properties is adjusting the nominal composition combined with a post heat treatment to approach a single-phase and a more defect-free alloy.

Bibliography

1. Li, P., A. Wang, and C.T. Liu, *A ductile high entropy alloy with attractive magnetic properties.* Journal of Alloys and Compounds, 2017. **694**: p. 55-60.
2. Li, Z., et al., *Tuning phase constitution and magnetic properties by composition in FeCoNiAlMn high-entropy alloys.* Journal of Alloys and Compounds, 2020. **845**: p. 156204.
3. Li, P., A. Wang, and C.T. Liu, *Composition dependence of structure, physical and mechanical properties of FeCoNi(MnAl)x high entropy alloys.* Intermetallics, 2017. **87**: p. 21-26.
4. Bazioti, C., et al., *Probing the structural evolution and its impact on magnetic properties of FeCoNi(AlMn)x high-entropy alloy at the nanoscale. Unpublished work.*
5. Cantor, B., et al., *Microstructural development in equiatomic multicomponent alloys.* Materials Science and Engineering: A, 2004. **375-377**: p. 213-218.
6. Tsai, M.-H. and J.-W. Yeh, *High-Entropy Alloys: A Critical Review*. Materials Research Letters, 2014. **2**(3): p. 107-123.
7. JEOL. *Annular bright-field scanning transmission electron microscopy, https://www.jeol.co.jp/en/words/emterms/search_result.html?keyword=ABF-STEM. 11. Aug. 2021*.
8. Cordova, G., B.Y. Lee, and Z. Leonenko, *Magnetic Force Microscopy for Nanoparticle Characterization.* NanoWorld Journal, 2016. **2**(1): p. 10-14.
9. Passeri, D., et al., *Magnetic force microscopy.* Biomatter, 2014. **4**(1): p. e29507.
10. Hopster, H. and H.P. Oepen, *Magnetic Microscopy of Nanostructures*, in *Magnetic Microscopy of Nanostructures*. 2005, Springer, Berlin, Heidelberg. p. 254-260.
11. Gruszecki, P., et al., *The influence of the internal domain wall structure on spin wave band structure in periodic magnetic stripe domain patterns*, in *Solid State Physics*, R.L. Stamps and H. Schultheiß, Editors. 2019, Academic Press. p. 79-132.
12. Cullity, B.D. and C.D. Graham, *Magnetic Anisotropy*, in *Introduction to Magnetic Materials*. 2008. p. 197-239.
13. Sechovský, V., *Magnetism in Solids: General Introduction*, in *Encyclopedia of Materials: Science and Technology*, K.H.J. Buschow, et al., Editors. 2001, Elsevier: Oxford. p. 5018-5032.
14. Reeve, R., et al., *Magnetic Imaging and Microscopy*. 2018.
15. Yeh, J.-W., et al., *Nanostructured High-Entropy Alloys with Multiple Principal Elements: Novel Alloy Design Concepts and Outcomes.* 2004. **6**(5): p. 299-303.
16. Yeh, J.-W., *Alloy Design Strategies and Future Trends in High-Entropy Alloys.* JOM, 2013. **65**(12): p. 1759-1771.
17. Liaw, P., J.-W. Yeh, and Y. Zhang, *High-entropy alloys: Fundamentals and applications*. 2016. 20-50.
18. Watson, R.E. and L.H. Bennett, *Hume-Rothery Parameters and Phases*, in *Encyclopedia of Materials: Science and Technology*, K.H.J. Buschow, et al., Editors. 2001, Elsevier: Oxford. p. 3843-3849.
19. Guo, S., et al., *Effect of valence electron concentration on stability of fcc or bcc phase in high entropy alloys.* 2011. **109**(10): p. 103505.

20. Yang, S., et al., *Revisit the VEC rule in high entropy alloys (HEAs) with high-throughput CALPHAD approach and its applications for material design-A case study with Al–Co–Cr–Fe–Ni system.* Acta Materialia, 2020. **192**: p. 11-19.
21. Chen, R., et al., *Composition design of high entropy alloys using the valence electron concentration to balance strength and ductility.* Acta Materialia, 2018. **144**: p. 129-137.
22. Ogura, M., et al., *Structure of the high-entropy alloy AlxCrFeCoNi: fcc versus bcc.* Journal of Alloys and Compounds, 2017. **715**: p. 454-459.
23. Stepanov, N., et al., *Effect of Al on structure and mechanical properties of Fe-Mn-Cr-Ni-Al non-equiatomic high entropy alloys with high Fe content.* Journal of Alloys and Compounds, 2019. **770C**: p. 194-203.
24. Wang, F.J., Y. Zhang, and G.L. Chen, *Atomic packing efficiency and phase transition in a high entropy alloy.* Journal of Alloys and Compounds, 2009. **478**(1): p. 321-324.
25. Lee, C.-F. and T.-T. Shun, *Effect of Fe content on microstructure and mechanical properties of Al0·5CoCrFexNiTi0.5 high-entropy alloys.* Materials Characterization, 2016. **114**: p. 179-184.
26. Huang, S., et al., *Mechanism of magnetic transition in FeCrCoNi-based high entropy alloys.* Materials & Design, 2016. **103**: p. 71-74.
27. Cullity, B.D. and C.D. Graham, *Soft Magnetic Materials*, in *Introduction to Magnetic Materials*. 2008. p. 439-476.
28. Getzlaff, M., *Fundamentals of Magnetism*, in *Fundamentals of Magnetism*. 2008, Springer, Berlin, Heidelberg. p. 117-131.
29. Halilov, S.V., et al., *Magnetocrystalline anisotropy energy in cubic Fe, Co, and Ni: Applicability of local-spin-density theory reexamined.* Physical Review B, 1998. **57**(16): p. 9557-9560.
30. Zhang, B., et al., *Rapid Annealing Optimizing Magnetic Softness and Thermal Stability of Mn-Substituted Fe-Based Nanocrystalline Alloys.* 2021. **11**(1): p. 20.
31. Mishra, R.K. and R.R. Shahi, *Novel Co35Cr5Fe20Ni20Ti20 high entropy alloy for high magnetization and low coercivity.* Journal of Magnetism and Magnetic Materials, 2019. **484**: p. 83-87.
32. *How to create an inverse pole figure color map? https://mathematica.stackexchange.com/questions/47492/how-to-create-an-inverse-pole-figure-color-map. 11. Aug. 2021*. 2019.
33. Solberg, J.K. and V. Hansen, *Innføring i transmisjon elektronmikroskopi.* 2007.
34. Fultz, B. and J. Howe, *Appendix*, in *Transmission Electron Microscopy and Diffractometry of Materials*. 2013, Springer. p. 681-761.
35. Campaña, A.L., et al. *Probing Van Der Waals and Magnetic Forces in Bacteria with Magnetic Nanoparticles*. in *2020 IEEE 10th International Conference Nanomaterials: Applications & Properties (NAP)*. 2020.
36. Yang, C., et al., *Soft-Magnetic High-Entropy AlCoFeMnNi Alloys with Dual-Phase Microstructures Induced by Annealing.* Acta Metallurgica Sinica (English Letters), 2020. **33**(8): p. 1124-1134.
37. Wulferding, D., et al., *Domain engineering of the metastable domains in the 4f-uniaxial-ferromagnet CeRu2Ga2B.* Scientific Reports, 2017. **7**.
38. Ermolaeva, O.L., et al., *Magnetic Force Microscopy of Nanostructured Co/Pt Multilayer Films with Perpendicular Magnetization.* Materials (Basel, Switzerland), 2017. **10**(9): p. 1034.
39. Bozorth, R.M., *Magnetic domain patterns.* Le journal de physique et le radium, 1951. **12**(3): p. 308-321.
40. Azuma, D., *Magnetic materials*, in *Wide Bandgap Power Semiconductor Packaging*, K. Suganuma, Editor. 2018, Woodhead Publishing. p. 97-107.
41. Dodrill, B., J. Lindemuth, and J. Krause. *Magnetic Anisotropy: Measurements with a Vector Vibrating Sample Magnetometer*. 2004.
42. Ciubotariu, O., et al., *Strain-induced perpendicular magnetic anisotropy and Gilbert damping of Tm3Fe5O12 thin films.* Scientific Reports, 2019. **9**(1): p. 17474.

43. Kotnala, R.K. and J. Shah, *Ferrite Materials: Nano to Spintronics Regime*, in *Handbook of Magnetic Materials*, K.H.J. Buschow, Editor. 2015, Elsevier. p. 291-379.
44. Smallman, R.E. and R.J. Bishop, *The physical properties of materials*, in *Modern Physical Metallurgy and Materials Engineering (Sixth Edition)*, R.E. Smallman and R.J. Bishop, Editors. 1999, Butterworth-Heinemann: Oxford. p. 168-196.
45. Kittel, C., *Theory of the Structure of Ferromagnetic Domains in Films and Small Particles.* Physical Review, 1946. **70**(11-12): p. 965-971.
46. Landau, L. and E. Lifshitz, *On the theory of the dispersion of magnetic permeability in ferromagnetic bodies* in *Perspectives in Theoretical Physics, Reprinted from Physikalische Zeitschrift der Sowjetunion 8, Part 2, 153-169, 1935*, L.P. Pitaevski, Editor. 1992, Pergamon: Amsterdam. p. 51-65.
47. Kittel, C., *Physical Theory of Ferromagnetic Domains.* Reviews of Modern Physics, 1949. **21**(4): p. 541-583.
48. Hubert, A. and W. Rave, *How well-defined are closure domains?* Journal of Magnetism and Magnetic Materials, 1999. **196-197**: p. 325-326.
49. Ohring, M., *14 - Magnetic Properties of Materials*, in *Engineering Materials Science*, M. Ohring, Editor. 1995, Academic Press: San Diego. p. 711-746.
50. Bube, R.H., *Magnetic Properties*, in *Electrons in Solids (Third Edition)*, R.H. Bube, Editor. 1992, Academic Press: San Diego. p. 242-265.
51. Jeudy, V., et al., *Pinning of domain walls in thin ferromagnetic films.* Physical Review B, 2018. **98**(5): p. 054406.
52. Webster, P.J. *The magnetic and chemical structures of the Heusler alloys*. 1968.

Appendix A

EDS raw file opened in TEM and SEM software

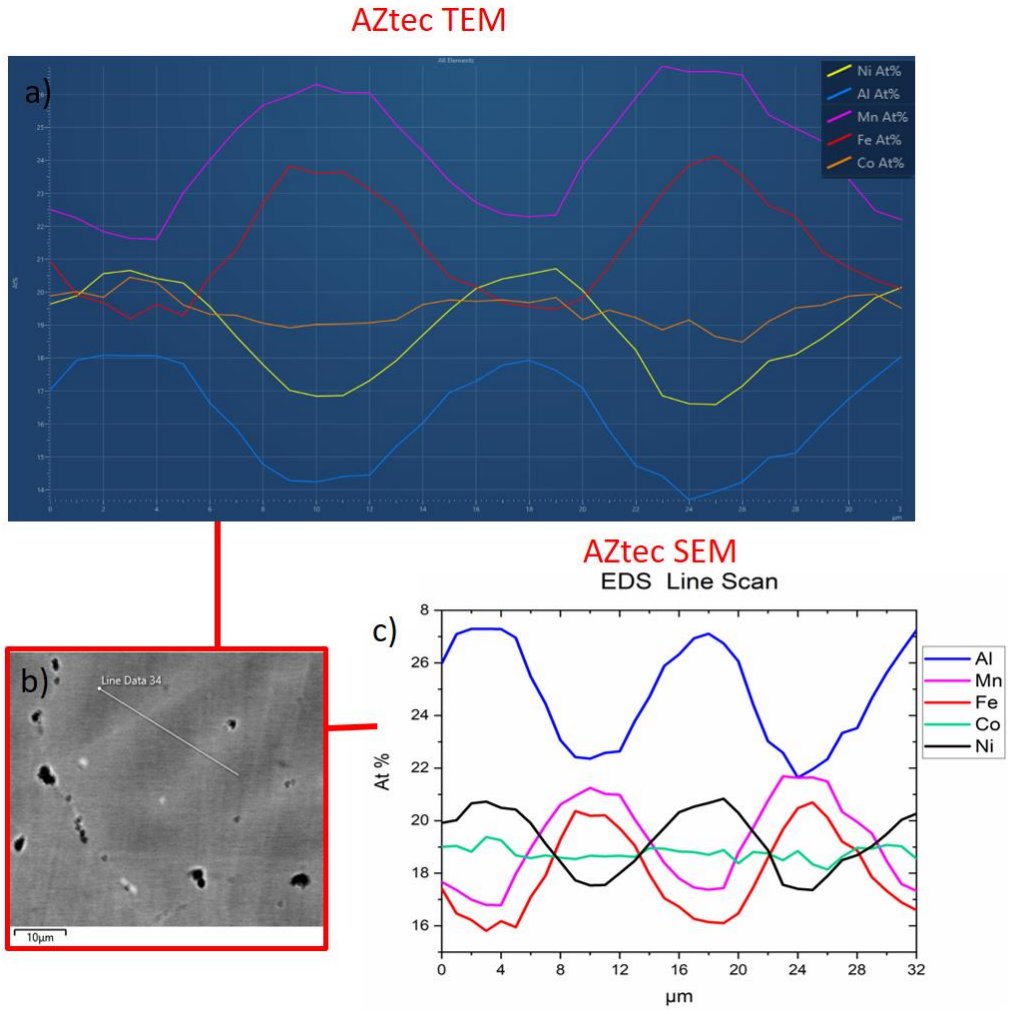

Fig. A.1: The exact same data set/raw file, opened in **a)** AZtec TEM and **c)** AZtec SEM plotted as atomic percent. **b)** Shows the region for the scan. The plot in c) is plotted with Origin, but the data are identical as when opened in AZtec SEM.

Fig. A.1 shows that the AZtec TEM and SEM software evaluate the same data set differently and that the content of Al has the most significantly drop in atomic percent. Thus, this correction for absorption between bulk and TEM sample may contribute to the experimentally observed drop in Al content across the instrument.

XRD results and simulation

The aim of this method was to propose two models of different crystal structures, namely a B2 and $L2_1$ phase that closely matched the experimental XRD pattern and EDS maps. The structure factors were calculated for both crystal structures in order to evaluate the similarities and differences between them.

The average composition used to build the models is given by Table A.1 below. To include all five constituents in these structures, partially occupancies on atomic positions must be taken into account, as there are more constituents than unique positions in the unit cell. The atomic scattering factors in the structure factor expression was indexed with Wycoff sites in order to represent all atoms occupying these positions.

Table A.1: The elemental composition used for the B2 and $L2_1$ models

	Fe	**Ni**	**Co**	**Mn**	**Al**
Formula	1	1,3	1,2	1,1	1,6
at %	16	21	19	18	26

The structure factor for B2:

$$F_{hkl} = \begin{cases} f_{1a} + f_{1b} & \text{for } h+k+l = \text{even} \\ f_{1a} - f_{1b} & \text{for } h+k+l = \text{odd} \end{cases} \quad \text{(A.1)}$$

The structure factor for $L2_1$:

$$F_{hkl} = \begin{cases} 4f_{4a} + 4f_{4b} + 8f_{8c} & \text{for } h+k+l = 4n \\ 4f_{4a} + 4f_{4b} - 8f_{8c} & \text{for } h+k+l = 4n+2 \\ 4f_{4a} - 4f_{4b} & \text{for } h+k+l = \text{odd} \\ 0 & \text{for mixed parity of } hkl \end{cases} \quad \text{(A.2)}$$

The $L2_1$ structure has some allowed reflections that are not possible for the B2 structure, i.e., the reflections from all odd h+k+l in the $L2_1$ type, which are given in Eq. A.2. However, these intensities of reflections

could be very close to zero for this alloy. The condition for this to be satisfied is when 4a and 4b sites in the $L2_1$ structure have the same number of electrons. Since most of the elements in the sample are 3d metals and differ by only one or two atomic numbers, any ordering between them could be difficult to distinguish. Hence, if Al is ordered at the 8c position for the $L2_1$ structure, and the 4a and 4b sites are not fully disordered being filled with the 3d transition metals, the $L2_1$ and B2 would be difficult to distinguish with XRD. The simulated XRD patterns in Fig. A.2a and b) illustrate this issue. The data for the B2 and $L2_1$ models can be found in Table A.2 and Table A.3, respectively.

The B2 model

For the B2 model, Al is ordered at 1a site, and all the other elements are randomly disordered in correspondence with the compositional data from table A.2. It would be equivalent to order Al at the 1b site.

B2 - Space group #221, Pm-3m

Table A.2: The B2 model

Wycoff site	Position	Atom (Occupancy)
1a	(0,0,0)	Fe (0.10), Ni (0.14), Co (0.12), Mn (0.12), Al (0.52)
1b	(½, ½, ½)	Fe (0.22), Ni (0.28), Co (0.26), Mn (0.24)

The $L2_1$ models

These models were based on ordering Al at the 8c position and then distributing the 3d transition metals at 4a and 4b according to the EDS data, without disordering the two sites. There are many possible ways to order the rest of the transition metals without reducing the symmetry to that of a B2 type. Here, one possible way is proposed.

$L2_1$- Space group #225, Fm-3m

Table A.3: The $L2_1$ model

Wycoff site	Position	Atom (Occupancy)
4a	(0,0,0)	Co (0.76), Mn (0.24)
4b	(½, 0, 0)	Fe (0.64), Ni (0.36)
8c	(¼, ¼,¼)	Al (0.52), Mn (0.24), Ni (0.24)

The procedure to obtain the B2 and $L2_1$ structure factors can be found in Appendix B.

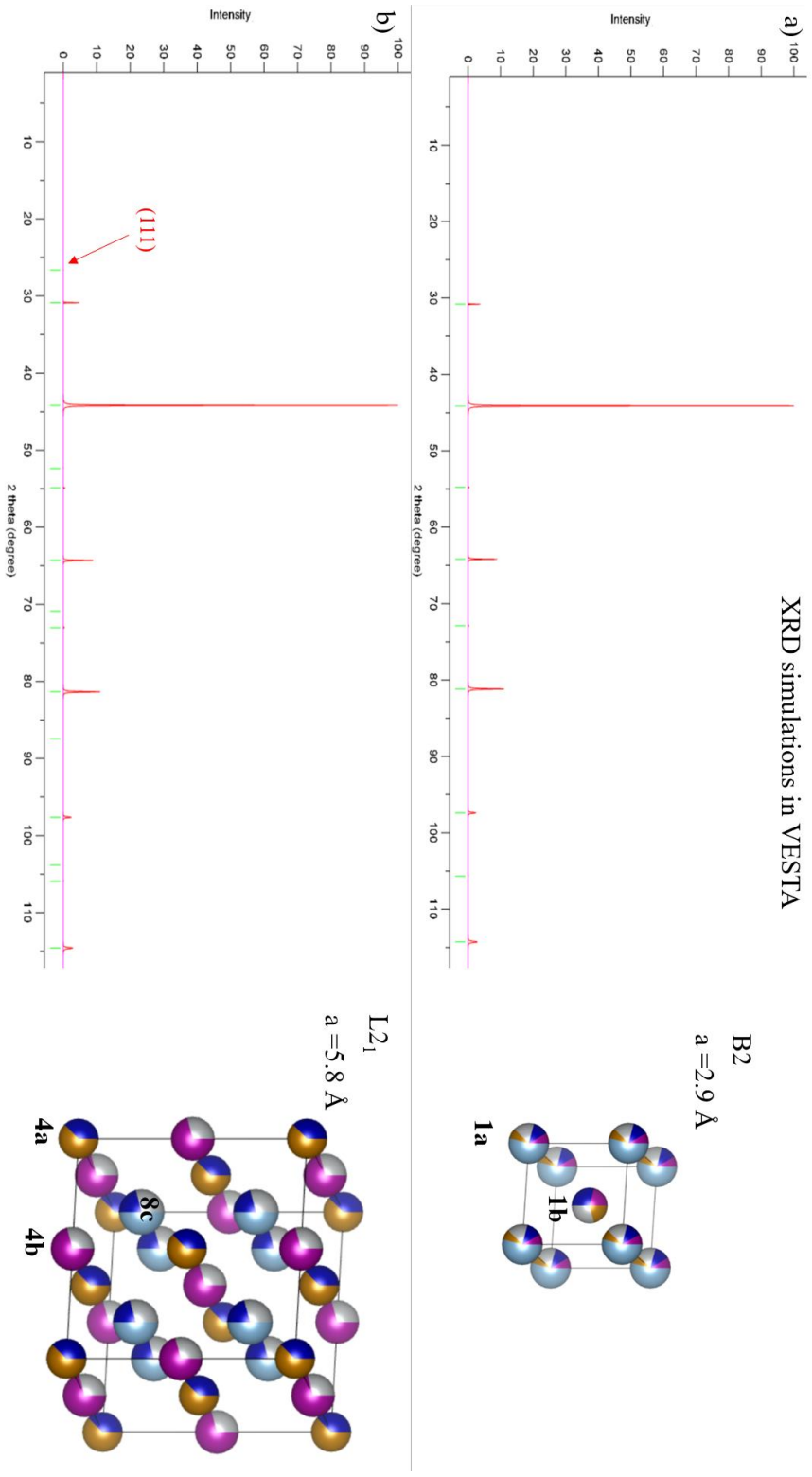

Fig. A.2: XRD simulations of **a)** B2 and **b)** $L2_1$ models. The red arrow in the $L2_1$ diffractogram highlights the low intensity of the [111] reflection that is possible to observe for a B2 type structure.

The evaluation of the structure factors and simulations, were further used to conduct XRD experiments with a very small step length in the intervals where these additional superlattice intensities could be present. An example of this is shown in Fig A.3 below, which does not indicate any presence of an $L2_1$ phase in the alloy.

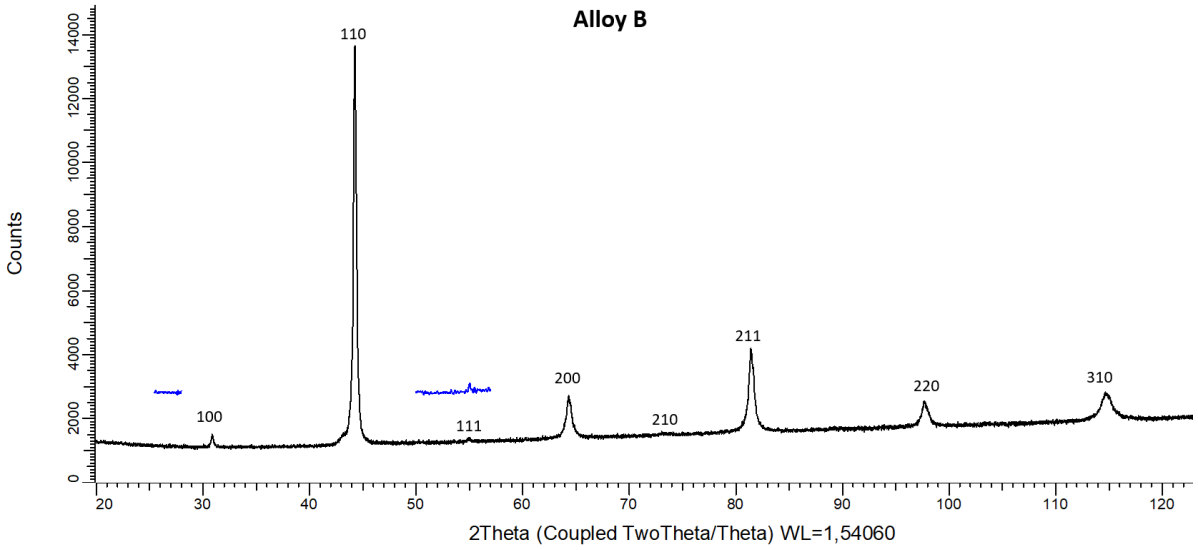

Fig. A.3: An experimental powder XRD result of Alloy B indexed for a B2 phase.

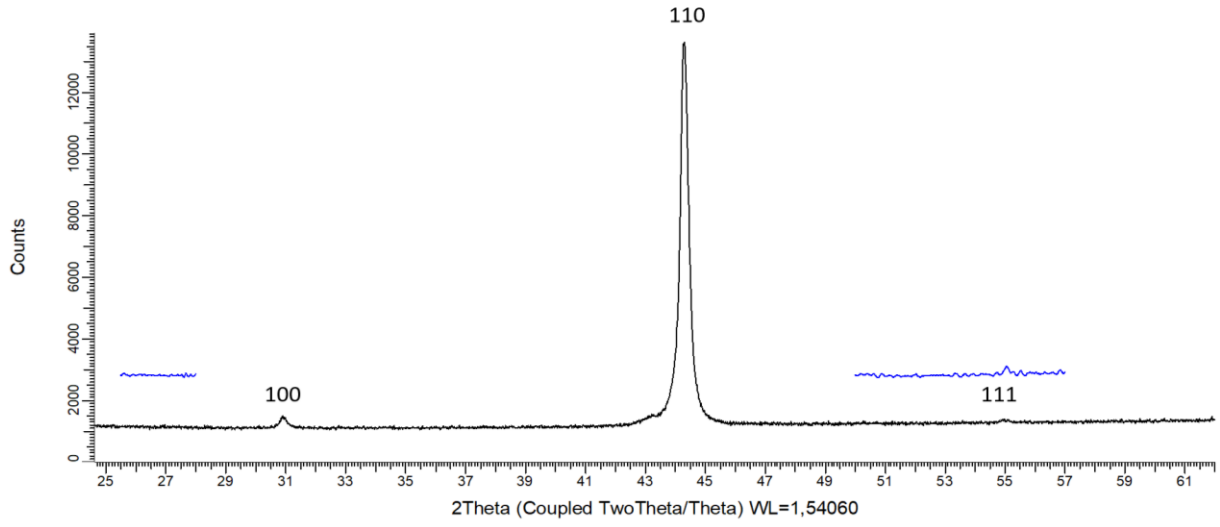

Fig. A.4: An experimental powder XRD result of Alloy B indexed for a B2 phase. The blue lines are measurements conducted with a small step size to reveal any low intensities of possible $L2_1$.

Appendix B

Structure factors for the B2 and $L2_1$ phases

The structure factor represents the amplitude and phase shift of a diffracted beam from a crystal and is a summation of all scattered wave contributions for the atoms in the unit cell. The observed intensity in a diffraction experiment is proportional to $|F_{hkl}|^2$.

$$F_{hkl} = \sum_{j=1}^{N} f_j \cdot e^{-2\pi i(hx_j + ky_j + lz_j)} \tag{B.1}$$

Here, x, y and z are the coordinates for the atom j. The *h*,*k*, and *l* are the Miller indices and f is the scattering factor for atom j. N is a positive integer, e is Euler's number, and i is the imaginary unit.

The scattering factor for atom j is indexed with the name of the Wyckoff position in the following "derivation". The reason of this indexing is that the five elements must share some atomic positions, in order to match the experimental EDS data, and the fact that there are more elements in the alloy than there are unique atomic positions in the unit cells of the presented structures. The atomic scattering factor is indexed with the Wyckoff site in order to represent all atoms associated with this position in the unit cell.

Some relations of Euler's equation that will be used:

$$e^{-\pi i(2n)} = 1 \tag{B.2}$$

$$e^{-\pi i(2n+1)} = -1 \tag{B.3}$$

$$e^{-\pi i\left(\frac{n}{2}\right)} = i \tag{B.4}$$

$$e^{-\pi i\left(\frac{3}{2}n\right)} = -i \tag{B.5}$$

n is an integer.

Structure factor derivation for L21

All atomic positions in a full Heusler ($L2_1$), space group no. 225, Fm-3m

Table B.1: Wycoff sites for the $L2_1$ structure

Atomic positions $L2_1$	Wycoff site
(0 0 0), (½ ½ 0), (½ 0 ½), (0 ½ ½)	4a
(0 0 ½), (½ 0 0), (0 ½ 0), (½ ½ ½)	4b
(¼ ¼ ¼), (¾ ¼ ¼), (¼ ¾ ¼), (¼ ¼ ¾), (¾ ¾ ¼), (¼ ¾ ¾), (¾ ¼ ¾), (¾ ¾ ¾)	8c

The structure factor with regards to Wycoff positions is

$$F_{hkl} = f_{4a} \cdot e^{-2\pi i(hx_{4a}+ky_{4a}+lz_{4a})} + f_{4b} \cdot e^{-2\pi i(hx_{4b}+ky_{4b}+lz_{4b})} + f_{8c} \cdot e^{-2\pi i(hx_{8c}+ky_{8c}+lz_{8c})} \quad \text{(B.6)}$$

Solve one term at a time in this equation

4a:

$$f_{4a} \cdot e^{-2\pi i(hx_{4a}+ky_{4a}+lz)} = f_{4a}\left(1 + e^{-\pi i(h+k)} + e^{-2\pi i(h+l)} + e^{-2\pi i(k+l)}\right) \quad \text{(B.7)}$$

When all *hkl* values are either even or odd, each term will be equal to one. For mixed values of *hkl*, with respect to parity, the sum will be zero. Thus

- *hkl* all even or all odd gives $4f_{4a}$
- mixed parity of *hkl* gives 0

4b:

$$f_{4b} \cdot e^{-2\pi i(hx_{4b}+ky_{4b}+lz_{4b})} = f_{4b}\left(e^{-\pi i(h)} + e^{-\pi i(k)}e^{-\pi i(l)}e^{-\pi i(h+k+l)}\right) \quad \text{(B.8)}$$

For the 4b positions it is clear that for all even values, each term will be equal to one, and for all odd values, each term will be negative one. For a mixed parity, the sum will be zero.

- *hkl* all even gives $4f_{4b}$
- *hkl* all odd gives $-4f_{4b}$
- mixed parity of *hkl* gives 0

8c:

$$f_{8c} \cdot e^{-2\pi i(hx_{8c}+ky_{8c}+lz_{8c})} \tag{B.9}$$

$$= f_{8c}\left(e^{-\pi i\frac{(h+k+l)}{2}} + e^{-\pi i\frac{(3h+k+l)}{2}} + e^{-\pi i\frac{(h+3k+l)}{2}}\right.$$

$$+ e^{-\pi i\frac{(h+k+3l)}{2}} + e^{-\pi i\frac{(3h+3k+l)}{2}} + e^{-\pi i\frac{(h+3k+3l)}{2}}$$

$$\left.+ e^{-\pi i\frac{(3h+k+3l)}{2}} + e^{-\pi i\frac{(3h+3k+3l)}{2}}\right)$$

Going forward, one divides into two types of even numbers. Even numbers that will turn odd when divided by 2, and even numbers that remains even when divided by 2. The first one will be $h+k+l = 4n + 2$ and the latter will be $h+k+l = 4n$.

One is also following same procedure for the odd numbers: Odd numbers divided by 2 will be either i, if $h+k+l = 4n + 3$, or $-i$, if $h+k+l = 4n + 1$.

This operation is done to account for the denominator in the exponential terms in Eq. B.9 above.

By plugging in values for *hkl*, one will find that for atoms located on the 8c positions, the *hkl* will be as follows:

- $h + k + l = 4n$ gives $8f_{8c}$
- $h + k + l = 4n + 2$ gives - $8f_{8c}$
- $h + k + l = 4n + 3$ gives 0
- $h + k + l = 4n + 1$ gives 0
- mixed parity of *hkl* gives 0

There is no difference between the two types of odd numbers, as both give zero. When considering the results for all Wycoff positions, there are in total three different categories for *hkl* that will contribute to intensity, and one that gives zero intensity. These are listed in table B.2 below.

Table B.2: Possible outcomes of $h + k + l$ for the $L2_1$ structure

$h + k + l$	4a	4b	8c
4n	$4f_{4a}$	$4f_{4b}$	$8f_{8c}$
4n + 2	$4f_{4a}$	$4f_{4b}$	$8f_{8c}$
Odd	$4f_{4a}$	$-4f_{4b}$	0
Mixed parity	0	0	0

Hence, the structure factor for $L2_1$ will be

$$F_{hkl} = \begin{cases} 4f_{4a} + 4f_{4b} + 8f_{8c} & \text{for } h + k + l = 4\text{n} \\ 4f_{4a} + 4f_{4b} - 8f_{8c} & \text{for } h + k + l = 4\text{n} + 2 \\ 4f_{4a} - 4f_{4b} & \text{for } h + k + l = \text{odd} \\ 0 & \text{for mixed parity of } hkl \end{cases} \quad \text{(B.10)}$$

This result is also used by P.J. Webster [52], but Webster does not show his procedure to arrive with this expression.

The structure factor for B2

Space group no. 221, Pm-3m, also known as the B2 structure.

This cubic structure has two different atomic positions, (0 0 0) and (½ ½ ½). If one considers the conventional unit cell, there is one atom position in the corner, and one in the body centre of the cube. This is the 1a and 1b Wycoff site, respectively. By using the same indexing for the scattering factor as for the Heusler, one gets

$$F_{hkl} = f_{1a} \cdot e^{-2\pi i(hx_{1a} + ky_{1a} + lz_{1a})} + f_{1b} \cdot e^{-2\pi i(hx_{1b} + ky_{1b} + lz_{1b})} \quad \text{(B.11)}$$

$$F_{hkl} = \begin{cases} f_{1a} + f_{1b} & \text{for } h + k + l = \text{even} \\ f_{1a} - f_{1b} & \text{for } h + k + l = \text{odd} \end{cases} \quad \text{(B.12)}$$

Appendix C

This Appendix contains an individual experiment carried out in the beginning of this study. The experiment was performed on a set of samples from the Magnificent project, that was not in possession of the author. The samples were from the $FeNiCoMn_xAl_x$ system, where $0.25 > x > 0.1$. The experiment was done in the early stages of this thesis, as an introduction to magnetic characterization and was guided by Pavlo Mikheenko.

The objective of the experiment was to get an overview of the magnetic structure for each sample, on millimetre to micrometre scale, and to convert the observed light intensity from the magneto-optical (MO) indicator films to magnetic field strength. A comparison of the magnetic strength for samples 9 to 14 was done by plotting the MOI intensity of each sample, and a similar MFM experiment tested the validity of these results.

Preparation

Cylindrical, polished samples were prepared by the Magnificent project.

Experimental

A magnetic field was applied by current flowing through a coil. The current, and consequently magnetic field was measured directly by the Power Supply unit. A sample was placed above, but close to the coil, and the MO film was placed on top of it. A polarized light microscope observed the surface of the film, and the images were captured with a mounted camera.

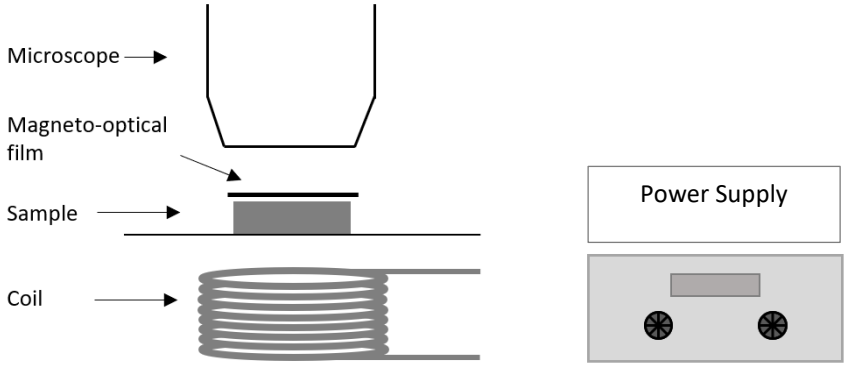

Fig. C.1: shows the experimental setup for the MOI measurements.

The local light intensity in the images was converted into magnetic field strength. For the calibration of the field, the MO film was measured in the absence of the sample. A current through the coil was increased from 0 to 5.0 A and decreased back to zero, with a step of 0.5 A. For each step, an image was captured, and both voltage and current through the coil were recorded. The exposure time for each recording was kept constant at 1.8 milliseconds. The same sequence of increasing and decreasing current was repeated without the MO film present, and a Gaussmeter was used to measure the magnetic field in the position of the film, as a function of voltage, displayed on Power Supply.

Data analysis

The intensity in black-and-white images was measured by creating a histogram in the ImagePro 8 software. A histogram was created for each sample, with the number of pixels plotted versus the intensity in the image. The data were transferred to the Origin software, fitted with gaussian curves, and the maxima of each peak were extracted. These intensity maxima were plotted as a function of voltage. The magnetic field data acquired from the Gaussmeter were also plotted as a function of voltage and the linear regression was applied to get a function for this relationship, as this was expected from theory (Faraday's law). From these two relationships, the magnetic field was plotted as a function of light intensity. A polynomial curve fit was created, and the obtained formula could be applied to convert light intensity in magneto-optical images to the magnetic field strength.

Validation of the experiment

The experimental results from MOI were ultimately cross-checked with MFM. Each sample was measured under the same conditions applying magnetic field of 580 mT, for 5 random positions on the sample. The average magnetic field above the sample was calculated measuring phase shift of the probe oscillations and normalizing it on the mass of the sample in order to compare it with the MOI results.

Results and discussion

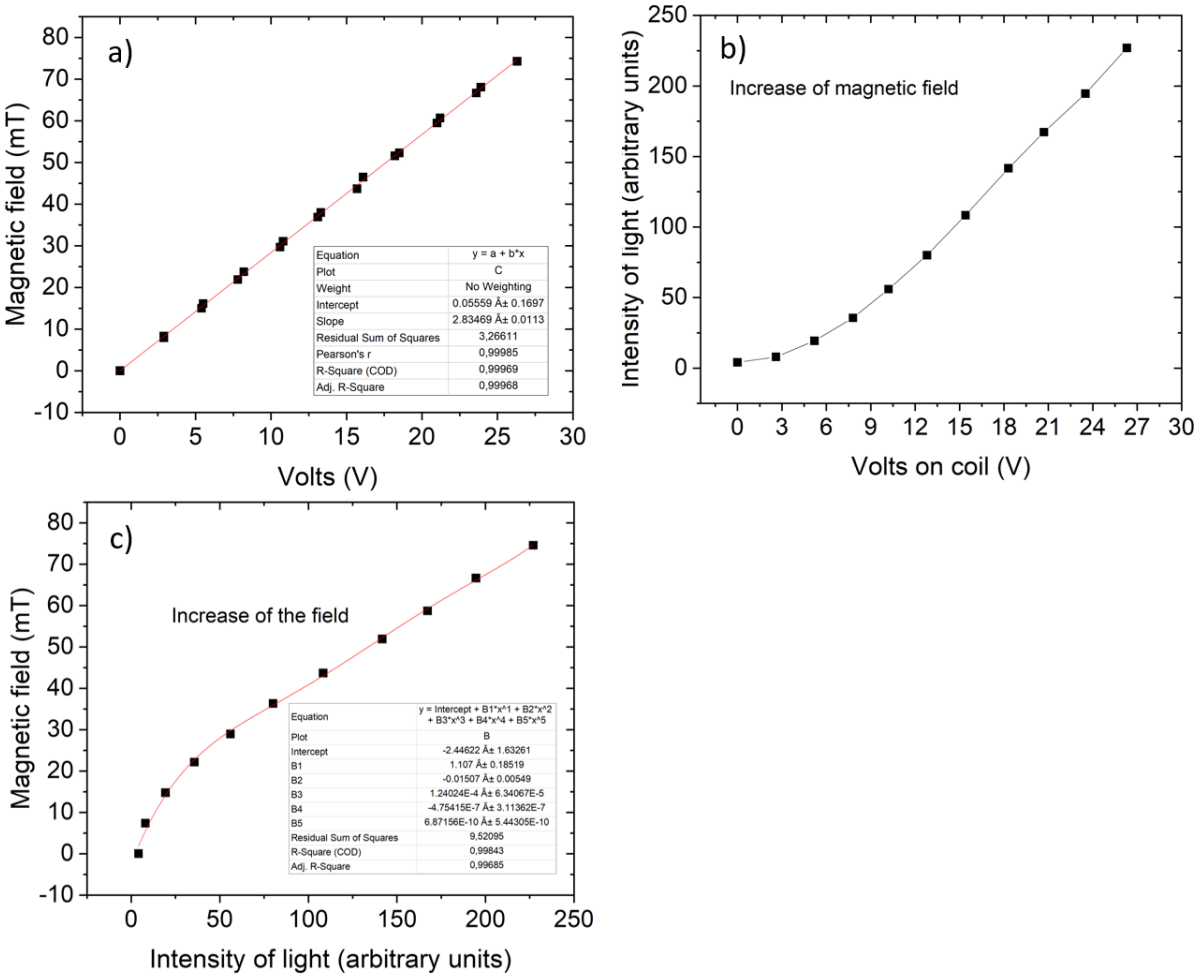

Fig. C.2: **a)** Linear regression for the magnetic field as a function of the voltage on the coil, **b)** Light intensity on the MOI film plotted as a function of the voltage. **c)** Relationship between the magnetic field and the intensity of the light with the polynomial curve fit.

The linear regression in a) fitted very well to the data points, as expected from the theory, which confirms that the instruments are operating correctly. The formula from the polynomial fit makes it easy to convert image intensity into the magnetic field strength for future testing, considering an identical setup and using the same MOI film and camera exposure time. A limitation for the resolution is the wavelength of light and the magnetic domain size in the MOI film. It is not possible to observe differences in the magnetic field at distances smaller than these.

MOI and MFM results compared

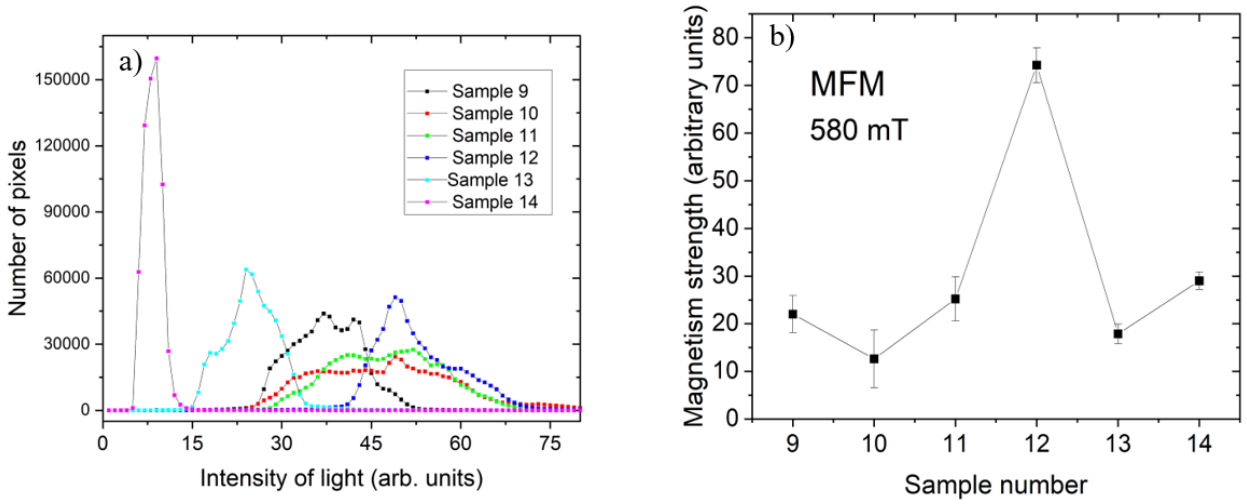

Fig. C.3: a) Light intensities from the MOI experiment for samples 9 to 14 at a current of 1.0 A through the coil. **b)** Relative MFM magnetic field strength plotted for samples 9 to 14, with the respective error bar.

Both the MOI and MFM evaluate the relative magnetic strength between the samples. Although sample 12 seems to be the best according to both MOI and MFM measurements, the results are inconsistent, suggesting an experimental failure, which may have occurred due to large sensitivity of MOI experiment to the angle of light incidence. For example, in contrast to MFM, MOI shows that sample 14 has the lowest average intensity, hence the weakest average magnetic field. For the rest of the samples, the intensity peaks are broad, arising from an uneven intensity distribution in the respective images. The angle of the incidence depends on the tilt of MO film, which when optimized should be parallel to the objective lens of the microscope. The broad intensity of peaks could be a result of domain structure in the sample and MOI film, as well as roughness of the surface. The broad peaks make it difficult to determine the mean intensity. Further MOI experiments must be carried out to find origin of possible systematic errors.

Despite some drawbacks, MOI images are easy to interpret, and the technique allows observing large areas and comparing different samples in the millimetre to micrometre scale.

Appendix D

The following paper was applied to the 2021 IEEE 11th International Conference on "Nanomaterials: Applications & Properties" and approved. The article presents the correlating SEM and MFM results of Alloy A and is attached for the interested reader.

10th International Conference on
"Nanomaterials: Applications & Properties" (NAP-2021)
Odesa, Ukraine, 5-11 Sept. 2021

Identifying Magnetic Phases in Additively Manufactured High-Entropy Alloy $FeCoNiAl_xMn_x$

Aleksander Amble Larsen
Department of Physics
University of Oslo
Oslo, Norway
a.a.larsen@kjemi.uio.no

Calliope Bazioti
Department of Physics
University of Oslo
Oslo, Norway
kalliopi.bazioti@smn.uio.no

Branson Belle
SINTEF Industry
Oslo, Norway
Branson.Belle@sintef.no

Anthoula Poulia
Department of Physics
University of Oslo
Oslo, Norway
anthoula.poulia@smn.uio.no

Patricia Carvalho
SINTEF Industry
Oslo, Norway
patricia.carvalho@sintef.no

Spyros Diplas
SINTEF Industry
Oslo, Norway
Spyros.Diplas@sintef.no

Amin Azar
SINTEF Industry
Oslo, Norway
amin.azar@sintef.no

Anette Eleonora Gunnæs
Department of Physics
University of Oslo
Oslo, Norway
a.e.gunnas@fys.uio.no

Pavlo Mikheenko
Department of Physics
University of Oslo
Oslo, Norway
pavlo.mikheenko@fys.uio.no

***Abstract*—High-Entropy Alloys are advanced technological materials composed of several (typically five) elements in nearly equal atomic concentration. By forming these alloys, previously unknown phase fields of multidimensional phase diagrams are explored. The large number of possible substitutions of constituent elements on crystal lattice sites justifies the dominant contribution of mixing entropy over enthalpy to the free energy reduction. This leads to the formation of phases, which otherwise could not be formed in alloys with fewer main alloying elements. Here we explore magnetic and compositional properties of a High-Entropy Alloy, namely $FeCoNiAl_xMn_x$ ($0.05 \leq x \leq 3.08$), composed of magnetic (Fe, Co, Ni) and non-magnetic elements (Al, Mn). By magnetic force microscopy of a selected area, it is observed that for intermediate to low Al and Mn contents, the alloy splits in two major crystallographic phases with different magnetic properties. Elemental maps of the same area were recorded with energy dispersive spectroscopy and scanning electron microscopy. Counterintuitively, it was found that the phase rich in non-magnetic Al has stronger magnetism than the phase rich in Fe. This work showcases possible applications of the here presented HEAs as soft magnetic materials in functional magnetic elements.**

***Keywords— High-entropy alloys, magnetic properties, magnetic force microscopy, nano-structure*.**

I. Introduction

The recently emerged new class of materials, High Entropy Alloys (HEAs), is attracting considerable attention due to the formation of unexplored phases stabilized by the high mixing entropy [1]. Some of these phases have -among others- unique mechanical [2-4] or interesting magnetic [5-7] properties. The magnetically strong and relatively inexpensive materials, Fe, Co and Ni were chosen to coexist with Al and Mn. The choice of Al and Mn is not accidental, as it is known that, although they are non-magnetic as individual elements, in combination with each other they form strong ferromagnetic compounds [8]. The parametric modelling presented in [5] shows that in a certain range of Al and Mn content, $FeCoNiAl_xMn_x$ exhibits a tendency to form two separate phases. At high concentration of Mn and Al, a body-centered cubic ordered alloy is expected, whereas at low Al and Mn contents, a face-centered cubic phase is mainly predicted. At intermediate Al and Mn contents, a mixture of these phases is more likely to be stable. Similar phase transitions regarding the same system were also postulated by other works [9]. The study in [5], also on the $FeCoNiAl_xMn_x$ system, was mainly focused on intermediate and low concentrations of Al and Mn. Extending this range, three samples of different concentrations, high, low and intermediate have been investigated by magnetic force microscopy (MFM) and energy dispersive x-ray analysis (EDX) on a scanning electron microscope (SEM). The main purpose of the study was to identify different magnetic phases and associate them with alloy composition, by imaging the same region in the material. The present study further aims to clarify how the nanostructure of the samples influences their magnetic properties.

II. Experimental Procedure

$FeCoNiAl_xMn_x$ ($0.05 \leq x \leq 3.08$) alloys were prepared using Laser Metal Deposition [5]. The desired element composition was achieved by controlling the weight of the elemental powders. The elemental composition in the samples was mapped using a TM3000 TableTop SEM. MFM was performed on a JPK NanoWizard 4.0 scanning probe microscope in AC mode at resonance frequency of 74 KHz using magnetic probes PPP-MFMR-10 (Nanosensors, Switzerland). An external magnetic field of 0.58 T was applied during the study. To distinguish between van der Waals and magnetic forces in MFM, a two-pass technique [10-12] was utilized. In the first pass, the topography close to the sample was measured. In the second scan, the topography measurement was repeated with the tip at a bigger height. At heights above 20 nm, van der Waals forces are weak, and the dominant magnetic response could be measured. This response is represented by the shift in the phase of probe oscillations, which is proportional to the gradient of the force acting to the tip [10,13,14].

III. Results and Discussion

The samples investigated in this study have the following nominal compositions: S1 - $FeNiCoAl_{0.9}Mn_{0.9}$, S2 - $FeNiCoAl_{0.29}Mn_{0.29}$ and S3 - $FeNiCoAl_{0.08}Mn_{0.08}$. The sample S1 is nominally the closest to a HEA with nearly equiatomic percentage of the constituent elements. By MFM, it was found that samples S1 and S3 behave like single-phase magnetic compounds. Results for S3 presented in this work, are also representative for S1. On the contrary, S2 revealed the coexistence of two different magnetic phases.

In Fig. 1, the emergence of magnetic structure with the height of the record is illustrated in the phase shift maps of sample S1. It is a pseudo-3D presentation composed of individual planar images of a 30×30 μm^2 surface recorded at the various heights shown in the plot. At zero height, only topography features are seen (lowest image). With increasing height, van der Waals interaction becomes weak, and the magnetic interaction becomes dominant, thus revealing features of magnetism in the sample [12]. Four magnetic grains are clearly seen at heights between 50 and 300 nm.

The grains in sample S1 are large (around 30-100 μm) and smaller sub-grains of the order of ~ 2 μm are also presented. Similar grain sizes (30-100 μm) with little variation in magnetic properties were also found in sample S3. However, sample S2 exhibited a different morphology. Fig. 2a shows a typical phase shift map for sample S2 recorded at the height of 200 nm. The magnetic grains in this sample are smaller than in S1 and S3, they are of irregular shape and there is a large difference in magnetic contrast between two types of observed grains. The grains of one type look darker than the other ones, and frequently they consist of stripy magnetic domains. The magnified magnetic domain structure of a selected grain is depicted in Fig. 2b. Fig. 2c shows the topography of the area corresponding to Fig. 2b. In Fig. 2c, the dark grains shown in Fig. 2b seem to stand out and be flat after the polishing, which indicates that they are harder than the grains of the bright phase.

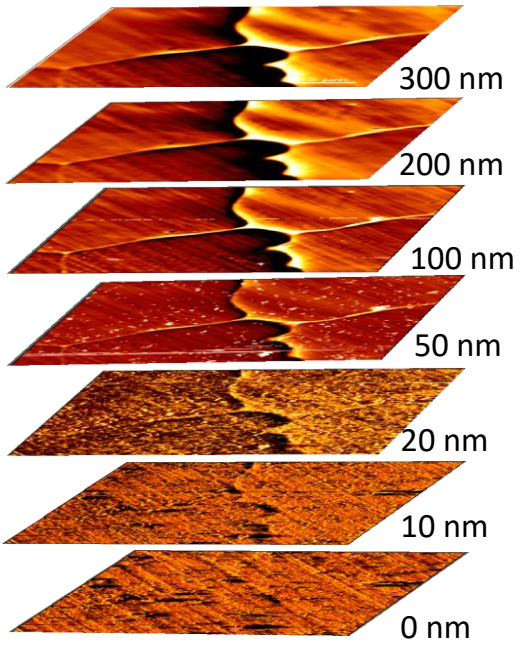

Fig. 1. Phase shift maps of sample S1 illustrating the emergence of the magnetic structure with the increase of the height above the sample. The height for each image is shown by the number close to it in the plot.

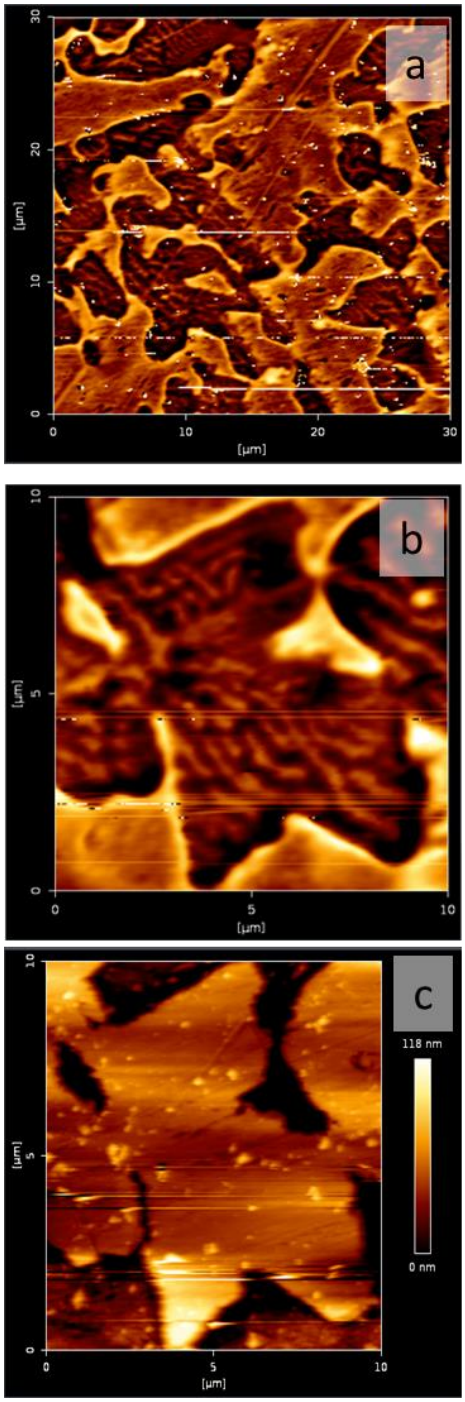

Fig. 2. Large- (a) and small-scale (b) phase shift maps for sample S2. Image c) shows the topography of the area corresponding to image b).

In Fig 2c, one can also see a large number of nano-inclusions. According to the element analysis, most of them are Al oxide particles. These nano-inclusions have a strong influence on the magnetic structure inside the grains of the dark phase, since they pin domain walls. This typically reduces magnetic softness of the material and increases the coercivity of the hysteresis loops.

To find out the composition of the dark and bright phases in S2, EDX analysis was performed on a large area that was previously scanned in MFM. Fig. 3a shows the SEM image and the outlined area chosen for EDX mapping. The grain boundaries are clearly seen in the image helping in the selection of the right spot for the comparison with the corresponding magnetic maps.

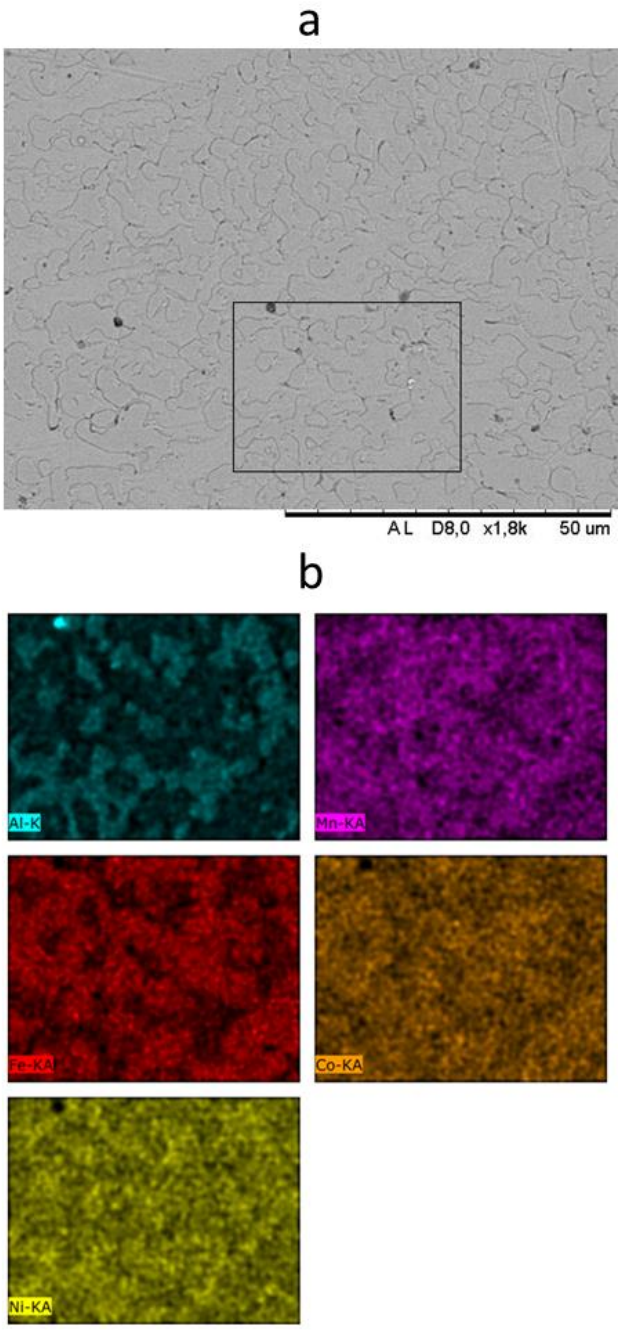

Fig. 3. a) SEM image of the surface of sample S2 with outlined area chosen for EDX quantification mapping. b) EDX maps of different elements corresponding to the black scanned rectangle in a). The biggest difference between the grains is in content of Al and Fe.

In Fig. 3b, the EDX maps of the constituent elements are shown for the outlined by black line scanned rectangle of Fig. 3a. The biggest difference between the grains is in the content of Al and Fe, which are in anti-correlation with each other. The intensity of Mn signal seems to be following that of Al in the maps, although the distribution of Mn is more diffused than that of Al and Fe. Co and Ni are distributed more evenly than the other elements.

In Figs. 4a and b, the comparison between MFM magnetic map and elemental map of Al in the same region is shown. The Al map is slightly rotated to perfectly match the scanning direction in MFM and has an image transparency of 30%.

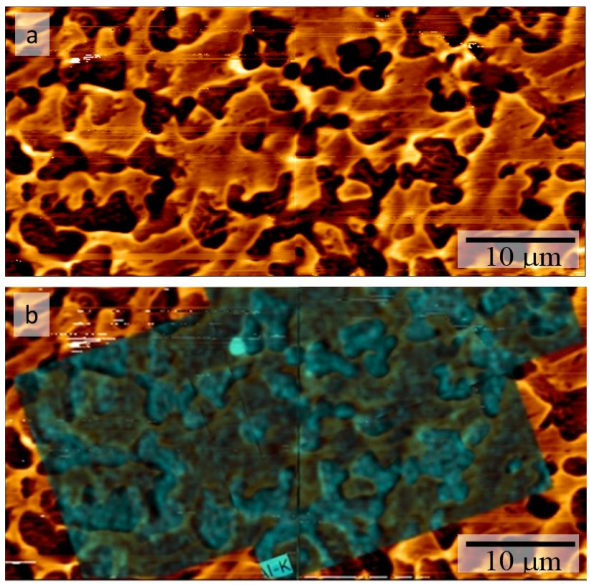

Fig. 4 a) MFM magnetic map and b) the same MFM magnetic map overlaid with EDX elemental map of Al. The dark areas in the MFM map correspond to grains with enhanced amount of Al.

In Fig. 4b, the brighter blue color corresponds to a higher Al concentration and matches identically with the dark domain areas in Fig. 4a. The elemental content of the phases with high and low concentration in Al was clarified by analyzing the EDX maps shown in Figs. 3 and 4. The Al-rich phase constitutes of the following percentage of elements: Fe - 22.2±1.4%, Ni - 24.4 ±1.0 %, Co - 23.1±0.7 %, Mn - 12.0±0.6 % and Al - 18.4 ±0.9 %. The elemental content in the Fe-rich phase was found to be the following: Fe - 28.5±1.0%, Ni - 22.7 ±0.5 %, Co - 26.2±1.0 %, Mn - 12.1±0.9 % and Al - 10.5 ±1.0 %. It is interesting that the concentration of Mn is the same in both phases, and the amount of Ni and Co differs only by 1.7 and 3.1 %, respectively. In contrast, in the dark Al-rich phase, the concentration of Fe is 6.3 % lower, and the concentration of Al is 7.9 % higher than in the Fe-rich phase that looks brighter in the MFM images.

Finally, to quantitatively analyze the MFM measurements, the maximum value of the MFM phase shift was evaluated in the alloy. The MFM phase shift is the gradient of the magnetic interaction force between two magnetic dipoles, the moments of which are aligned along the same z axis. In Fig. 5, we determine the mean value of the MFM phase shift from the Gaussian fit of the obtained histogram. The detailed fitting parameters are tabulated below the histogram plot. As observed, there is a peak splitting of the histogram intensity. This means that the grains with the higher Al content that match well with the dark grains in the MFM image, present a more negative phase shift (calculated as -96.5 degrees utilizing the Gaussian fitting process), thus attracting stronger the MFM probe [12]. On the contrary, the Fe-rich area (bright area in the MFM phase shift) still possesses a negative phase shift value (-90.5 degrees), but this peak is slightly shifted to the right of the previously mentioned histogram peak, implying a less magnetic area. In general, due to the high concentration of the magnetic energy, the dark grains rich in Al have stronger tendency to split into magnetic domains demonstrating well-expressed stripy structure (see Figs. 2a,b and Fig. 4a).

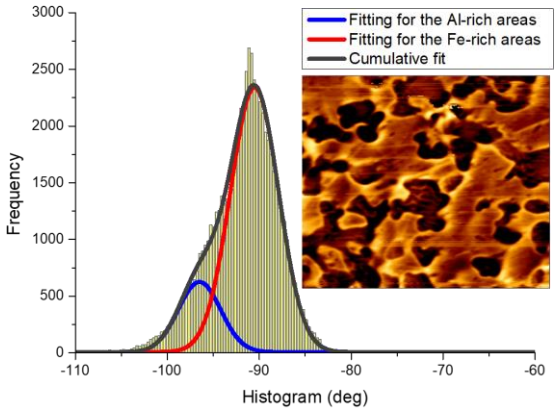

Model	Gaussian		
Equation	y=y0+A/(w*sqrt(PI/4*ln(2)))*exp(-4*ln(2)*(x-xc)^2/w^2)		
R-Square	0.99122		
		Value	Standard Error
Peak 1	y0	6.92784	3.89628
Peak 1	xc	**-96.50985**	0.24224
Peak 1	A	3570.96079	390.20616
Peak 1	w	5.41967	0.38942
Peak 2	y0	6.92784	3.89628
Peak 2	xc	**-90.51408**	0.07324
Peak 2	A	15358.45327	397.69642
Peak 2	w	6.18085	0.12548

Fig. 5 MFM phase shift histogram corresponding to the Al-rich and the Fe-rich magnetic domains of the embedded area. The Al-rich phase is more magnetic since it possesses a histogram shifted to more negative values as calculated according to the Gaussian fitting model.

IV. Conclusions

Two distinct magnetic phases were observed by magnetic force microscopy (MFM) in the $FeCoNiAl_xMn_x$ high-entropy alloy with nominal value of x of about 0.3. The combination of this technique with energy-dispersive x-ray analysis in scanning electron microscopy, being applied to the same area of the sample, allowed to identify the elemental content of both phases. One of them, possessing high concentration of Al and low concentration of Fe, was proven to exhibit strongest magnetic response as verified by calculating the MFM phase shift histograms. The recorded magnetic maps display high concentration of magnetic energy and stripy domain structure in the stronger magnetic phase with higher concentration of Al. The domain structure also seems to be influenced by the presence of nano-inclusions and deformations produced during polishing of the samples. The samples with x of 0.9 and 0.08 look magnetically homogeneous with the observed differences caused possibly by the different crystallographic orientation of the grains. The study shades light on the magnetic behavior of the $FeCoNiAl_xMn_x$ alloys and could help in developing strategies for producing high-entropy alloys with targeted magnetic properties, suitable for large-scale industrial applications.

Acknowledgment

This work is part of the Project “MAGNIFICENT - Additively manufactured magnetic high entropy alloys for renewable electricity”, funded by the Research Council of Norway (pr. nr 287979) within the Nano2021 Program.

References

[1] E. P. George, D. Raabe, and R. O. Ritchie, “High- entropy alloys,” Nature Reviews Materials, vol. 4, pp. 515-534, August 2019.

[2] M. H. Tsai, and J. W.Yeh, “High-entropy alloys: a critical review,” Materials Research Letters, vol. 2, pp. 107-123, April 2014.

[3] L. Huang, Y. Sun, A. Amar, C. Wu, X. Liu, G. Le, X. Wang, J. Wu, K. Li, C. Jiang, and J. Li “Microstructure evolution and mechanical properties of $Al_xCoCrFeNi$ high-entropy alloys by laser melting deposition,” Vacuum, vol. 183, 109875, January 2021.

[4] J. Zhang, H. Qiu, H. Zhu, and Z. Xie, “Effect of Al additions on the microstructures and tensile properties of $Al_xCoCr_3Fe_5Ni$ high entropy alloys,” Materials Characterization, vol. 175, 111091, May 2021.

[5] A. Poulia, A. Azar, P. Svec, C. Bazioti, B. Belle, A. E. Gunnæs, S. Diplas, and P. Mikheenko, "Nanoscale Magnetic Properties of Additively Manufactured $FeCoNiAl_xMn_x$ High-Entropy Alloys," 2020 IEEE 10th International Conference Nanomaterials: Applications & Properties (NAP), Sumy, Ukraine, pp. 01NMM02-1-01NMM02-5, January 2021.

[6] R. K. Mishra, and R. Shahi, “A systematic approach for enhancing magnetic properties of CoCrFeNiTi-based high entropy alloys via stoichiometric variation and annealing,” Journal of Alloys and Compounds, vol. 821, 153534, April 2020.

[7] C. L. P. Pavithra, R. K. S. .K. Janardhana, K. M. Reddy, C. Murapaka, J. Joardar, B. V. Sarada, R. R. Tamboli, Y. Hu, Y. Zhang, X. Wang, and S. R. Dey “An advancement in the synthesis of unique soft magnetic CoCuFeNiZn high entropy alloy thin films,” Scientific Reports, vol. 11, 8836, April 2021.

[8] J.H. Park, Y.K. Hong, S. Bae, J.J. Lee, J. Jalli, G.S. Abo, N. Neveu, S.G. Kim, C.J. Choi, and J.G. Lee, "Saturation magnetization and crystalline anisotropy calculations for MnAl permanent magnet," Journal of Applied Physics, vol. 107, pp. 1-3, April 2010.

[9] Z. Li, G. Bai, X. Liu, S. Bandaru, Z. Wu, X. Zhang, M. Yan, and H. Xu “Tuning phase constitution and magnetic properties by composition in FeCoNiAlMn high-entropy alloys,” Journal of Alloys and Compounds, vol. 845, 156204, December 2020.

[10] D. Passeri, C. Dong, M. Reggente, L. Angeloni, M. Barteri, F.A. Scaramuzzo, F. De Angelis, F. Marinelli, F. Antonelli, F. Rinaldi, C. Marianecci, M. Carafa, A. Sorbo, D. Sordi, I. WCE Arends, and M. Rossi, “Magnetic force microscopy. Quantitative issues in biomaterials,” Biomatterials, vol. 4, e29507, July 2014.

[11] G. Cordova, B.Y. Lee, and Z. Leonenko, “Magnetic Force Microscopy for Nanoparticle Characterization,” NanoWorld Journal, vol 2, pp. 10-14, April 2016.

[12] A. L. Campaña, N. Joudeh, H. Høyer, A. Røyne, D. Linke, and P. Mikheenko, "Probing Van Der Waals and Magnetic Forces in Bacteria with Magnetic Nanoparticles," 2020 IEEE 10th International Conference Nanomaterials: Applications & Properties (NAP), Sumy, Ukraine, 2020, pp. 01NSSA03-1-01NSSA03-5

[13] B. Torre, G. Bertoni, D. Fragouli, A. Falqui, M. Salerno, A. Diaspro, R. Cingolani, and A. Athanassiou, “Magnetic, force microscopy and energy loss imaging of superparamagnetic iron oxide nanoparticles,” Scientific Reports, vol.1, 202, December 2011.

[14] Sarid D, Scanning Force Microscopy. New York, USA: Oxford University Press, 1994.